

Quantitative Analysis of Kilohertz-Frequency Neurostimulation

by

Leonel E. Medina Daza

Department of Biomedical Engineering  
Duke University

Date: \_\_\_\_\_

Approved:

\_\_\_\_\_  
Warren M. Grill, Supervisor

\_\_\_\_\_  
Craig S. Henriquez

\_\_\_\_\_  
Marc A. Sommer

\_\_\_\_\_  
Patrick D. Wolf

\_\_\_\_\_  
Shivanand (Nandan) Lad

Dissertation submitted in partial fulfillment of  
the requirements for the degree of Doctor  
of Philosophy in the Department of  
Biomedical Engineering in the Graduate School  
of Duke University

2016

ABSTRACT

Quantitative Analysis of Kilohertz-Frequency Neurostimulation

by

Leonel E. Medina Daza

Department of Biomedical Engineering  
Duke University

Date: \_\_\_\_\_  
Approved:

\_\_\_\_\_  
Warren M. Grill, Supervisor

\_\_\_\_\_  
Craig S. Henriquez

\_\_\_\_\_  
Marc A. Sommer

\_\_\_\_\_  
Patrick D. Wolf

\_\_\_\_\_  
Shivanand (Nandan) Lad

An abstract of a dissertation submitted in partial  
fulfillment of the requirements for the degree  
of Doctor of Philosophy in the Department of  
Biomedical Engineering in the Graduate School of  
Duke University

2016

Copyright by  
Leonel E. Medina Daza  
2016

## Abstract

Mainstream electrical stimulation therapies, *e.g.*, spinal cord stimulation (SCS) and deep brain stimulation, use pulse trains that are delivered at rates no higher than 200 Hz. In recent years, stimulation of nerve fibers using kilohertz-frequency (KHF) signals has received increased attention due to the potential to penetrate deeper in the tissue and to the ability to block conduction of action potentials. As well, there are a growing number of clinical applications that use KHF waveforms, including transcutaneous electrical stimulation (TES) for overactive bladder and SCS for chronic pain. However, there is a lack of fundamental understanding of the mechanisms of action of KHF stimulation. The goal of this research was to analyze quantitatively KHF neurostimulation.

We implemented a multilayer volume conductor model of TES including dispersion and capacitive effects, and we validated the model with *in vitro* measurements in a phantom constructed from dispersive materials. We quantified the effects of frequency on the distribution of potentials and fiber excitation. We also quantified the effects of a novel transdermal amplitude modulated signal (TAMS) consisting of a non-zero offset sinusoidal carrier modulated by a square-pulse train. The model revealed that high-frequency signals generated larger potentials at depth than did low frequencies, but this did not translate into lower stimulation thresholds. Both TAMS and conventional rectangular pulses activated more superficial fibers in addition to the deeper, target fibers, and at no frequency did we observe an inversion of the strength-distance relationship. In addition, we performed *in vivo* experiments and applied direct stimulation to the sciatic nerve of cats and rats. We measured electromyogram and compound action potential activity evoked by pulses, TAMS and modified versions of TAMS in which we varied the

amplitude of the carrier. Nerve fiber activation using TAMS showed no difference with respect to activation with conventional pulse for carrier frequencies of 20 kHz and higher, regardless the size of the carrier. Therefore, TAMS with carrier frequencies  $>20$  kHz does not offer any advantage over conventional pulses, even with larger amplitudes of the carrier, and this has implications for design of waveforms for efficient and effective TES.

We developed a double cable model of a dorsal column (DC) fiber to quantify the responses of DC fibers to a novel KHF-SCS signal. We validated the model using *in vivo* recordings of the strength-duration relationship and the recovery cycle of single DC fibers. We coupled the fiber model to a model of SCS in human and applied the KHF-SCS signal to quantify thresholds for activation and conduction block for different fiber diameters at different locations in the DCs. Activation and block thresholds increased sharply as the fibers were placed deeper in the DCs, and decreased for larger diameter fibers. Activation thresholds were  $> 5$  mA in all cases and up to five times higher than for conventional ( $\sim 50$  Hz) SCS. For fibers exhibiting persistent activation, the degree of synchronization of the firing activity to the KHF-SCS signal, as quantified using the vector strength, was low for a broad amplitude range, and the dissimilarity between the activities in pairs of fibers, as quantified using the spike time distance, was high and decreased for more closely positioned fibers. Conduction block thresholds were higher than 30 mA for all fiber diameters at any depth and well above the amplitudes used clinically (0.5 – 5 mA). KHF-SCS appears to activate few, large, superficial fibers, and the activated fibers fire asynchronously to the stimulation signal and to other activated fibers.

The outcomes of this work contribute to the understanding of KHF neurostimulation by establishing the importance of the tissue filtering properties on the distribution of potentials, assessing quantitatively the impact of KHF stimulation on nerve fiber excitation, and developing

and validating a detailed model of a DC fiber to characterize the effects of KHF stimulation on DC axons. The results have implications for design of waveforms for efficient and effective nerve fiber stimulation in the peripheral and central nervous system.

## **Dedication**

To my beloved wife, Marce, and daughter, Sofi.

# Contents

Abstract .....	iv
List of Tables .....	xiv
List of Figures .....	xv
Acknowledgements.....	xvii
Chapter 1: Introduction and Overview .....	20
1.1 Introduction .....	20
1.2 Clinical applications of kilohertz-frequency stimulation .....	21
1.2.1 Spinal cord stimulation for chronic pain relief.....	21
1.2.2 Transcutaneous electrical stimulation for physical therapy .....	24
1.2.3 Other clinical applications of transcutaneous electrical stimulation .....	27
1.2.4 Peripheral nerve stimulation for phantom limb pain relief .....	29
1.2.5 Vagus nerve stimulation for the treatment of obesity .....	30
1.2.6 Transcranial alternating current stimulation for the treatment of brain cancer .....	30
1.2.7 Deep brain stimulation for the treatment of Parkinson’s disease.....	31
1.3 Neural responses to kilohertz-frequency stimulation .....	32
1.3.1 Firing rate differs from stimulation frequency .....	33
1.3.2 Activation varies non-monotonically with stimulus amplitude .....	35
1.3.3 Responses to kilohertz-frequency signals exhibit adaptation.....	37
1.3.4 Kilohertz-frequency signals can block the conduction of action potentials.....	38
1.4 Effects of tissue electrical properties on potentials and implications for kilohertz-frequency stimulation .....	41
1.4.1 Tissue conductivity and permittivity exhibit dispersion .....	42

1.4.2	Models using kilohertz-frequency stimulation may need to incorporate capacitive effects or dispersion .....	44
1.4.3	The impedance of the electrode-tissue interface decays with increasing frequency	45
1.4.4	Adding dispersion to physical models to quantify potentials.....	46
1.5	Some technical considerations.....	46
1.6	Introduction to dissertation and outline of chapters .....	48
Chapter 2:	Volume Conductor Model of Transcutaneous Electrical Stimulation with Kilohertz Signals	51
2.1	Introduction .....	51
2.2	Methods .....	52
2.2.1	Volume conductor model.....	52
2.2.2	Frequency-dependent dielectric properties .....	56
2.2.3	Cable model of a myelinated nerve fiber .....	57
2.2.4	Stimulation waveforms .....	58
2.2.5	Model validation .....	58
2.3	Results .....	59
2.3.1	Distribution of potentials and penetration distance .....	59
2.3.2	Fiber excitation with TAMS and conventional pulses .....	61
2.3.3	Filtering properties of the axonal membrane .....	63
2.3.4	Prediction of experimentally measured thresholds .....	65
2.4	Discussion.....	67
2.4.1	Filtering properties of biological tissue.....	67
2.4.2	Influence of the electrode-skin interface (ESI) .....	68
2.4.3	The transdermal amplitude modulated signal (TAMS).....	69
2.4.4	Voltage versus current stimulation.....	69

2.4.5	Conduction block .....	70
2.4.6	Model limitations .....	71
2.5	Conclusion.....	72
Chapter 3:	Phantom Model of Transcutaneous Electrical Stimulation.....	73
3.1	Introduction .....	73
3.2	Methods .....	74
3.2.1	Phantom Overview .....	74
3.2.2	Agar-based Gel: Mixing Protocol .....	75
3.2.3	Biological and Synthetic Materials .....	75
3.2.4	Dielectric Properties of Materials .....	76
3.2.5	TES Phantom .....	77
3.2.6	Mathematical Model .....	78
3.3	Results .....	78
3.4	Discussion.....	81
Chapter 4:	Nerve Excitation Using an Amplitude-Modulated Signal with Kilohertz-Frequency Carrier and Non-Zero Offset.....	83
4.1	Introduction .....	83
4.2	Methods .....	85
4.2.1	Stimulation waveforms .....	85
4.2.2	Computational model.....	86
4.2.3	In vivo experiments.....	87
4.2.4	Statistical analysis .....	89
4.3	Results .....	90
4.3.1	Simulations in a computational model of peripheral nerve fiber stimulation .....	90

4.3.2	In vivo measurements .....	92
4.4	Discussion.....	95
4.4.1	Mechanisms of nerve fiber activation using TAMS .....	95
4.4.2	Implications for transcutaneous electrical stimulation .....	98
4.4.3	Limitations .....	99
4.5	Conclusion.....	100
<b>Chapter 5: Computational Model of a Dorsal Column Fiber and Application to Spinal Cord Stimulation 101</b>		
5.1	Introduction .....	101
5.2	The dorsal columns.....	102
5.2.1	Overview .....	102
5.2.2	Fiber morphology.....	102
5.2.3	Ion channels .....	103
5.3	Methods.....	105
5.3.1	Model development.....	105
5.3.1.1	Morphology .....	105
5.3.1.2	Ion channels.....	106
5.3.1.3	Frequency-dependent membrane capacitance .....	106
5.3.1.4	Dynamics of extracellular potassium concentration.....	107
5.3.2	Model validation .....	110
5.3.3	Patient-specific model of spinal cord stimulation .....	113
5.3.4	Metrics to quantify activation patterns.....	114
5.3.5	Experimental measurements .....	116
5.3.5.1	Animal preparation.....	116

5.3.5.2	Strength-duration relationship .....	118
5.3.5.3	Recovery cycle .....	118
5.4	Results .....	118
5.4.1	Model validation .....	118
5.4.1.1	Action potential shape and conduction velocity.....	118
5.4.1.2	Current-distance relationship.....	119
5.4.1.3	Strength-duration relationship .....	120
5.4.1.4	Recovery cycle .....	121
5.4.2	Dynamic effects of extracellular potassium concentration .....	122
5.4.3	Thresholds calculated in a patient-specific model of spinal cord stimulation.....	124
5.5	Discussion.....	129
5.5.1	The strength-duration relationship .....	129
5.5.2	The recovery cycle .....	130
5.5.3	Effects of extracellular potassium concentration .....	132
5.5.4	Implications for spinal cord stimulation.....	133
5.6	Conclusion.....	135
Chapter 6:	Conclusions and Future Directions .....	136
6.1	Conclusions .....	136
6.2	Future directions.....	137
6.2.1	Kilohertz-frequency transcutaneous electrical stimulation .....	137
6.2.2	Kilohertz-frequency spinal cord stimulation.....	138
6.2.3	Neural responses to kilohertz-frequency signals.....	139
Appendix A:	Volume Conductor Model of Transcutaneous Electrical Stimulation – Coefficients of Fourier Method .....	141

Appendix B: Model of Dorsal Column Fiber – Ion Channel Kinetics .....	143
Appendix C: Simplified Model of Spinal Cord Stimulation .....	145
References.....	149
Biography.....	166

## List of Tables

Table 2.1. Thresholds obtained with the forearm model and motor thresholds reported by Slovak <i>et al</i> (2013).....	66
--	----

## List of Figures

Figure 1.1 Examples of kilohertz-frequency waveforms used in transcutaneous electrical stimulation. ....	25
Figure 1.2. Examples of responses of axons to KHF stimulation. ....	36
Figure 1.3. Illustration of conduction block. ....	40
Figure 1.4. Dielectric parameters of skin, fat and muscle. ....	43
Figure 2.1. Model of transcutaneous nerve stimulation. ....	56
Figure 2.2. Decay of potentials in the modeled tissue as a function of frequency. ....	60
Figure 2.3. Stimulation threshold as a function of carrier frequency of the Transdermal Amplitude Modulated Signal (TAMS) for 7 different geometries of the volume conductor model. ....	62
Figure 2.4. Strength-distance relationship for the Transdermal Amplitude Modulated Signal (TAMS) and rectangular pulses. ....	63
Figure 2.5. Transmembrane voltage response to sinusoidal stimulation. ....	64
Figure 2.6. Motor thresholds measured experimentally and estimated with model. ....	65
Figure 2.7. Waveforms from the model of the Slovak <i>et al</i> (2013) experiment. ....	66
Figure 3.1 Phantom model of transcutaneous electrical stimulation. ....	75
Figure 3.2. Conductivity of phantoms. ....	79
Figure 3.3. Conductivity of skin and organic and synthetic materials used as skin phantoms. ....	79
Figure 3.4. In vitro measurements of impedance. ....	80
Figure 4.1. Stimulation waveforms. ....	85
Figure 4.2. In vivo stimulation of rat sciatic nerve. ....	88
Figure 4.3. Simulation of nerve stimulation. ....	91
Figure 4.4. Evoked EMG activity. ....	93
Figure 4.5. Evoked CAP activity. ....	94

Figure 4.6. Membrane parameters during stimulation with pulse, sine, TAMS and TAMS1c2. ...	96
Figure 5.1. Illustration of the model of extracellular potassium concentration. ....	108
Figure 5.2. Human model of spinal cord stimulation using kilohertz-frequency signals. ....	114
Figure 5.3. Metrics of spike train similarity.....	116
Figure 5.4. Action potential shape and conduction velocity of DC fibers.....	119
Figure 5.5. Current-distance relationship of DC fibers.....	120
Figure 5.6. Strength-duration relationship of DC fibers. ....	121
Figure 5.7. Recovery cycle of DC fibers. ....	122
Figure 5.8. Effects of potassium diffusion.....	123
Figure 5.9. Activation thresholds for two patients using conventional SCS. ....	124
Figure 5.10. Activation thresholds for two patients using KHF-SCS.....	125
Figure 5.11. Block thresholds for two patients using KHF-SCS. ....	125
Figure 5.12. Vector strength of DC fiber activity. ....	127
Figure 5.13. Similarity of spike activity of DC fibers. ....	128
Figure 5.14. Effects of ion currents on the recovery cycle of the fiber model.....	132

## **Acknowledgements**

I am extremely grateful to have had the opportunity to work with Warren. He is an incredibly creative, hardworking researcher that I consider a true role model of what I would like to become as an independent investigator. Throughout my PhD, Warren not only supported my work and encouraged me in every path that I pursued, but also gave me gazillion (I learnt this word from him) of ideas without which I would have not been able to achieve my goals. I really appreciate the opportunity he gave me to work with him, and I am grateful for all what I learned from him in class, in the lab, and during the countless discussions of research work, from minor details to broader research questions.

I would also like to thank the members of the Dissertation Committee, Drs Craig Henriquez, Marc Sommer, Patrick Wolf, and Nandan Lad, for their valuable input and insights over the years.

For the work in Chapter 5, we worked together with John Janik from Stryker Corporation, and I would like to thank him for the enriching biweekly discussions that witnessed the development of the fiber model.

I am also very grateful to the members of the Grill lab for making it an intellectually stimulating work environment. I really enjoyed the many discussions about science -and tons of other topics- that I had with Bryan Howell, which helped me refine my knowledge of the physics behind neural engineering. One of these discussions, in fact, ended up as a publication. Plus, for the work in Chapter 5 I used his model, and he kindly facilitated all the code. I feel really lucky to have shared office with Nikki Pelot. She gave me great feedback in many parts of my work, help me with many details of modeling, and was always there to discuss basic science or detailed

research that reminded me of the importance of critical thinking for my work. Nate Crosby taught me how to perform the spinal surgery with incredible patience and dedication, and provided me data to compare with my model predictions (Chapter 5). He was always happy to discuss about spinal cord stimulation or any other topic, and I learned a lot from him in our biweekly meetings. Chris Langdale was also very patient to teach me the most of what I know of animal handling and surgery. He spent plenty of time to ensure that I felt confident performing surgeries by myself, and I truly appreciate his generous efforts to teach me these experimental techniques. I am also very grateful to Gilda Mills, who also helped me with the animal work, and offered valuable administrative assistance, including animal protocols. Tianhe Zhang provided feedback in my initial work of Chapter 5, and helped me get on board with the SCS project. Zach Danziger gave me great feedback as well, and his sharp mind always inspired me to think critically. I am most likely forgetting to acknowledge their particular contributions to this work, and I am very grateful to Brandon Swan, George McConnell, Christina Behrend, David Brocker, Meredith McGee, Chintan Oza, Jim Hokanson, Aman Aberra, Nathan Titus, Isaac Cassar, Haigreev Yedla, and Karthik Kumaravelu.

I would also like to thank Dr Miguel Nicolelis, who received me in his lab when I first came to Duke. I might have ended in a different institution if it wasn't for his encouragement to come here, and I really appreciate the opportunity he gave me to work in his lab. Many thanks also to the people from the Nicolelis lab, especially to Mikhail Levedev, who not only taught me a lot of brain-machine interfaces, neuroscience and primate research, but also with his advice gave me the initial push that one needs to succeed in a PhD program. I also learnt a lot from Joey O'Doherty; through insightful discussions with him I came up with ideas for an experiment.

Many thanks to Je Hi An, Andy Fuller, Peter Ifft, Katie Zhuang, Solaiman Shokur, David Schwarz, Gary Lehew, Miguel Vieira, Laura Oliveira and Tamara Phillips.

I would also like to thank my parents, Malu and Eugenio, for supporting me throughout my studies from the very beginning. My education, which allowed me to get here in the first place, I owe to them. My accomplishments are also theirs, and I will be always grateful for all the efforts they put on my education that are crowned with my PhD. Many thanks as well to my sisters for contributing to my parents' efforts and for being as supportive throughout: Barbara, Vale, and Nadia. I would also like to thank the support of Ange, Jose, Rafa, and my parents-in-law, Raul and Dafne. Friends were also very supportive during my PhD, and in particular I would like to thank Rene, who gave me great advice many times.

This work would have not been possible without the continuous and selfless support, encouragement and love of my wife Marce. She was willing to move to a different country, with a different language, to spend nearly six years of her life without really knowing in advance what she could do here (it ended up being a terrific experience for her as well). Marce gave me everything one could ask to carry on the tremendous task of completing a PhD. She cheered me up in moments of struggle, she joined me in moments of happiness. In sum, my adventure was her adventure, and so this work resulted from her perseverance as well. Plus, she actually facilitated my work with important little details like giving me rides to work many times a week. I am also very grateful to my little daughter, Sofi, simply for being there and inspiring me to continue to work hard. De todo corazón, mi niñas, les agradezco el haber hecho posible que terminara este trabajo. Esta tesis es tanto de Uds como mía.

This work was supported financially by a Fulbright-CONICYT Chile scholarship (2010-2014), Stryker Corporation, and Ethicon, Inc.

# **Chapter 1: Introduction and Overview**

## ***1.1 Introduction***

Electrical stimulation therapies are used to treat the symptoms of a variety of nervous system disorders and diseases including chronic pain, Parkinson's disease, and epilepsy, among many others [1]. In these therapies, electrical currents intended to modulate the activity of nerve fibers or neurons are delivered to the tissue through an implanted or a surface electrode. The most common modality of stimulation is a train of pulses delivered at a rate of few tens of Hz, and in some cases, up to few hundreds of Hz. For example, typical pulse rates for spinal cord stimulation and deep brain stimulation, two mainstream electrical stimulation therapies, are 50 and 130-185 Hz, respectively [2, 3]. There is an increased interest in stimulation of nerve fibers using kilohertz-frequency (KHF) signals due to the potential to penetrate deep in the tissue and the ability to block action potential conduction. Transcutaneous stimulation, for example, may be optimized by overcoming the impedance of the skin and the underlying tissues. Further, use of KHF waveforms for spinal cord stimulation shows great promise for the treatment of chronic pain, and KHF signals are being investigated for the treatment of obesity, via stimulation of the vagus nerve, and amputee pain, via peripheral nerve stimulation. The purpose of this review is to assess the effects of neurostimulation using KHF signals on the tissue and on nerve fibers and cells, describing what is known about this modality, and to review some applications that use KHF waveforms.

This review is organized as follows. First, we review specific applications that employ KHF waveforms, with a focus on transcutaneous electrical stimulation and spinal cord stimulation. The former has a long history using signals in the low KHF range, whereas the latter only recently introduced a KHF waveform to treat pain without paresthesia, a signature of

conventional spinal cord stimulation. Next, we describe the responses of axons and cells to KHF signals, including block of the conduction of action potentials. We then present the effects of the dielectric parameters on the potentials in the tissue, and how dispersion and other effects affect the distribution of potentials when a KHF electric field is applied to the tissue. Finally, we describe some technical aspects that researchers should consider if they are to equip electrical neuromodulation devices with KHF waveforms. In this review we use the “Hertz” unit indistinctly for pulse trains and sinusoids. For pulse trains, we use frequency to refer to pulse rate, and we note that a complete description of a pulse train should include at least, in addition to the frequency, the pulse duration and the number of phases per pulse (monophasic/biphasic). Further, we refer to “stimulation” with KHF signals, even though the intended or actual response may be conduction block, rather than activation.

## ***1.2 Clinical applications of kilohertz-frequency stimulation***

Kilohertz-frequency (KHF) signals are used in a number of clinical applications including spinal cord stimulation and peripheral nerve stimulation for the treatment of chronic pain, transcutaneous electrical stimulation for physical therapy, vagus nerve stimulation for the treatment of obesity, transcranial alternating current stimulation for the treatment of brain cancer, and deep brain stimulation for the treatment of motor symptoms in Parkinson’s disease.

### **1.2.1 Spinal cord stimulation for chronic pain relief**

Spinal cord stimulation (SCS) is a treatment for chronic pain, most commonly failed back surgery syndrome [4]. In SCS, an implanted pulse generator delivers electrical stimulation to the dorsal columns (DCs) via electrodes placed in the epidural space of the spinal cord. The stimulation parameters are selected based on a combination of paresthesia location, pain relief and comfort, and the parameter selection can have a significant impact on clinical outcomes [5]. Typical parameters used in SCS are: pulse duration 100-300  $\mu$ s, pulse rate ~50 Hz, amplitude in

the range of a few mA to a few tens of mA [2].

Recently, KHF-SCS was proposed as a means of providing pain relief without paresthesia [6–9], and clinical trials showed improved efficacy of KHF-SCS as compared to traditional SCS, with greater reduction in overall pain score and up to twice as many responders [6, 9]. However, there is controversy regarding the clinical outcomes as in another study, KHF-SCS provided no improvement over sham, *i.e.*, no stimulation, although differences in frequency of stimulation (5 versus 10 kHz), pulse duration and other parameters may explain the disparate results [10]. In KHF-SCS, short duration biphasic pulses of 30  $\mu$ s/phase are delivered at 10 kHz, with amplitudes in the range of 0.5 to 5 mA [6], and pulse rates of 1.2 kHz and 5 kHz have been used as well [10, 11].

The mechanisms of KHF-SCS are not understood. A key piece of the puzzle that needs yet to be determined is how the main target of the SCS therapy, *i.e.*, the DC axons, respond to the KHF signal, and therefore experimental and model-based quantification are warranted. It appears that traditional SCS and KHF-SCS involve different spinal and/or supraspinal mechanisms, since 50 Hz SCS, but not KHF-SCS, inhibited sensitization to noxious stimuli in dorsal horn projection neurons that are used as a proxy of pain suppression [12], although KHF stimulation of dorsal root fibers did have a suppressive effect on these neurons [13]. Rat models of pain demonstrated analgesic effects of SCS of 50 Hz, 1 kHz and 10 kHz, via reduction of mechanical hypersensitivity [14], and the 10 kHz signal produced a stronger effect with earlier onset [12]. Further, recordings from dorsal column nuclei (DCN) - relay centers receiving inputs from DC axons - showed massive activation during 50 Hz SCS, and no activation during KHF-SCS, although the latter was of lower amplitude [14]. The absence of DCN activity during KHF-SCS at analgesic amplitudes is suggestive of DC axon unresponsiveness, *i.e.*, the KHF-SCS signal may not activate DC axons. However, low frequency (<50 Hz) SCS elicits a variety of DCN

responses, including inhibition [15], and thus KHF-SCS-induced DC axon discharges may be accompanied by suppression of DCN activity. Further, for suppressed DCN cells, the coherence to peripheral nerve stimulation using Poisson pulse trains declines rapidly with increasing frequency [16], and thus activation patterns with KHF content may generate highly asynchronous DCN activity. This may in part explain the lack of paresthesia during KHF-SCS as non-tonic SCS stimulation of variable pulse durations, which apparently triggered burst-like asynchronous activation patterns, produced more natural percepts than tonic SCS [17]. Alternatively, KHF-SCS may block the conduction of DC axons, and this is also consistent with DCN quiescence. However, DCN responded to tactile stimuli during KHF-SCS [14], indicating that at least some DC axons were not blocked.

Computational models of SCS provided insights into both anatomical substrates and geometric aspects of the SCS electrodes important to DC activation [2, 18], leading, for example, to electrode designs more capable of targeting specific dermatomes. A finite element model of human SCS suggested that only large DC axons (15  $\mu\text{m}$  diameter) are activated by the KHF-SCS signal using amplitudes within the range used clinically (0.5 – 5 mA), and block thresholds were about twice as large as activation thresholds [19]. Further, the amplitude to activate smaller axons increased substantially, and activation thresholds for fiber diameter  $<8 \mu\text{m}$  were higher than 10 mA even at the superficial edge of the spinal cord. Since the vast majority of human DC axons have diameters of few  $\mu\text{m}$  [20], it appears that only few large, superficial axons are activated during KHF-SCS, a hypothesis also advanced for traditional SCS [21]. If the KHF-SCS waveform activates a small group of DC axons, it is necessary to quantify the firing activity of these axons, and determine whether the activation patterns 1) can inhibit pain signals, and 2) evoke no paresthesia. Computational models may help determine answers to these questions, and

our approach is to develop a model of a DC axon with enough detail to represent the excitation properties of DC axons.

### **1.2.2 Transcutaneous electrical stimulation for physical therapy**

Neuromuscular stimulation, delivered in the form of transcutaneous electrical stimulation (TES), is used in physical therapy to improve muscle strength, increase range of motion, and decrease atrophy [22]. The goal is to activate motor nerve fibers and elicit muscle contractions and to bypass cutaneous nociceptors or other sensory fibers that can produce discomfort. In TES, surface electrodes deliver currents across the skin, and since the impedance of the skin declines by several orders of magnitude between the hundreds of Hz to the hundreds of kHz range [23], TES for motor stimulation may be optimized using KHF signals. Consequently, different TES waveforms with a fundamental frequency in the kHz range have been proposed for neuromuscular stimulation, mainly sinusoidal ac with some type of modulation (Figure 1.1). A more extensive review of KHF-TES for motor stimulation can be found elsewhere [24].

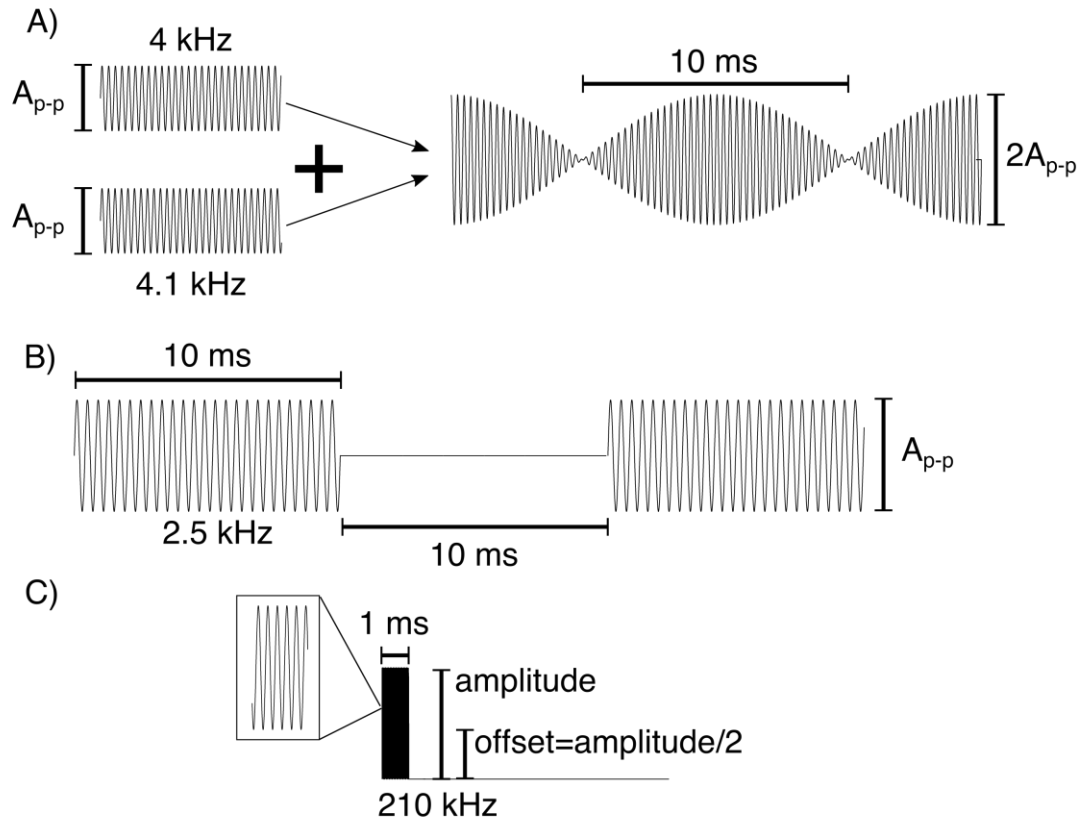


**Figure 1.1 Examples of kilohertz-frequency waveforms used in transcutaneous electrical stimulation.**  
 A) Interferential current. B) Russian current. C) Transdermal amplitude modulated signal.

One of the earliest KHF-TES modalities is the interferential current (IFC) [25], and in addition to muscle strengthening in physical therapy, IFC was used for treatment of musculoskeletal pain [26], chronic constipation [27], and swallowing disorders [28]. IFC uses two pairs of skin electrodes placed diagonally opposed such that the paths of two independently generated KHF currents produce an interference effect where they intersect (Figure 1.1A) [24]. In IFC, sinusoidal currents of slightly different frequencies, *e.g.*, 4 and 4.1 kHz, are applied continuously at a fixed amplitude, and it is intended that motor axons experience a fully modulated signal resulting from the summation of the two sinusoids, *i.e.*, the interference effect. However, the actual stimulation signal is not known and the degree of modulation depends on

fiber location and orientation with respect to the stimulation electrodes. In fact, fibers located near the axis of one of the current paths, and far from the interference field, can experience an unmodulated signal, *i.e.*, purely KHF sinusoid. This distinctive feature of IFC seems appealing because skin receptors and other superficial sensory fibers may be blocked by an unmodulated signal while motor fibers are activated by a modulated signal, thereby eliciting muscle activation with less discomfort. This idea is supported by computational modeling that showed that some fibers are blocked and others fire continuously or in burst at the rate of the modulation frequency or higher [29]. Purely sinusoidal waves are extensively used to block the conduction of nerve fibers [30–34], but in IFC, it is unclear what fibers are subjected to the unmodulated currents. Volume conductor models may be used to determine the spatiotemporal distribution of currents for IFC [35], and coupled to model of nerve fibers, can be used to predict motor and/or discomfort thresholds. For example, we implemented a multilayer (skin, fat and muscle) model of KHF-TES including dispersion [36], and found that thresholds for single action potential matched well with experimental measurements of motor thresholds for sinusoidal bursts in the 2 – 25 kHz frequency range [37]. Similar approaches may be used to predict motor and discomfort thresholds for IFC.

The Russian current is another KHF-TES modality used in physical therapy, introduced originally for muscle strengthening in elite athletes [38, 39]. The Russian current is a 2.5 kHz sinusoidal signal modulated by a rectangular pulse train at 50 Hz with a 50% duty cycle, *i.e.*, each pulse is a sinusoidal burst of 10 ms duration (Figure 1.1B). The 2.5 kHz carrier frequency was suggested as an optimal frequency to maximize muscle torque while reducing skin discomfort, and the 50% duty cycle was favored to reduce the energy delivered to the tissue [38]. The carrier frequency may be suboptimal, however, as muscle force obtained with KHF modulated stimulation decreased monotonically with increasing carrier frequency in the 1 – 10 kHz range

[37, 40], and the Russian current provided weaker muscle contractions and torque with respect to rectangular pulses, with less or equal discomfort [41, 42].

The Russian current resembles the fully modulated IFC, but with rectangular instead of sinusoidal amplitude modulation. In contrast to IFC, however, there are no unmodulated current sources in this case, and therefore, depending on the filtering properties of tissue, it is expected that all fibers, including sensory and motor fibers, will experience a modulated waveform. This appears to be an important feature for motor fiber activation, as modulation is essential for high torque production [43]. In addition, if IFC and Russian current are applied using the same amplitude, carrier frequency, and modulation frequency, IFC generates twice as much muscular force than the Russian current [44]. The doubled force generated by IFC matches well with the additive effect within the interference field since the summation of the current paths generates twice as large currents. Regardless, it appears that both modalities are suboptimal, and the desired outcomes, force production or reduced discomfort, are likely maximized with different sets of stimulation parameters, *i.e.*, burst duration and carrier frequency [24]. Future research should be directed to determine the basis of these differences. For example, in models of TES, thresholds for motor and sensory fiber placed at different distances from the electrode may be used as proxies for force output and discomfort threshold, respectively, and the effects of stimulation waveform parameters on thresholds may be determined for a number of fiber properties that differ between fiber modality, *e.g.*, ion channels and fiber geometry.

### **1.2.3 Other clinical applications of transcutaneous electrical stimulation**

Recently, a novel waveform called transdermal amplitude modulated signal (TAMS) was proposed for the treatment of overactive bladder [45–47]. TAMS is composed of a 210 kHz sinusoidal carrier added to a traditional rectangular pulse train of half the amplitude of the carrier,

resulting in non-zero offset sinusoidal pulses (Figure 1.1C). In animals, TAMS modulated bladder activity via TES of the pudendal or sacral nerves [45, 46, 48], and depending on the frequency of the modulating waveform, both inhibitory and excitatory effects were evoked. In clinical studies, TAMS improved the symptoms and quality of life of patients with overactive bladder [47, 49]. However, experimental and computational modeling studies suggested that the KHF carrier used in TAMS does not affect nerve excitation [36, 50]. In our modeling work, we quantified thresholds for nerve fiber activation using both TAMS and traditional rectangular pulses, and we accounted for tissue dispersion effects [36]. Even though the KHF carrier generated larger potentials at a certain depth in the tissue compared to lower frequencies, the axon models were not more easily activated after adding the carrier because of the low pass filtering properties of the axonal membrane. We confirmed these results experimentally by quantifying nerve fiber activation in animals using TAMS with different sizes of the carrier, and in all cases, thresholds were no different between TAMS and pulse stimulation, in agreement with measurements of muscle contractions humans [50].

Other KHF-TES waveforms were used in clinical applications. For example, KHF-TES was applied over the ophthalmic and maxillary divisions of the trigeminal nerve for stress control, and the levels of tension and anxiety were reduced compared to a control group that received sham stimulation of lower frequency and amplitude [51]. In this application, the waveform was a biphasic pulse train with frequency ramped up from 7 to 12 kHz during the first 30 s of a 15 min stimulation time, and then ramped down from 12 to 7 kHz during the last 30 s. A different waveform was proposed to generate locomotion via TES at multiple spinal levels [52]. Bursts of 10 kHz biphasic pulses and 0.3-1 ms duration were delivered to non-injured people at cervical, thoracic and lumbar levels, which caused coordinated stepping movements with ample range of

motion at multiple joints, and these results may be used in strategies to restore motor function after spinal cord injury.

#### **1.2.4 Peripheral nerve stimulation for phantom limb pain relief**

Peripheral nerve stimulation (PNS) using KHF waveforms was proposed to relieve phantom limb pain by means of conduction block of nociceptive nerve fibers [53, 54]. Phantom limb pain is a chronic and severe residual pain in amputees that may be refractory to medication and denervation. A cuff electrode was implanted around the severed peripheral nerve of amputees proximal to a distal neuroma, the source of pain, and a 10 kHz sinusoidal signal was applied for 30 minutes as needed. Pain decreased by 75% after three months, and all subjects achieved 50% or more pain reduction in at least 50% of the treatment sessions, but these results are yet to be confirmed by a larger, longer duration pivotal study [53]. It was claimed that block of nociceptive fibers proximal to the neuroma resulted in pain relief. However, such claims require further examination. First, in the clinical trials, the amplitude was ramped up from 0 to a few volts (<10 V) during 5 min, and then plateaued at the maximum voltage for an additional 25 min. Block thresholds of large motor fibers (10 – 12  $\mu\text{m}$  [55]) of the rat sciatic nerve using sinusoidal signals are in the range of a few volts [56], and block threshold increase dramatically as the fiber diameter decreases [32]. Therefore, it seems unlikely that small diameter nociceptive fibers (< 1 mm [55]) were completely blocked by the KHF signal, and at 10 kHz unmyelinated fibers have higher block thresholds than myelinated fibers [31]. Secondly, the analgesic effects of KHF-PNS lasted in some cases up to several hours after the device was turned off, whereas conduction block using KHF signals is rapidly reversible, *i.e.*, the effects vanish within few ms [33], although longer ‘carry-over’ effects were observed that, nonetheless, lasted only a few minutes [57]. Therefore, the KHF-PNS therapy likely involves mechanisms other than conduction block, and it

may engage spinal circuits via activation, for example, of peripheral sensory fibers in a manner similar to KHF-SCS.

### **1.2.5 Vagus nerve stimulation for the treatment of obesity**

Electrical stimulation of the abdominal vagus nerve using a 5 kHz rectangular signal was proposed for the treatment of obesity [58, 59]. This therapy is based on the observation that KHF stimulation of vagal fibers that may be involved in appetite control decreased pancreatic exocrine secretion in animals, allegedly by blocking nerve conduction, and that vagotomy resulted in short-term loss of appetite [60]. While one clinical trial reported an average excess weight loss of 15% after 6 months of treatment [59], much larger studies including a control group, which received the implant without stimulation, showed that both study and control subjects lost similar excess weight after 12 months, although greater weight loss was observed in subjects that used the device more frequently [58, 61]. Conduction block of small diameter fibers ( $<1 \mu\text{m}$  [62]) of the abdominal vagus nerve using the same 5 kHz rectangular signal was demonstrated in rats [57], and complete block of unmyelinated C-fibers was achieved with amplitudes of  $\sim 8 \text{ mA}$ . In clinical applications, similar amplitudes were used, *i.e.*, 6 – 8 mA, but it is unclear whether the amplitudes from the animal study can be directly translated to humans, and a computational model of autonomic nerve stimulation suggested that the primary effect of the KHF signal was activation rather than block of small myelinated and unmyelinated axons [63].

### **1.2.6 Transcranial alternating current stimulation for the treatment of brain cancer**

Transcranial alternating current stimulation (tACS) is a noninvasive brain stimulation technique that delivers sinusoidal currents through the skull using surface electrodes, and can be targeted to different brain cortices. By synchronizing brain oscillations, tACS may improve cognition and motor performance, interfere with attention, or induce phosphenes [64]. Typical

frequencies in tACS are within the EEG spectrum, *i.e.*, 0.1 – 80 Hz, but frequencies in the low kHz range were used to increase motor cortex excitability [65]. Recently, very high KHF (100 – 1000 kHz) was used to decelerate the proliferation of different cancer cells in culture, and the optimal frequency varied across cell types [66]. These findings led to a clinical trial of 200 kHz tACS, also called TTFields, that enrolled patients with glioblastoma, a type of brain cancer. Patients treated with TTFields had a progression-free survival and a median overall survival 3 and 5 months longer than controls, respectively [67]. However, these results have been received with skepticism because of the absence of sham controls, and the lack of understanding of the mechanisms of action [68]. Due to the capacitive nature of the cell membrane, the impedance of the membrane at very high frequencies (200 kHz) is close to zero, and the changes in transmembrane voltage generated by such signals are likely to be very small [69]. Instead, TTFields appears to oppose cell division by means of a phenomenon called dielectrophoresis, in which a non-uniform electric field inside the inhomogeneous composition of dividing cells exerts forces on intracellular molecules that participate in cellular division [66].

### **1.2.7 Deep brain stimulation for the treatment of Parkinson's disease**

Deep brain stimulation (DBS) is a well-established therapy in which electrical currents are delivered to deep structures in the brain to treat, most commonly to treat the motor symptoms of movement disorders such as Parkinson's disease, essential tremor and dystonia [70]. DBS effectiveness is strongly related to frequency, and it has been shown that 1 kHz DBS is as effective for tremor suppression as the commonly used 130 Hz DBS [71]. However, frequencies that are too low (<50 Hz) and too high (> 2 kHz) are ineffective. One hypothesis of the frequency-dependent effects of DBS is the “informational lesion” that postulates that DBS overrides the pathological neuronal activity by regularizing neural activity [72]. In a computational model of DBS, KHF stimulation (>2 kHz) reduced the regularity of firing as

quantified using the entropy, and this result appears to explain the loss of effectiveness for tremor suppression using frequencies  $> 2$  kHz [73].

### **1.3 Neural responses to kilohertz-frequency stimulation**

The responses of axons - and other neural elements - to kilohertz-frequency (KHF) electrical stimulation can vary significantly, depending on signal amplitude, distance to the electrode, electrode geometry, and frequency of stimulation [73–78]. In general, for stimuli of large enough amplitude, two broad categories of responses are observed. First, the KHF stimulus may generate firing activity [76, 77], and we refer to this response as *activation*. Secondly, the conduction of action potentials may be arrested by the KHF stimulus, *i.e.*, *conduction block* [33]. We note that block is typically accompanied by onset activation immediately after the signal is turned on [79]. However, in contrast to activation, this onset response is short lasting and represents a transition from rest to block.

In this section, we discuss three main features of neural responses to KHF stimulation. The first characteristic is straightforward, but not always appreciated. In contrast to stimulation with frequencies commonly used in electrical neuromodulation ( $<100$  Hz), the activated axon is unable to fire for each pulse or cycle of the KHF signal, and the firing rate does not exceed a certain maximum. We will examine some of the electrophysiological properties that determine the response of an axon to repetitive stimulation, which may contribute to firing characteristics under KHF stimulation. Secondly, the KHF-evoked activity exhibits a non-monotonic relationship with stimulus amplitude, and in many cases asynchronous firing activity may be evoked. Next, we will comment on the adaptation of the response to the KHF signal, *i.e.*, the firing activity declines as time progresses. Finally, KHF stimulation can block the conduction of action potentials, and this effect is not observed using low frequency neurostimulation. We will discuss the conditions under which block can be achieved, and the features of conduction block,

including dependence of block thresholds on fiber diameter and signal frequency, reversibility, and the onset response.

### **1.3.1 Firing rate differs from stimulation frequency**

For frequencies from a few Hz to tens of Hz, axons are, in general, able to fire in response to each pulse or cycle of stimulation with large enough stimulus amplitudes. Models and experimental measurements demonstrated a one-to-one relationship between firing rate and stimulation frequency of up to a few hundreds of Hz [77, 80], and in some cases, more than one action potential per cycle was elicited [81, 82]. As the frequency of stimulation increases, however, axons are not able to follow the rapidly repeating stimuli, and the instantaneous firing rate plateaus. For instance, squid axons fired every “second, third or fourth current maximum” in response to 1 kHz sinusoidal stimulation [81]. Peak firing rates as high as ~800 spikes/s were recorded in peripheral motor and sensory axons *in vivo* in response to KHF stimulation [76, 77], but in general maximum firing rates are in the order of few hundred of Hz.

Certain electrophysiological properties determine how nerve fibers respond to repetitive stimulation. First, after a nerve fiber fires an action potential, the fiber is unable to fire a second action potential during a time window known as the absolute refractory period. The refractory period, ranges between 0.7 and 2 ms in peripheral nerve fibers [83], and imposes an upper bound on the firing rate between 500 and 1,400 spk/s. Secondly, after the absolute refractory period and before recovering baseline excitability, the axon experiences periods of supra- and sub-normality, in which it is easier or more difficult to activate, respectively. This property, termed the recovery cycle [84], can be recorded by measuring the threshold for a second stimulus pulse applied after a first (conditioning) supra-threshold stimulus pulse. Thus, during repetitive stimulation, the axon response to a particular pulse will depend on the response history to recent pulses. In peripheral

axons, baseline excitability returns after about 100 ms [84–86], and this is consistent with firing rate fidelity to stimulation pulses for frequencies  $<100$  Hz.

The ability of a nerve fiber to respond to ac stimulation with persistent excitation received attention since the early twentieth century [87–89]. It was postulated that the membrane voltage must exceed a threshold for the axon to fire an action potential, and that this threshold is dynamic and dependent on the recent firing history. Under this assumption, and since the membrane voltage fluctuates with the stimulation waveform, the phase angle between the voltage threshold and the induced membrane oscillations determines axonal firing [87]. Further, the phase angle depends on the “accommodation” time constant, *i.e.*, dynamics of the threshold, and the “disturbance” time constant, *i.e.*, membrane response to stimulation, and an optimal frequency is predicted for which a minimal stimulus amplitude produces steady excitation. Experimental recordings of compound nerve activity in response to sinusoidal stimulation demonstrated a non-monotonic relationship between stimulus threshold and frequency for frequencies  $<400$  Hz, and the theory predicted well the optimal frequency ( $\sim 130$  Hz) [87]. However, the theory does not account for the refractory period, and this may explain the deviation for frequencies higher than 400 Hz as this frequency range roughly corresponds to inter-pulse intervals in the range of refractory period measured in peripheral axons. Further, the refractory period exhibits high stochasticity due to the increased noise level of voltage-gated sodium channels during this period [90], which accounts for macroscopic threshold fluctuations to repetitive stimulation. Stochastic sodium channels were incorporated into models of auditory nerve fibers, and asynchronous firing activity, termed “pseudospontaneous” activity, was obtained using KHF stimulation [91]. However, channel stochasticity is not required for asynchronous firing as fiber models with deterministic ion channels can also exhibit high variable firing patterns [73].

### 1.3.2 Activation varies non-monotonically with stimulus amplitude

As the stimulus amplitude is increased above threshold, the *activation level* increases to a maximum, and then decays before complete block is achieved. We refer to activation level as a measure of response strength, *e.g.*, the total number of spikes evoked by the KHF stimulus within a time interval or, equivalently, the average firing rate. The non-monotonic relationship between activation level and stimulus intensity was demonstrated experimentally in peripheral nerve fibers and CNS cells [76, 77, 92]. The average firing rate was quantified for single unit recordings from cat lumbar dorsal roots *in vivo* in response to voltage-controlled stimulation of the tibial nerve using a 20 kHz sinusoid (Figure 1.2A) [76]. As the amplitude of the ac signal was increased, the average firing rate increased from ~200 spikes/s to a maximum of ~500 spikes/s, and the responses were rhythmic. Further amplitude increments reduced the firing rate, and the activity switched to a random pattern, although it was not quantified how aperiodic the activity was. Finally, for very high stimulus amplitude, the firing rate dropped to zero and action potential conduction, as tested applying a distal stimulus, was blocked. The average firing rate seemed to conceal the initial activity, however, as block stimuli are frequently accompanied by an onset activation [33]. These findings appear to apply over a broader range of frequencies and for different waveforms, as in motor fibers of the cat sciatic nerve, similar results were obtained using pulse trains of 50  $\mu$ s delivered at 1 – 10 kHz [77].

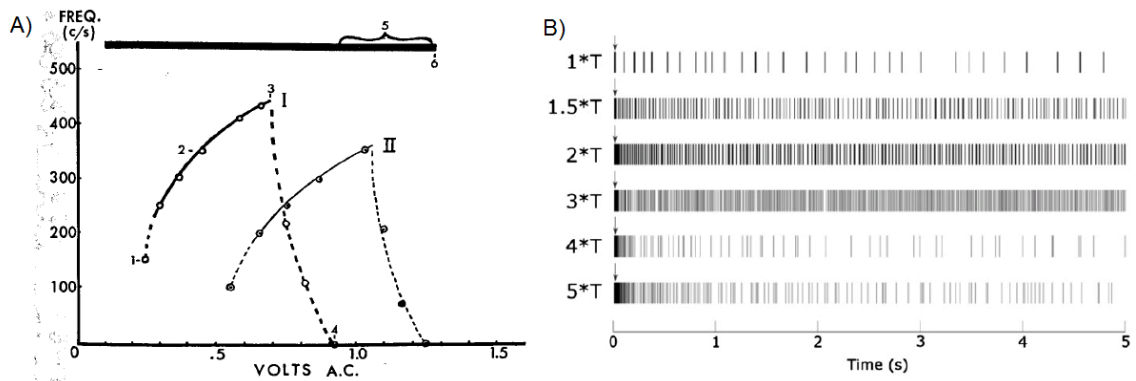


**Figure 1.2. Examples of responses of axons to KHF stimulation.**

A) Average firing rate as a function of stimulus amplitude for two dorsal root axons. The stimulus was a 20 kHz sinusoid. Adapted from [76] with permission. B) Raster plots of the firing activity of a retinal cell during stimulation using a pulse train of 2 kHz for 5 s at different stimulus intensities as labeled on the left. T was defined as the amplitude for which 50% of the pulses elicited spikes. Adapted from [92] with permission.

Retinal cells exhibited amplitude-dependent KHF-evoked activity as well [92], and this finding was used for selective activation of different retinal cell types, *i.e.*, ON- and OFF- center ganglion cells [93, 94], a feature that may be a critical to evoke more biologically relevant visual percepts in retinal prostheses [95]. Pulse trains of 2 kHz were applied to rabbit retina for 5 s (Figure 1.2B), and the average firing rate of two different cell types peaked at different stimulus amplitudes in the 0 – 150  $\mu$ A range [92]. Further, an amplitude modulated 2 kHz waveform with a baseline amplitude level and a triangular envelope, produced transient opposite responses during the amplitude shift: the firing activity of ON cells increased, whereas that of OFF cells decreased [93]. The basis of this differential activation is not understood, and it was hypothesized that greater  $K^+$  channel expression may facilitate the onset of depolarization block, thereby shifting the peak firing activity toward lower amplitudes [94]. Potassium-mediated KHF block was proposed for a model of frog unmyelinated fiber [96], but models of mammalian axons suggested that KHF block is mediated by  $Na^+$  inactivation [97]. Further, there is no experimental evidence of differential  $K^+$  expression in ON and OFF ganglion cells.

The basis for the relationship between activation level and stimulus amplitude is yet to be determined. In recordings from frog single motor axons *in vitro*, the mean membrane potential was depolarized during stimulation with rectangular current-controlled ac at frequencies between 4 and 20 kHz, depolarization increased with increasing stimulus strength, and this effect vanished after applying tetrodotoxin, a Na<sup>+</sup> channel blocker [98]. Na<sup>+</sup>-mediated membrane depolarization has also been related to KHF block [33, 97], and therefore, the falling phase of the activity-amplitude relationship may be facilitated by depolarization mediated Na<sup>+</sup> influx and subsequent inactivation of voltage-dependent Na<sup>+</sup> channels. However, it is unclear how the rising phase of the activity-amplitude relationship would be originated in this case since depolarization increased monotonically with stimulus strength. In addition, further research is needed to determine the effects of stimulation waveform parameters and fiber properties on the activity-amplitude relationship. For example, model work suggested that suppression of firing activity is dependent on the ratio of stimulation frequency and amplitude [99]. Further, experimental measurements indicate that different stimulation frequencies produce similar increments in activity level [98], and that the relationship between activity level, amplitude, and frequency shifts to higher amplitudes with decreasing fiber diameter [76], but these effects have not been thoroughly examined.

### **1.3.3 Responses to kilohertz-frequency signals exhibit adaptation**

The firing activity in response to KHF stimulation decays as time progresses, *i.e.*, the responses exhibit adaptation, for a wide range of frequencies and amplitudes. This observation was well documented by Bowman and McNeal [77], who recorded from single alpha-motoneurons of cat sciatic nerves using silver microwires, and applied stimulation via two distal cuff electrodes: one delivered voltage-controlled pulse trains of 0.1 to 10 kHz, and the other, a test pulse. For frequencies below 1 kHz, the axons fired at the same rate or at sub-harmonics of

the stimulation signal, and the discharge rate often decreased as time progressed beyond a few minutes. At frequencies between 2 and 10 kHz, the axons initially fired at several hundreds of spikes/s, but stopped firing after a few seconds or minutes in some cases. Above a certain stimulus amplitude, test stimulation applied distally failed to propagate, indicating that the axons were blocked, but recovered full conduction within seconds after cessation of the KHF signal. Adaptation to KHF stimulation was demonstrated in auditory fibers as well. The firing rate as a function of time in response to 1 and 5 kHz pulse trains was well described by an exponential decay with two time constants [100]. It was proposed that adaptation in auditory nerve fibers is produced by hyperpolarization-activated cation channels (HCN) and slow  $K^+$  channels in the node of Ranvier [101]. However, HCN channels have been identified in somas rather than nodes of spiral ganglion neurons [102] and in the internode of peripheral nerve fibers [103], and therefore it is unlikely that HCN channels are major contributors to adaptation. Other work postulated that adaptation is mediated by  $K^+$  accumulation [104]. This hypothesis is supported by measurements in hippocampal slices showing activity-dependent increases of extracellular  $K^+$  concentration that correlated well with block of axonal conduction [105]. In our work, we implemented a model of a dorsal column axon that included dynamics of extracellular  $K^+$  concentration, and we observed similar results. Further, the potassium dynamics were necessary to replicate the time-decaying firing rate of dorsal column axons recorded in response to KHF SCS.

#### **1.3.4 KiloHertz-frequency signals can block the conduction of action potentials**

One of the most distinctive effects of KHF stimulation on nerve fibers is conduction block, and this effect might be effective for many clinical applications. KHF conduction block was extensively reviewed elsewhere [33], and in this section we will briefly summarize its basis

and the main experimental and modeling findings. To measure nerve conduction block, the primary strategy is to apply the blocking signal to a section of the nerve and test nerve conduction using a second electrode to deliver suprathreshold pulses at a distance from the blocking electrode (Figure 1.3). The most common outcome measure is muscle force, and sinusoidal signals are commonly used in models and animal experiments. Compound nerve action potentials (CNAP) are a more direct outcome measure of nerve activity, but since the individual fibers can fire asynchronously [76, 91], the CNAP can be attenuated by KHF signals despite fibers not being indeed blocked. One of the earliest demonstration of conduction block was reported by Tanner [106]. Tanner recorded the effects of a 20 kHz ac signal on frog sciatic nerve compound responses *in vitro* evoked by a more distal test stimulus. As the voltage of the ac signal increased, the evoked response was attenuated, and activity of larger fibers was suppressed first, followed by smaller fiber activity. The blocking effect was immediately reversed after removal of the ac signal. The last decade saw a resurgence of the interest in KHF conduction block, and a number of experimental and computational studies quantified different aspects of KHF block. Conduction block was demonstrated in peripheral myelinated and unmyelinated nerve fibers of amphibians and mammals [30, 31, 56, 57, 107, 108], and in the central nervous system [109]. Collectively, these studies demonstrated that, in general, KHF block 1) is quick acting, 2) reverses rapidly, 3) requires lower amplitudes for larger diameter fibers, 4) requires higher amplitudes for higher frequencies ( $> 2$  kHz), and 5) is accompanied by an onset activation of the fibers.

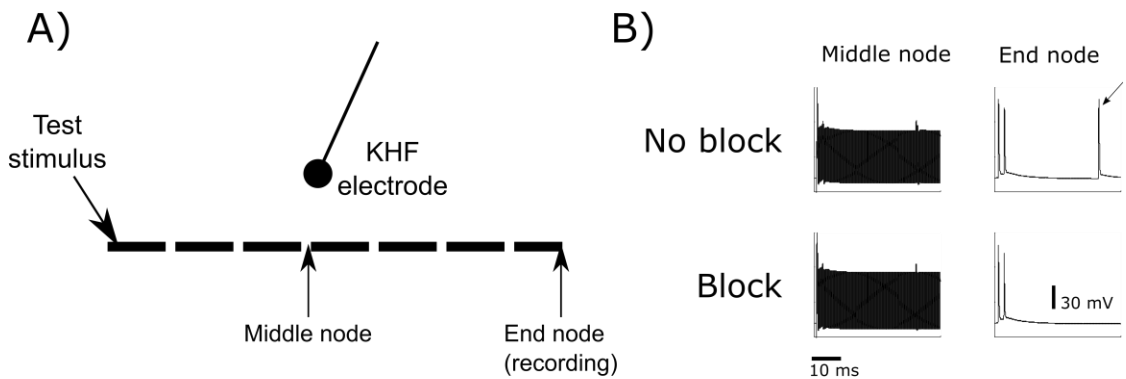


**Figure 1.3. Illustration of conduction block.**

A) Illustration of a typical model setup to demonstrate conduction block. An extracellular electrode delivers KHF stimulation above the middle node of a myelinated fiber. A suprathreshold test stimulus is applied intracellularly to one end of the fiber, and fiber activity is recorded at the other end. B) Membrane potential of the middle node and the end node for a sub-threshold (top) and a supra-threshold (bottom) block stimulus of 10 kHz. Arrow: action potential triggered by the test stimulus, *i.e.*, block was not achieved in that case.

KHF block acts rapidly and its effects reverse quickly [34, 56], although a “carry-over” effect was identified in autonomic nerves in which, after cessation of a 1-minute duration KHF signal, nerve conduction was suppressed for several minutes before recovering full conduction [57]. In addition, a typical parameter to characterize conduction block is the block threshold, *i.e.*, the minimum stimulus intensity necessary to achieve complete block. For sinusoidal signals, block thresholds increase with increasing frequency in the range of a few kHz to a few tens of kHz [30, 56], and this result has been replicated using computational models of myelinated and unmyelinated axons [32, 96, 97]. However, slow unmyelinated axons in frogs and rats exhibited a non-monotonic threshold as a function of stimulation frequency [31, 34]. Modeling work suggested that this may be an effect of pulse asymmetry [110], but it seems unlikely that the sinusoidal waveform used in the experimental studies was distorted. Instead, it may be possible that the measurements were affected by dc current contamination, as it has been demonstrated that both voltage and current waveform generators can introduce unintentional dc offset that can also produce block [111]. In this case, the non-monotonic threshold may have resulted from

dominant contributions of dc or KHF block over different frequency ranges. In addition, large diameter fibers can be blocked at lower amplitudes [32, 106], but due to the apparent non-monotonic threshold of small diameter fibers this relationship may reverse for very high frequencies ( $> 50$  kHz) [31].

Concomitant with the application of the KHF blocking signal is initial axon activation, and this phenomenon is called the “onset response” [33]. The duration and number of action potentials in the onset response are variable and depend on the parameters of the stimulation signal [32]. Generally, the onset response is undesirable as it can produce muscle contraction or pain, and different strategies were proposed to mitigate or eliminate the onset response, *e.g.*, combining ac and dc signals or varying the signal frequency [79, 112].

#### ***1.4 Effects of tissue electrical properties on potentials and implications for kilohertz-frequency stimulation***

The changes in the transmembrane potential of a neuron depend on the spatiotemporal properties of the applied field and the electrical properties and morphology of the neuron [113]. The electric field is determined by the electrical properties of the extracellular tissue, *i.e.*, conductivity and permittivity. In the frequency range commonly used for nerve stimulation, tissues are typically considered as purely resistive, and capacitive, inductive and propagation effects are neglected through the quasi-static assumption [114]. However, for kilohertz-frequency (KHF) stimulation this assumption may not be valid. In this section, we comment on the dependency of tissue conductivity and permittivity on frequency, *i.e.*, dispersion. Next, we discuss the effects of incorporating capacitive effects and dispersion on models of neurostimulation and how they may affect predictions of thresholds and other outcome measures. We then briefly examine the effects of the electrode-tissue interface on the potentials, and finalize

with a short note of how to add dispersion to physical systems to measure KHF potentials more accurately.

### 1.4.1 Tissue conductivity and permittivity exhibit dispersion

Living tissues exhibit dispersion, *i.e.*, the conductivity increases and the permittivity decreases with increasing frequency [115]. The tissue can act as a filter [116], and this filtering can influence the magnitude and time course of the potentials in the tissue and thus affect the pattern of resulting nerve fiber stimulation. The dielectric parameters of a number of living tissue, including bone, blood, brain, muscle, fat, skin, and others, have been extensively documented from dc to the GHz range (Figure 1.4) [117–120], and the parameters were modeled using  $n$  dispersive regions [121]:

$$\boldsymbol{\varepsilon}_c(\boldsymbol{\omega}) = \boldsymbol{\varepsilon}_\infty + \sum_{i=1}^n \frac{\Delta\varepsilon_i}{1+(j\boldsymbol{\omega}\tau_n)^{(1-\alpha_n)}} + \frac{\sigma_i}{j\boldsymbol{\omega}\boldsymbol{\varepsilon}_0} \quad (1.1)$$

where  $\boldsymbol{\varepsilon}_c$  is the complex permittivity,  $\boldsymbol{\varepsilon}_\infty$  is the permittivity as  $\boldsymbol{\omega} \rightarrow \infty$ ,  $\sigma_i$  is the static conductivity,  $\tau$  is the relaxation time constant, and  $\alpha$  is the distribution parameter. These experimentally recorded data are valuable for developing computational models to quantify more accurately the effects of electric fields on tissues, and ultimately, on neurons.

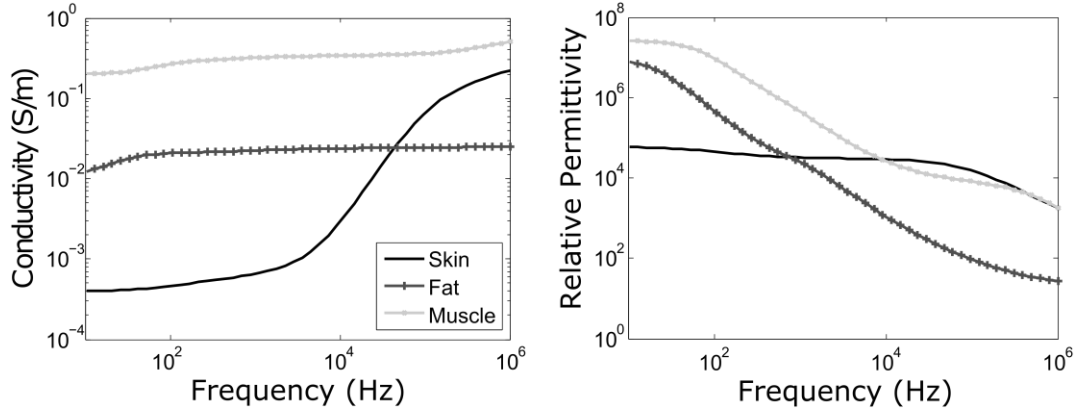


**Figure 1.4. Dielectric parameters of skin, fat and muscle.**

Conductivity and permittivity are plotted as a function of frequency. Adapted from [118].

In the general case, the potential is calculated by solving the Helmholtz equation:

$$\nabla^2 \Phi - \gamma \Phi = \frac{\nabla \cdot J}{\sigma + j\omega \epsilon} \quad (1.2)$$

where  $\sigma$  and  $\epsilon$  are the conductivity and the permittivity of the extracellular medium, respectively,  $J$  is the current density,  $\omega$  is the angular frequency of the electric field, and  $\gamma$  is the propagation constant such that  $\gamma^2 = \omega^2 \mu \epsilon (1 + \sigma / j\omega \epsilon)$ , where  $\mu$  is the permeability. However, most electrophysiological modeling studies use the quasi-static assumption and simplify equation (1.2) to Laplace's equation. The quasi-static assumption includes the following conditions [114]. First, to neglect capacitive effects,  $\omega \epsilon / \sigma \ll 1$ . Secondly, inductive effects are neglected if  $(\gamma R)^2 \ll 1$ , where  $R$  is the distance between the source and the evaluation point. Finally, the criterion to neglect propagation effects is  $(\gamma R_{\max}) \ll 1$ . In general, all three conditions are met if  $\omega$  is sufficiently low, but if the frequency is too high, then the quasi-static assumption may not be appropriate [122].

### **1.4.2 Models using kilohertz-frequency stimulation may need to incorporate capacitive effects or dispersion**

The weakest condition of the quasi-static assumption is that  $\omega\epsilon/\sigma \ll 1$ , and consequently, the capacitive effects of tissue on neural excitation may need to be incorporated in models using KHF signals. In finite element models of deep brain stimulation, the volume of tissue activated declined by 20% after including capacitive effects of the tissue and the electrode using pulses of 90  $\mu\text{s}$  [123], and for short-duration pulses ( $<20 \mu\text{s}$ ) the error of the potential calculated using a purely resistive model with respect to a full dispersive model was up to 40% [124]. However, in a homogenous, isotropic volume conductor using a point-source electrode, the error of the quasi-static approximation averaged less than 13% for pulses of 0.025 – 1 ms [122]. It appears then that for volume conductor models including greater detail of the electrode and the tissue geometry, capacitive effects may need to be incorporated for short-duration pulses. In addition, the error of the quasi-static assumption is time-dependent, peaking at the edges of the pulse, and therefore during repetitive stimulation the error may vary depending on the pulse rate [122]. Further investigation is needed to quantify the error resulting from using the quasi-static solution to calculate other axonal output measures that may be relevant for KHF stimulation, such as firing rate and block thresholds. Additionally, the membrane capacitance is also dependent on frequency [125, 126], and it has been demonstrated, using axon models, that neglecting this feature can lead to overestimation of KHF block thresholds [69].

In several models of transcutaneous electrical stimulation (TES), the potential was calculated without relying on the quasi-static assumption [35, 36, 127]. In contrast to other tissues, the conductivity of skin increases sharply with frequency, and at 100 kHz the conductivity is about 3 orders of magnitude larger than that at dc [118, 128]. Therefore, it is expected that in models of TES dispersive conductivity has the greatest effect on the potentials

and on fiber activation. In fact, in a model of TES including capacitive effects and a representation of the electrode-skin interface, permittivity had a rather small effect on the threshold and on the percentage of activated axons, with changes no larger than 5% [129]. Other models used a Fourier-based approach to calculate the potentials in a multilayer volume conductor, including dispersion and capacitive effects [35, 36]. In our model, for voltage-controlled stimulation, the potential in the deepest of three layers was about 3-4 times larger for frequencies higher than 10 kHz as compared to dc, a result that would not be expected for non-dispersive media. Nonetheless, the threshold for axon activation using the TAMS waveform composed of a very high KHF carrier on top of a non-zero offset, was the same as the threshold for a pulse. Further modelling research is warranted to quantify the effects of dispersion on fiber excitation in particular in the low KHF range, which, as we described (see section 1.2.2. Transcutaneous electrical stimulation), is frequently used in TES.

### **1.4.3 The impedance of the electrode-tissue interface decays with increasing frequency**

The impedance of the electrode-tissue interface (ETI) depends on stimulation frequency, and can also act as a filter thereby affecting the spatiotemporal distribution of potentials generated by KHF signals. Therefore, the ETI may need to be incorporated in models using KHF stimulation, especially for voltage-controlled sources. Volume conductor models incorporated the ETI via a thin-layer approximation that assumed that all current flowing across the interface had only a normal component and that the volume of the interface could be neglected [36, 124, 130]. The classical ETI model is a parallel RC circuit, in which the resistance represents Faradaic charge transfer between the electrode and the tissue, and the (double-layer) capacitor represents the non-Faradaic redistribution of charges due to the electric field [131], but it has also been described using nonlinear elements [132, 133] and as a dynamical impedance [134]. Due to its

capacitive nature, the ETI impedance decays with increasing frequency [135], and thus under voltage-controlled stimulation the current in the tissue can be larger for higher frequency due to the smaller voltage drop at the interface. For instance, the impedance of deep brain stimulation electrodes measured *in vitro* and *in vivo* at 10 kHz is up to one order of magnitude smaller than 10 Hz [136, 137]. This can have clinical implications as lower electrode impedance can result in greater volume of tissue activated [138].

#### **1.4.4 Adding dispersion to physical models to quantify potentials**

Mathematical [36, 129, 139, 140] and experimental models [141] were proposed to quantify the potentials in the volume conductor using surface stimulation, and physical systems, *e.g.*, phantoms, may be used for this task as well. Phantoms can emulate living tissue with more controlled properties than *in vivo*, and were used in a variety of biomedical applications [142, 143]. Agar-based phantoms provide a moldable solid structure from solution, and are good candidates for measuring potentials in space using, for example, a penetrating microwire [144]. However, estimation of the potentials generated by KHF signals requires a phantom model that incorporates dispersive material. For gel phantoms, graphite can add dispersion in the KHF range [142] and beyond [145]. Further, the conductivity of the gel can be adjusted by varying the concentration of a conductive solute, *e.g.*, sodium chloride [146]. In addition, anisotropy can be included by assembling several layers of isotropic material [147]. Finally, certain biological materials, *e.g.*, zucchini squash skin, exhibit dielectric properties that resemble those of living tissue, and have been used as, for example, skin phantoms [144, 148].

### **1.5 Some technical considerations**

One challenge in the use of KHF signals in clinical applications is the high energy requirement, as many more pulses are delivered per unit time compared to conventional stimulation signals [149]. Higher energy requirements result in larger batteries, shorter battery

lifetimes, and in the case of rechargeable devices, shorter intervals between recharging. In spinal cord stimulation (SCS), for example, using typical parameters, *i.e.*, 300  $\mu$ s pulses delivered at 50 Hz, the typical battery life of the pulse generator is 3-4 years for non-rechargeable and 9 years for rechargeable devices [4]. Typical parameters for KHF-SCS are 30  $\mu$ s biphasic pulses delivered at 10 kHz, and thus in this case the power consumption can be up to 40 times higher compared to the traditional signal for the same amplitude of stimulation. This would reduce the battery life to only few months if the device was continuously on, although the reported amplitudes for KHF-SCS are in general smaller than traditional SCS. Power output can be reduced in KHF-SCS by shortening the duty cycle, *i.e.*, the percentage of time that the signal is active, but it is uncertain how this would affect the utility of the therapy. As more long-term clinical studies are reported, energy constraints may appear as a relevant variable.

The risk of tissue damage by electrical stimulation is commonly assessed using the Shannon relationship in the charge density-charge per phase plane [150]. However, this relationship does not capture the possible effects of frequency of stimulation, and other factors such as duty cycle, non-uniform current distributions and electrode materials [151]. Nerve damage quantified as early axonal degeneration in chronically stimulated sciatic cat nerve [152], and central nervous system damage quantified as stimulation-induced depression of neuronal excitability during prolonged microstimulation [153], were assessed as a function of pulse rate. In both cases, lower stimulation frequency resulted in less damage, but the tested pulse rates did not exceed 500 Hz. Similarly, the current density threshold for damage of retinal cells declined by up to 7 times compared to a single pulse after increasing the repetition rate to up to 30 Hz [154]. In chronic cochlear implants delivering 1 and 2 kHz stimulation, there was no histological damage caused by stimulation, and stimulation did not affect physiological function [155]. Further, although there is a correlation between reduction in auditory nerve excitability and stimulation

rate using high amplitudes [156], excitability was not significantly reduced for amplitudes in the range used clinically for cochlear implants. These findings suggest that, under controlled conditions, KHF stimulation does not increase the risk for neural damage.

KHF signals are susceptible to dc contamination, and prolonged dc can cause neuronal damage or other effects [111]. For example, dc can produce block, and thus dc-contaminated KHF signals may achieve conduction block via dc rather than, or in addition to, via KHF generated depolarization block. If the dc offset increases with increasing frequency, then at higher frequencies dc and KHF block may act simultaneously, thereby facilitating block and reducing block thresholds. This may explain the non-monotonic relationship of block threshold with frequency observed for slow fibers in frogs and mammals [31, 34]. Inductor-based circuitry has been devised to eliminate dc contamination [111]. Finally, certain instrumentation can cause attenuation of the KHF components, and the attenuation should be measured to carefully monitor the true current output applied to the tissue [31].

## ***1.6 Introduction to dissertation and outline of chapters***

Kilohertz-frequency (KHF) neurostimulation is used in a variety of modalities including transcutaneous electrical stimulation and spinal cord stimulation, and there is an increasing number of clinical applications. Prior studies have only partially described the cellular responses to KHF stimulation, including activation and conduction block, and indicate that fiber excitation properties may determine these responses. The aim of this research was to analyze quantitatively KHF stimulation of nerve fibers. The outcomes of this study contribute to the understanding of KHF neurostimulation by establishing the importance of the tissue filtering properties on the distribution of potentials, assessing quantitatively the impact of HF stimulation on fiber excitation, and developing and validating a detailed model of a dorsal column (DC) fiber to characterize the effects of KHF stimulation on these fibers.

Chapter 2 presents a multilayer volume conductor model including dispersion and capacitive effects, coupled to a cable model of a nerve fiber that we used to quantify the effects of frequency on the distribution of potentials and on fiber excitation, in particular using the transdermal amplitude modulated (TAMS) waveform. We show that the model reproduces the threshold-frequency relationship of experimentally measured motor thresholds, and predicts that the high-frequency carrier of TAMS does not affect nerve fiber excitation.

Chapter 3 presents a physical phantom model of transcutaneous electrical stimulation that included elements representing the skin and underlying tissue, and incorporated dispersion of the electrical conductivity as required for KHF stimulation. We used both agar-based gels and biological materials, and doped the gels with graphite to add dispersion, and assembled up to three layers of material. We show that the impedance at any depth decayed with frequency, and we used these results to validate the model presented in Chapter 2.

In Chapter 4, we present the results of an *in vivo* experiment in which we applied direct stimulation to the sciatic nerve of cats and rats and measured electromyogram and compound action potential activity evoked by pulses, TAMS, and modified versions of TAMS, to quantify the effects of the carrier and the offset of TAMS on nerve fiber excitation. We show that activation with TAMS was no different from activation with conventional pulse for carrier frequencies of 20 kHz and higher, regardless of the amplitude of the carrier. We also present a computational model of nerve fiber stimulation using the same stimulation waveforms, and show that the results matched our experimental measurements. We conclude that TAMS with carrier frequencies >20 kHz does not offer any advantage over conventional pulses, even with larger amplitudes of the carrier.

Finally, Chapter 5 presents a model of a dorsal column (DC) fiber that we developed to quantify the responses of these fibers to KHF spinal cord stimulation (SCS). We also present *in*

*vivo* recordings in anesthetized rats of the strength-duration relationship and the recovery cycle of single DC fibers that we used to validate the model. We show that activation and block thresholds using the KHF-SCS signal increase sharply as the fibers are placed deeper in the DCs, and decrease for larger diameter fibers. Activation and block thresholds were higher than the amplitudes used clinically. Our results suggest that KHF-SCS activates few, large, superficial fibers, and the activated fibers fire asynchronously to the stimulation signal and to other activated fibers.

## **Chapter 2: Volume Conductor Model of Transcutaneous Electrical Stimulation with Kilohertz Signals**

### **2.1 Introduction**

Electrical stimulation of the peripheral nervous system relies, in many cases, on implantation of an electrode in proximity to the nerve and connected to an implanted stimulator. Transcutaneous electrical stimulation (TES) with external electrodes and stimulator is a noninvasive alternative for peripheral nerve stimulation that reduces the risks and costs associated with implanted devices. In TES, electrical currents in the form of rectangular pulses are applied to the skin. The pulse rate of stimulation can range from few to hundreds of Hz, and stimulation can be delivered in bursts or single pulses. High frequency sine waves on the order of a few kHz (*e.g.*, interferential currents, in which the paths of two kHz currents cross and generate an amplitude modulated signal) as well as other non-conventional waveforms (*e.g.*, H-wave, which is a biphasic exponentially decaying waveform) have also been explored, albeit with equivocal outcomes [157].

The use of high frequency waveforms for TES is suggested by the reduced impedance of the skin with increasing frequency [23]. Thus, it may be possible to reach deeper structures by adding high frequency components to the stimulation waveform. Specifically, a transcutaneous amplitude modulated signal (TAMS), in which a high frequency (210 kHz) sinusoidal carrier is modulated by a traditional rectangular pulse, was proposed as a non-invasive neurostimulation approach that can modulate bladder activity similarly to direct pudendal nerve stimulation [45, 46]. However, the mechanisms of actions of TAMS, which may differ substantially from conventional low-frequency stimulation, remain largely unexplored.

The potentials generated in the tissue by an electrode in contact with the skin are dependent on the electrical properties of the electrode-tissue interface and tissue and the geometry of the electrode and tissue. In the frequency range commonly used for peripheral nerve stimulation, tissues are considered as purely resistive, and capacitive, inductive and propagation effects are neglected through the quasi-static assumption [114]. Under certain conditions, however, these simplifications may not be appropriate [122], particularly in cases where the frequency content of the signal extends to the kHz range. In this study, we present a model of TES in which we calculate the distribution of potentials without invoking the quasi-static assumption. Although in the past many studies have used volume conductor models to estimate the potentials generated during TES, only a few have considered transcutaneous stimulation in the kHz range without relying on the quasi-static assumption [35, 129, 158].

We implemented a two-step model [159] of TES using a distributed parameter volume conductor model to quantify the spatiotemporal distribution of potentials in the tissue, and a cable model of a mammalian myelinated axon to quantify excitation of peripheral nerve fibers. Our objective was to determine whether the introduction of high frequency components, up to hundreds of kHz, made it possible to reach deeper structures, thereby facilitating nerve fiber excitation. The results contribute to understanding the mechanisms of TES with novel high frequency waveforms such as TAMS.

## **2.2 Methods**

### **2.2.1 Volume conductor model**

We calculated the potentials in a volume conductor consisting of three planar layers of tissue with frequency-dependent dielectric properties (Figure 2.1). We applied voltage or current source stimulation on the most superficial layer, including a model of the electrode-skin interface impedance. The potential in the modeled tissue,  $\Phi$ , is described by the inhomogeneous Helmholtz

equation (for a derivation of this equation see, for example, [122]), which is expressed in the frequency domain as:

$$\nabla^2 \Phi - \gamma^2 \Phi = \nabla \cdot \mathbf{J} / (\sigma(\omega) + j\omega \varepsilon_0 \varepsilon(\omega)) \quad (2.1)$$

where  $\omega$  is the angular frequency,  $\mathbf{J}$  is the current density vector,  $\sigma$  is the conductivity,  $\varepsilon$  is the relative permittivity,  $\varepsilon_0$  is the permittivity of free space, and  $\gamma$  is the complex propagation constant. Following the approach of Mesin and Merletti [35] and Farina and Rainoldi [160], we found an analytical solution of (2.1) in a multi-layer planar geometry neglecting propagation effects, as this is an appropriate approximation for living tissues [161]. We Fourier-transformed the  $x$  and  $z$  space variables into the spatial frequencies  $k_x$  and  $k_z$ , respectively. Thus, the problem was described by the ordinary differential equations in the depth  $y$ :

$$\begin{aligned} \partial_{yy} \varphi_{skin} - k_y^2 \varphi_{skin} &= 0 & 0 < y < h \\ \partial_{yy} \varphi_{fat} - k_y^2 \varphi_{fat} &= 0 & h < y < h + d \\ \partial_{yy} \varphi_{muscle} - k_{ya}^2 \varphi_{muscle} &= 0 & y > h + d \end{aligned} \quad (2.2)$$

where  $\varphi_{tissue}$  is the potential in the transformed domain,  $h$  and  $d$  are the thicknesses of the skin and fat layer, respectively,  $k_y^2 = k_x^2 + k_z^2$ , and  $k_{ya}^2 = k_x^2 + k_z^2 (\sigma_L + j\omega \varepsilon_L) / (\sigma_T + j\omega \varepsilon_T)$ , where the muscle layer was anisotropic with different conductivity and permittivity values in the transverse ( $T$ ) and longitudinal ( $L$ ) directions [118]. The solution of (2.2) is written as:

$$\varphi_{tissue}(y) = A_{tissue} \exp(k_{ya} y) + B_{tissue} \exp(-k_{ya} y) \quad (2.3)$$

where coefficients  $A_{tissue}$  and  $B_{tissue}$  are dependent on the boundary conditions, *i.e.*, they are calculated by imposing continuity of voltage and the normal component of the current density at the boundaries between layers (see Appendix A).

We incorporated the impedance of the electrode-skin interface via a thin-layer approximation [124, 130]. Assuming that all current flowing through the interface is normal to the skin surface, we imposed the following boundary condition:

$$-\mathbf{J} \cdot \mathbf{n} = (V_{source} - V_0) \cdot Y_{interface} \quad (2.4)$$

where  $V_{source}$  is the voltage delivered by the electrode (voltage-controlled stimulation),  $V_0$  is the potential on the skin surface and  $Y_{interface}$  is the admittance of the electrode-skin interface. For current-controlled stimulation we imposed continuity of the normal component of the current density on the surface of the skin. We used measurements of the impedance of the electrode-skin interface for carbon rubber electrodes with a dry-skin/pre-gelled electrode condition [162], which fall within the same range (*i.e.*, tens of  $\Omega$ ) of that used by [129] for square pulses. In the simulation of the Ward and Robertson experiment [37] (see section 2.2.5), we used the “constant phase angle impedance” model of the electrode-skin interface with the parameters reported by [163] for hydrogel-based electrodes. In this model, the interface is represented by a large resistance,  $R_p$ , in parallel with a constant phase angle impedance,  $Z_{CPA}$ , so that the admittance of the interface is expressed as:

$$Y_{interface} = \frac{1}{R_p} + \frac{1}{Z_{CPA}} = \frac{1}{R_p} + \frac{(j\omega)^\alpha}{K} \quad (2.5)$$

where  $K$  is a constant with units  $\text{Ohm}/\text{sec}^{-\alpha}$ ,  $\alpha$  is a deviation factor from the pure capacitive behavior, and  $\omega$  is the angular frequency.

For a particular depth  $y$ , we inverted the 2-D Fourier transform to obtain the potential phasor (time-harmonic),  $\Phi(\omega)$ , in the entire volume. Additionally, to compute the time-domain solution of the potential, we inverted the 3-D Fourier transform constructed by varying the

frequency over the  $[0, f_s/2]$  interval, where  $f_s$  is the sampling frequency. We used a sampling frequency at least 10-times higher than the maximum frequency of the stimulation waveform to avoid aliasing. The model was implemented in MATLAB, and was 128 mm wide ( $x$ ) by 128 mm long ( $z$ ) with a spatial resolution of 1 mm. We used disk- and rectangular-shaped electrodes, and sine and TAMS waveforms in the 0 – 210 kHz frequency range. The MATLAB code of the volume conductor model is available at [https://github.com/leonelmd/three\\_layers\\_model](https://github.com/leonelmd/three_layers_model).

For each layer, we defined the penetration distance as the length constant of a single exponential decay model of the voltage along the  $y$ -axis just below the center of the electrode (*i.e.*, a penetration distance larger than the layer thickness means that the decay of the potential across the layer was less than 63%). We fitted the data using non-linear least squares with a termination tolerance of  $10^{-6}$ , and the coefficient of determination,  $R^2$ , was larger than 0.9 in all cases.

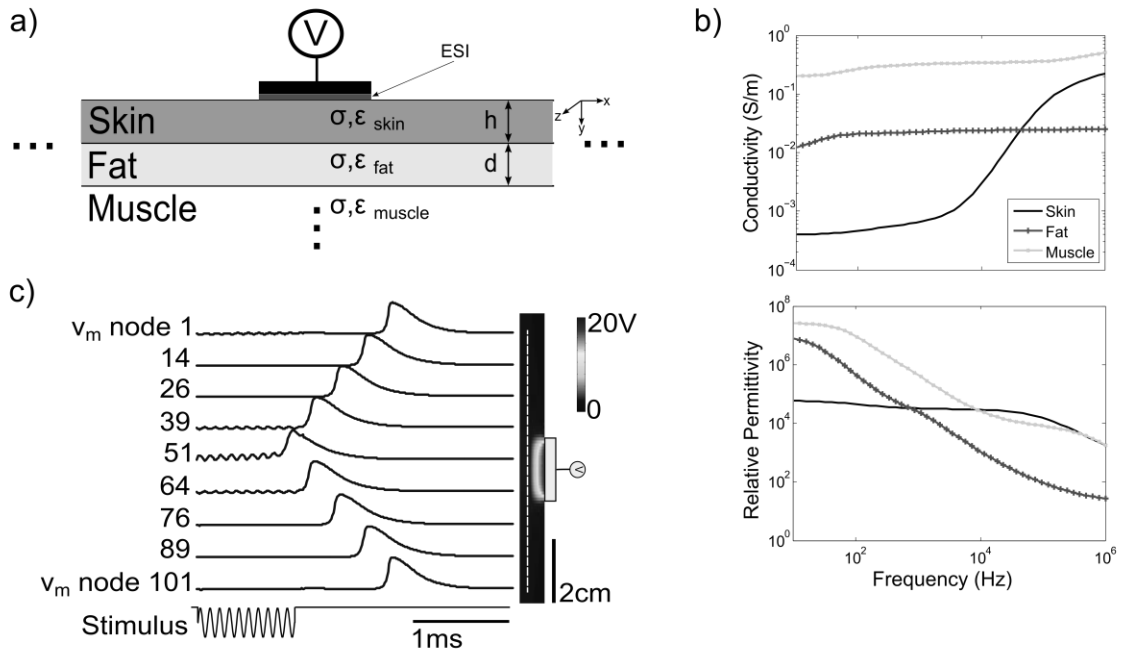


**Figure 2.1. Model of transcutaneous nerve stimulation.**

(a) A volume conductor model of three planar layers of skin, fat and muscle, a disk electrode in contact with the skin, and a distributed impedance representing the electrode-skin interface (ESI). (b) Conductivity,  $\sigma$ , and relative permittivity,  $\epsilon$ , as a function of frequency for the three tissues included in the volume conductor (parameters from Gabriel *et al* 1996b) (c) The potentials calculated from the volume conductor model were coupled to a cable model of a mammalian nerve fiber, located 7 mm from the skin surface in this example. The membrane voltage,  $v_m$ , at 9 different nodes of Ranvier is shown on the left. Skin thickness: 1.5 mm, fat thickness: 2.5 mm. Electrode diameter: 2 cm.

## 2.2.2 Frequency-dependent dielectric properties

The dielectric properties of each tissue layer (Figure 2.1) were modeled using multiple Cole-Cole [164] dispersions ( $\alpha$ ,  $\beta$ ,  $\gamma$  and  $\delta$ ) and the complex relative permittivity,  $\epsilon_c$ , was estimated as [121]:

$$\epsilon_c(\omega) = \epsilon - j \frac{\sigma}{\omega \epsilon_0} = \epsilon_\infty + \sum_{n=1}^4 \frac{\Delta \epsilon_n}{1 + (j\omega \tau_n)^{(1-\alpha_n)}} + \frac{\sigma_i}{j\omega \epsilon_0} \quad (2.6)$$

The parameters of Equation (2.6) were taken from [121]. Note that the relative permittivity is simply the real part of  $\epsilon_c$ , whereas the conductivity is determined by multiplying the imaginary part of  $\epsilon_c$  by  $\omega \epsilon_0$ .

To quantify the filtering properties of the axonal membrane, we used purely resistive media with no dispersion. In this case, the conductivity of each layer was set to the static conductivity of the layer (*i.e.*, frequency approaching zero), and we neglected capacitive effects.

### **2.2.3 Cable model of a myelinated nerve fiber**

We quantified nerve fiber excitation via TES using the McIntyre-Richardson-Grill (MRG) cable model of a myelinated mammalian axon [86]. We used 5.7 to 16  $\mu\text{m}$  diameter fibers with 101 nodes of Ranvier, and took all other parameters from [86]. We adopted the modelDB version (<http://senselab.med.yale.edu/modeldb/ShowModel.asp?model=3810>) of the MRG model in NEURON [165], and used the “extracellular” mechanism to implement extracellular stimulation. We used the Crank-Nicholson method for integration of the transmembrane voltage in response to extracellular stimulation with a time step given by the sampling frequency used for the volume conductor model. We positioned the model nerve fibers parallel to the skin surface at distances of 0.5 to 20 mm from the fat muscle boundary, with the central node randomly positioned with respect to the center of the surface electrode, but no further than half the internodal length. For the strength-distance relationship we also positioned fibers in the skin and the fat at depth multiples of 0.5 mm. Linear spatial interpolation of the potentials computed with the volume conductor model was used to calculate the extracellular voltage outside each axon compartment in the nerve fiber models. We used a binary search to estimate excitation thresholds to within  $\pm 0.1\%$ , *i.e.*, the smallest stimulation amplitude that elicited an action potential.

The coupled volume conductor/nerve fiber model of TES is illustrated in figure 1c. In this example, the stimulus generated potentials on the order of 30 V in the skin that declined to the mV range in the muscle, where the nerve fiber was positioned, and a propagating action potential was initiated in the mid-axon below the electrode. In all our simulations, we verified fiber excitation by determining whether an action potential propagated to one end of the axon.

## 2.2.4 Stimulation waveforms

We simulated voltage and current controlled stimulation using TAMS, rectangular pulses, and zero mean (*i.e.*, zero dc offset) sine waveforms. TAMS is composed of a sine carrier of 210 kHz modulated by 1 ms square pulses at a much lower pulse repetition frequency (less than 100 Hz), and with a non-zero dc component equal to half the amplitude of the sinusoid. We varied the frequency of the carrier from 100 Hz to 210 kHz, and used a sufficiently long pulse to have at least one complete sine cycle for the lowest frequency. Threshold for the TAMS waveform was defined as the dc component of the pulse, whereas for rectangular pulses and zero-offset sine waves, the threshold was the peak amplitude of the signal.

## 2.2.5 Model validation

We simulated the experimental measurements of Ward and Robertson [37] and Slovak *et al.* [50], respectively, and compared motor thresholds to our model predictions. First, we simulated voltage-controlled stimulation using the same 40 x 44 mm electrode of [37], with thicknesses of 1.5 and 2.5 mm for skin and fat, respectively, to represent the forearm [129], and applied two different waveforms: a 10 ms burst of sinusoidal stimulation and a single-cycle sine. We used the constant phase angle impedance model of the electrode-skin interface [163] as a representation of nonlinear processes that can occur at the interface. We used a frequency-dependent deviation factor,  $\alpha$ , so that  $\alpha=0.8$  for  $f < 2$  kHz and  $\alpha=0.9$  otherwise, which is within the experimentally measured range [163]. Lastly, we simulated current-controlled bipolar stimulation using 2 cm diameter disk electrodes placed 3 cm apart, and skin and fat thicknesses of 1.5 and 2.5 mm, respectively, to represent the forearm [129]. We compared the voltage across the electrodes and estimated thresholds from our model to those measured by Slovak *et al.* [50].

## 2.3 Results

### 2.3.1 Distribution of potentials and penetration distance

We quantified the decay of potential versus depth in the model tissues as a function of frequency for the geometry illustrated in Figure 2.2a. When a 1 V voltage-controlled sine waveform was applied, the potential decayed across the skin-electrode interface by less than 8% for low frequencies (<1 kHz) but by up to 36% at 10 kHz. In a purely resistive medium with no dispersion, however, the potential decayed by less than 2% across the skin-electrode interface, and this voltage drop decreased monotonically with increasing frequency. For low frequencies (<1 kHz) the voltage dropped almost entirely across the skin layer, and the voltages in the muscle were on the order of a few millivolts. However, for higher frequencies ( $\geq 10$  kHz) the potential decayed more gradually across the tissue layers and three-fold larger potentials were present in the muscle. Figure 2.2b shows representative voltage waveforms at different depths for voltage and current control using TAMS.

The frequency-dependent decay of the potential in the tissues is summarized in Figure 2.2c. While the penetration in the skin showed a very strong dependence on frequency, the penetration in muscle showed comparatively much smaller variation with frequency. As a result, and in accordance with the potential profile of Figure 2.2a, the total penetration (dotted line in Figure 2.2c) exhibited frequency-dependent behavior, which suggests that high-frequency components may reach deeper structures. In addition, we calculated the peak of the second spatial difference of the extracellular potentials between three consecutive nodes along the model axons,  $\Delta^2\Phi$ , which is proportional to the activating function that has been used as estimator of nerve fiber excitation [166, 167]. The maximum  $\Delta^2\Phi$  varied with frequency depending on the type of source. For voltage controlled TES,  $\Delta^2\Phi$  increased by nearly one order of magnitude between low

(<1 kHz) and high frequencies (>10 kHz) (Figure 2.2d), while for current-controlled TES,  $\Delta^2\Phi$  decayed monotonically with frequency.

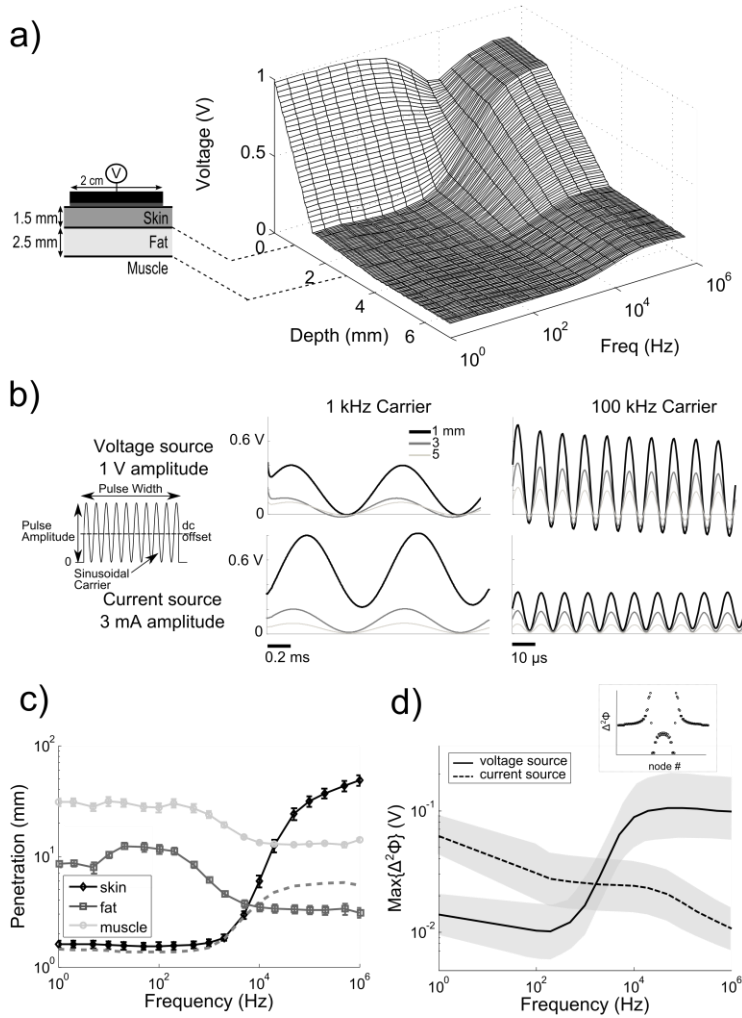


**Figure 2.2. Decay of potentials in the modeled tissue as a function of frequency.**

(a) Voltage as a function of frequency and depth along a line perpendicular to the electrode for the geometry illustrated to the left. Stimulation amplitude was 1 V. (b) Voltage waveform at different depths generated by a voltage source (top) and a current source (bottom) using the Transdermal Amplitude Modulated Signal (left) with two different carrier frequencies, 1 kHz and 100 kHz. Geometry as in (a). (c) Penetration distance (mean  $\pm$  standard error of the length constant of a single exponential decay model of the potentials) as a function of frequency for the three layers, averaged across skin thicknesses from 1.5 to 4 and fat thicknesses from 1 to 7 mm. Dotted line: total penetration. (d) Maximum of the second spatial difference of the potential,  $\text{Max}\{\Delta^2\Phi\}$ , for a 14  $\mu$ m fiber as a function of frequency for voltage- (solid line) and current- regulated (dotted line) sources. The lines represent the average over depths in the muscle layer from 0.5 to 10 mm and fat thicknesses from 1 to 7 mm, and the shaded area illustrate the range. Inset: Stereotypical second spatial difference of the potentials along a model axon (101 nodes).

### 2.3.2 Fiber excitation with TAMS and conventional pulses

The results for 7 different geometries of the volume conductor, using cathodic regulated voltage and cathodic regulated current stimulation, are summarized in Figure 2.3. Threshold was strongly dependent on the carrier frequency for both types of stimulation, with a minimum around 200 Hz. The threshold for voltage controlled stimulation did not significantly vary with the fat thickness (grey squares versus black diamonds in Figure 2.3a). However, increasing the skin thickness from 1.5 to 3.5 mm increased the threshold across all carrier frequencies. Similarly, thresholds increased with nerve depth in muscle (*i.e.*, distance from fat-muscle interface to fiber), although the changes were less pronounced than when the skin thickness was increased. Conversely, for current controlled stimulation, nerve depth had a strong influence on thresholds, whereas neither skin thickness nor fat thicknesses significantly affected thresholds (Figure 2.3b). In addition, we estimated the threshold for conventional rectangular pulse stimulation for all 7 geometries. The rectangular pulse threshold approximately equaled the dc component of the TAMS waveform with the highest carrier frequency for all geometries and for both voltage and current regulated stimulation. Additionally, as shown in Figure 2.3c, TAMS with a low frequency carrier (*i.e.* <1 kHz) delivered less energy than rectangular pulse for all 7 model variants.

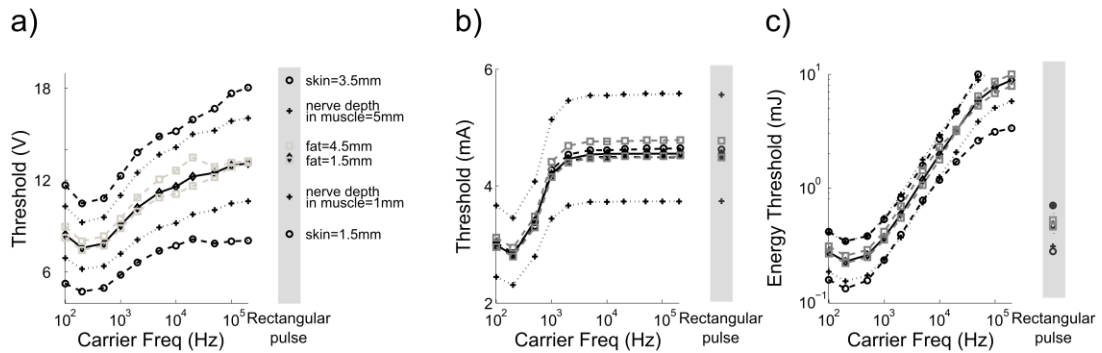


**Figure 2.3. Stimulation threshold as a function of carrier frequency of the Transdermal Amplitude Modulated Signal (TAMS) for 7 different geometries of the volume conductor model.**

(a) Voltage-controlled stimulation. (b) Current-controlled stimulation. Threshold is defined as the dc component of TAMS. (c) Same as in (a), but with threshold measured as the total energy delivered by the voltage source. Threshold for conventional rectangular pulses is shown in the shaded area and corresponds to the amplitude of the pulse in (a) and (b), and to the energy in (c). Each plot shows the thresholds for seven geometries that differed from the base condition (diamonds, solid line) in a single parameter. The base condition was: skin thickness: 2.5 mm, fat thickness: 2.5 mm, and nerve depth in muscle: 3 mm. Pulse width: 10 ms in all cases. Electrode diameter: 2 cm. Fiber diameter: 14  $\mu\text{m}$ .

Thresholds increased rapidly with nerve depth, and fibers with smaller diameters exhibited higher stimulation thresholds (Figure 2.4). For voltage and current regulated stimulation, the current-distance relationship obtained with TAMS was a vertically shifted version of that with rectangular pulse stimuli. These results did not indicate that TAMS is more effective than conventional stimulation since both activate deeper axons at higher thresholds than more superficial fibers, regardless of the nerve fiber diameter or the waveform characteristics.

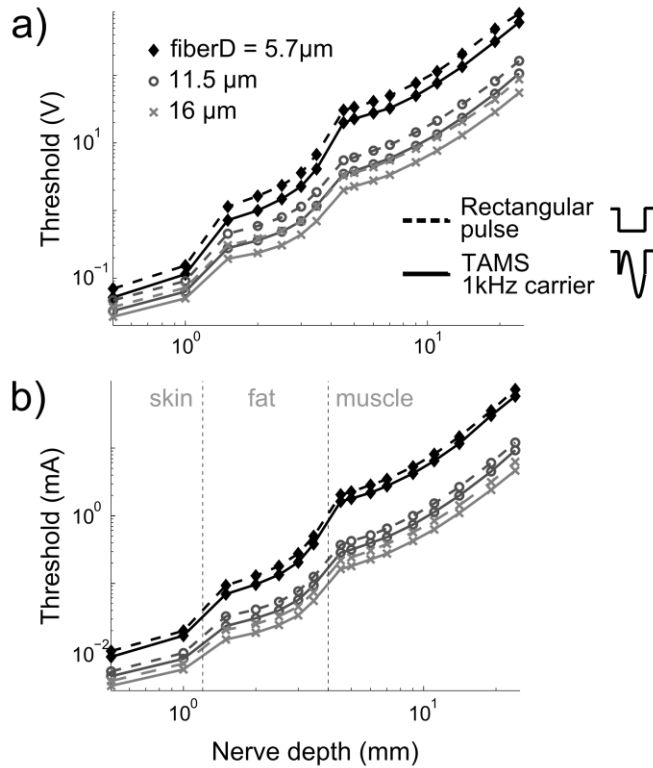


**Figure 2.4. Strength-distance relationship for the Transdermal Amplitude Modulated Signal (TAMS) and rectangular pulses.**

Thresholds for three fiber diameters (fiberD) as a function of distance from the skin surface to the nerve fiber when administering (a) voltage-regulated stimulation, and (b) current-regulated stimulation. Dotted vertical lines in (b) indicate the location of the interfaces between tissue layers. Skin thickness: 1.5 mm, fat thickness: 2.5 mm. Pulse width: 1 ms.

### 2.3.3 Filtering properties of the axonal membrane

We assessed the filtering properties of the axonal membrane and the possible influence on nerve activation by quantifying the attenuation of the transmembrane potential,  $V_m$ , as a function of the sinusoidal frequency. For these simulations, we configured our volume conductor model as a purely resistive medium by neglecting capacitive effects and setting the conductivity of each layer constant and equal to its value at frequency approaching zero (*i.e.*, no dispersion). For sinusoidal stimulation, the excursion of  $V_m$  strongly depended on frequency (Figure 2.5a), and the 200 kHz signal was almost entirely attenuated. If a dc component was added, then the 200

kHz carrier was again filtered out, and  $V_m$  resembled that generated by the rectangular pulse (Figure 2.5a). The ratio of the RMS of  $V_m$  to the maximum depolarization generated by a rectangular pulse was used to summarize this filtering effect (Figure 2.5b). The ratio decayed monotonically with frequency for all fiber diameters, indicating that the membrane acts as a low pass filter, and in the hundreds of kHz range the changes in  $V_m$  are nearly completely attenuated (*i.e.*, ratio approaches zero). However, if a nonzero offset is added, as in TAMS, the dc component contributes to fiber activation and the threshold rises more gradually with frequency than for stimulation with a zero offset sine wave (Figure 2.5c).

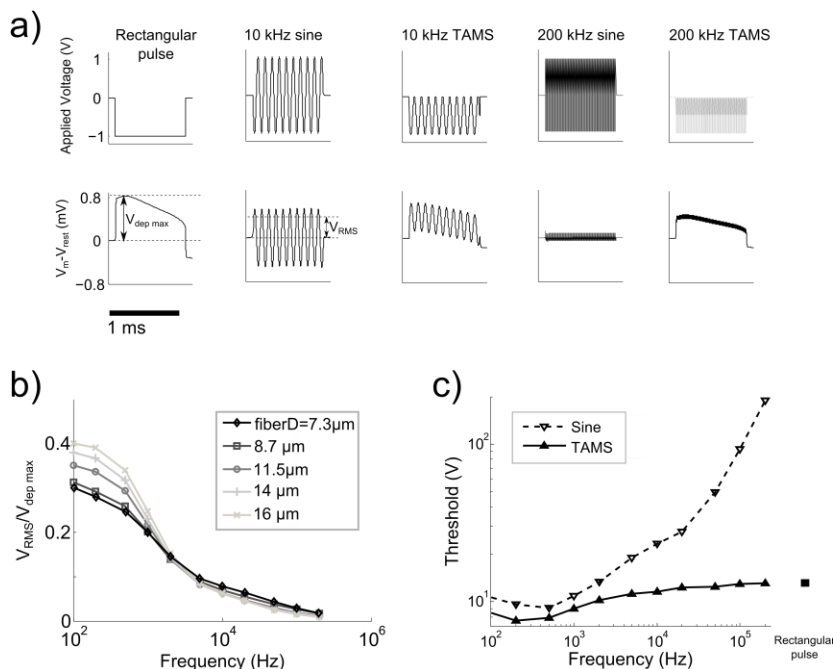


**Figure 2.5. Transmembrane voltage response to sinusoidal stimulation.**

(a) Time course of the reduced transmembrane potential,  $V_m - V_{rest}$ , at the central node of a 14  $\mu\text{m}$  fiber (*bottom row*) for five sub-threshold stimulation waveforms (*top row*) in a purely resistive medium. (b) Ratio of the root mean square (RMS) value of the reduced transmembrane potential ( $V_{RMS}$ , as depicted in (a), second panel from left) generated by sinusoidal stimulation with a fixed amplitude to the maximum depolarization generated by a sub-threshold rectangular pulse ( $V_{dep\ max}$ , as depicted in (a), leftmost panel). The ratio is plotted against frequency for five fiber diameters (fiberD). (c) Comparison of thresholds for zero offset sine waveforms, measured as the signal amplitude, and the Transdermal Amplitude Modulated Signal (TAMS), measured as the dc component. Electrode diameter: 2 cm. Fiber to electrode distance: 7 mm.

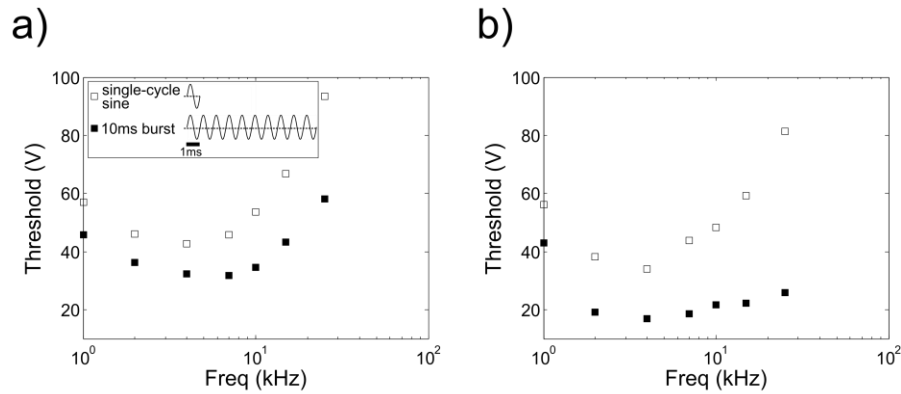


**Figure 2.6. Motor thresholds measured experimentally and estimated with model.**

(a) Motor thresholds reported by Ward and Robertson (2001). (b) Single action potential thresholds obtained with the model. Skin thickness: 1.5 mm. Fat thickness: 2.5 mm. Electrode: 40 x 44 mm.

### 2.3.4 Prediction of experimentally measured thresholds

We determined whether the model could predict motor thresholds obtained for TES with sinusoidal regulated voltage stimuli applied to the forearm with two carbon rubber electrodes [37]. Initially, across the 1 - 25 kHz frequency range tested by Ward and Robertson [37], our model showed monotonically increasing thresholds with frequency (Figure 2.5c). However, after introducing nonlinearity into the electrode-skin interface impedance (*i.e.*, frequency-dependent deviation factor, as described in Methods), the calculated threshold versus frequency curve showed a remarkably similar shape to that of the experimental motor thresholds (Figure 2.6). The model reproduced both the non-monotonic relationship of threshold with frequency, including a minimum around 5 kHz for the single-cycle waves, and lower thresholds for the 10 ms burst with respect to the single-cycle waves. However, the model did not capture the rate of increases in threshold with frequency for 10 ms bursts. This deviation may be due to differences in detection of single action potential thresholds in the model axon versus thresholds for torque generation measured experimentally, where temporal summation may influence detection of the threshold response.

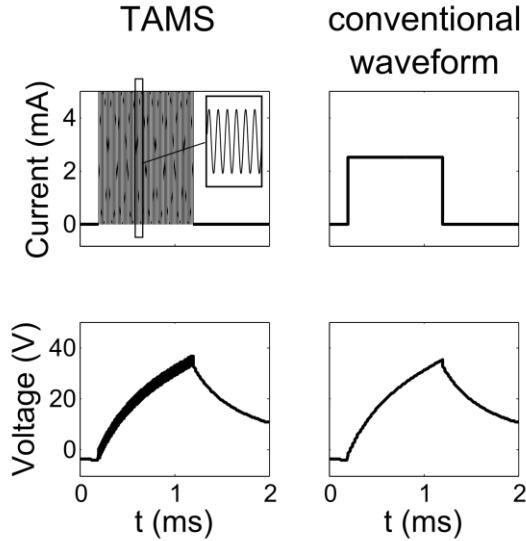


**Figure 2.7. Waveforms from the model of the Slovak *et al* (2013) experiment.**

Input current (*top*) and voltage across the electrodes (*bottom*) for the forearm model. Waveforms are shown for the Transdermal Amplitude Modulated Signal (TAMS) (*left*) and for conventional rectangular pulse (*right*). Skin thickness: 1.5 mm. Fat thickness: 2.5 mm. Electrode diameter: 2 cm. Inter-electrode distance (center to center): 3 cm.

Finally, we modeled TES of the forearm with TAMS as in [50]. They measured sensation and motor thresholds with both current-controlled TAMS and conventional pulses for TES over the ulnar nerve. Similar to their measurements, our model showed that the voltage on the skin surface was a low-pass filtered version of the applied current and looked quite similar for TAMS and a conventional pulse (Figure 2.7). Further, in agreement with[50], we observed little difference in the thresholds with TAMS and rectangular pulses (Table 2.1).

**Table 2.1. Thresholds obtained with the forearm model and motor thresholds reported by Slovak *et al* (2013).**

	Rectangular pulse	TAMS
<b>Model</b>	3.52 mA	3.38 mA
<b>Slovak <i>et al.</i> [50]</b>	$3.84 \pm 0.68$ mA	$3.81 \pm 0.77$ mA

## **2.4 Discussion**

The objective of this study was to quantify the effects of frequency in a model of transcutaneous electrical stimulation (TES). We focused on frequencies higher than those typically used in neural stimulation, *i.e.*, the kilohertz range. We developed a multilayer volume conductor model that included dispersive tissues and capacitive effects, and tested whether incorporating high-frequency components into the stimulation waveform could facilitate excitation of peripheral nerve fibers. We observed larger voltages at depth (*i.e.*, greater penetration) in the kHz range, but this did not translate into lower thresholds. The possible benefits of less attenuated extracellular potentials - and the spatial derivatives of the extracellular potentials - at deeper locations in the tissue, as a result of the tissue filtering properties, were offset by the filtering properties of the membrane, where higher frequencies produced smaller changes in transmembrane voltage. Further research is needed to determine the potential contributions of ion channel dynamics to the increases in threshold with frequency.

### **2.4.1 Filtering properties of biological tissue**

Our multilayer volume conductor model revealed that the frequency-dependent effects on penetration were greatest in the skin layer. The penetration in the skin increased dramatically above  $\sim 10$  kHz, whereas in the remaining layers there was a comparatively smaller decline in penetration with frequency (Figure 2.2). The conductivity of the skin increases by approximately three orders of magnitude from 1 to 100 kHz, while the conductivity of both fat and muscle show little variation in the same frequency range [118]. On the contrary, the permittivity of both fat and muscle, but not skin, decay strongly with frequency. Therefore, the deeper total penetration observed in the high frequency range ( $> 10$  kHz) is dependent on the dielectric properties of the skin, particularly the conductivity. This is consistent with the findings of [122], who showed that the potential in a homogenous, isotropic volume conductor was more strongly dependent on the

conductivity than the permittivity of the medium. Accordingly, removing the capacitive effects from our model did not substantially change the penetration profile of all three layers. Similarly, Grant and Lowery [124] found that, under certain conditions of deep brain stimulation, neglecting dispersion could generate large errors in the calculated potentials. This further emphasizes the need to incorporate dispersion, although in our model the main contributor for the variations in voltage with frequency was dispersive conductivity.

#### **2.4.2 Influence of the electrode-skin interface (ESI)**

The ESI has a strong influence on the relationship between threshold and frequency. Our model of the Ward and Robertson experiment initially showed strictly increasing thresholds over the 1 – 25 kHz range that they tested. However, after introducing nonlinearity to the deviation factor,  $\alpha$ , of the constant phase angle impedance, our model reproduced quite well the experimentally measured motor thresholds (Figure 2.6). Even though we were not able to find experimental studies assessing a direct dependency of  $\alpha$  on frequency, we varied it over the experimentally measured range for hydrogel skin electrodes [163]. In estimating the parameters of the constant phase angle impedance, McAdams *et al.* [163] assumed that  $\alpha$  was frequency-independent. Cantrell *et al.* [130] also assumed frequency-independent  $\alpha$ , but since  $\alpha$  shows a dependency on the electrode overpotential for large voltages, it can indirectly depend on frequency. Nonetheless, our frequency-dependent  $\alpha$  might reflect other nonlinear processes occurring at the ESI. For example, Wei and Grill [136] found that the impedance of deep brain stimulation electrodes could be well described by nonlinear circuit elements. Additionally, Dorgan and Reilly [168] introduced a nonlinear model of the skin impedance under neuromuscular stimulation. Thus, in the Ward and Robertson experiment, the ESI, the skin impedance, or both, might have included nonlinearities, which our model captured in the deviation factor of the ESI.

### **2.4.3 The transdermal amplitude modulated signal (TAMS)**

The TAMS waveform has been used for bladder control via transcutaneous stimulation of the pudendal nerve in cats [45, 46]. Activation of the pudendal nerve was verified by observing anal sphincter activity, and by comparing the results to similar studies employing direct stimulation of the pudendal nerve. The authors assumed that TAMS was “optimal for stimulating nerves under the skin and muscle” since the skin impedance is minimal at the frequency of the carrier (210 kHz). However, both TAMS and conventional stimuli might also activate both nerve fibers in the skin and in the underlying muscles as our analysis failed to reveal any inversion of the strength-distance curve that would allow stimulation of deep fibers at lower thresholds than more superficial fibers. It then follows that to excite a nerve located at a specific depth from the skin surface, both TAMS and conventional stimuli would activate the same population of more superficial fibers and thus would be at least equally effective. Further, we observed little difference in thresholds with TAMS and conventional pulses, in agreement with the experimental observations of [50].

### **2.4.4 Voltage versus current stimulation**

The use of either voltage- or current-controlled stimulation has a direct impact on the properties of nerve excitation since regulated current, but not regulated voltage, generates the same current flow through the tissue regardless of the impedance [169]. Thus, even though voltage-controlled stimulation is generally considered lower risk in transcutaneous electrical stimulation, it produces less predictable forces [170]. We simulated both types of stimulation and found that the filtering properties of the tissue substantially differed, as reflected in the opposite effects of frequency on  $\Delta^2\Phi$ , *i.e.*, high-pass and low-pass behavior for voltage- and current-controlled stimulation, respectively. For the geometries tested here, we found that fat thickness had little influence on threshold across all carrier frequencies of TAMS, regardless the type of

stimulation. This can be interpreted as an effect of the great dissipation of energy in the skin and at the electrode-skin interface, which may reduce the impact of fat thickness. This latter observation is confirmed by the strong effect of skin thickness on thresholds for voltage controlled stimulation. These results support the use of one or the other type of stimulation depending on the geometry of a particular application, *i.e.*, they favor voltage stimulation for thin skin, and current stimulation for more superficial nerves.

#### **2.4.5 Conduction block**

Although in our study we did not directly assess conduction block, we tested frequencies that have been used for this purpose, *i.e.*, from 600 Hz to 40 kHz (for a review see [30]). Block generally employs a continuous ac signal, and it is unclear whether pulses of ac, as used in this study, can produce conduction block. The initiation of the ac block signal produces an 'onset response' [79], *i.e.*, the initial fiber activation transiently triggered by the kHz-frequency block signal. It is possible that in our study we observed a similar phenomenon, in which the transient phase of the stimulation waveform was responsible for axon firing. However, we only used single pulses and therefore further investigation is needed to determine the properties of nerve excitation and block with modulated ac signals. The modeling study by Rattay [75] suggests that modulated ac can indeed produce synchronous activation under certain conditions, but it remains unclear whether similar results can be obtained with extracellular stimulation of more complex nerve fiber models. kHz-frequency continuous signals applied to the MRG model do indeed produce conduction block [32, 97], and in accordance with our results the onset response as described above was observed for both block and non-block signals. In addition, conduction block of superficial fibers and activation of deeper fibers may occur concomitantly with kHz frequency TES leading to less discomfort.

### 2.4.6 Model limitations

One of the limitations of our approach was not accounting for the more complex geometry of the tissues. For a particular application, a more detailed description of the geometry may be necessary to predict more accurately stimulation thresholds at different tissue depths and waveform frequencies. The Fourier-based solution presented here dramatically increases in complexity as the number of boundaries increases, particularly for non-planar shapes. In these cases, a numerical approach (*e.g.*, finite element method) is likely to be more appropriate. However, our approach was suitable to generate an understanding of the properties of high-frequency TES as a step preceding application-specific solutions. In addition, the truncation of the digitized Fourier transform can introduce artifacts in the spatiotemporal distribution of potentials. However, preliminary assessments showed variations in the potential  $\leq 5\%$  when the spatial resolution was changed from 1 mm to 0.5 mm.

Another limitation may arise from the use of a nerve fiber model that has not been thoroughly validated for kHz-frequency stimulation signals. Although we replicated the results of two prior experimental studies of high frequency stimulation, not all conductances present in human peripheral myelinated nerve fibers are included in the MRG model (*e.g.*, [103]). As well, Haydon *et al.* [126] found that membrane capacitance declines by a factor of two between dc and 100 kHz, and this may affect excitation thresholds in range of frequencies that we tested. Preliminary assessments showed that reducing the membrane specific capacitance from 2 to 1  $\mu\text{F}/\text{cm}^2$  caused thresholds for 100 kHz signals to vary by less than 10%. However, since stimulation waveforms may present broad frequency content, further research is required to assess the potential impact of a frequency-dependent formulation of the membrane capacitance in the nerve fiber model.

Finally, we focused on large diameter fibers within the muscle layer. In TES, comfort can be an important factor for patient acceptance, and thus modeling studies have addressed the activation of superficial nerve endings [127, 171]. Our model could be used to study cutaneous activation by placing unmyelinated fibers in the skin layer in different orientations, but multiple layers of cutaneous tissue, as in [158], may be necessary as they can have substantially different dielectric properties. Additionally, the number of action potentials generated in superficial versus deep fibers may help explain differences in comfort level with high frequency TES and conventional stimulation. In general, we observed single action potentials using just above threshold stimulation, but as the stimulus strength increased, multiple action potentials were elicited with long duration stimuli.

## **2.5 Conclusion**

We implemented a multilayer model of TES that accounted for dispersive tissues and capacitive effects, thereby providing a framework suitable for kHz frequency TES simulations. Our model suggests that high-frequency signals generate larger potentials at depth than low frequencies. However, incorporating kHz signals in the stimulation waveform does not necessarily facilitate fiber excitation. We quantified the effects of a novel signal, TAMS, and observed non-monotonic variation of threshold as a function of the carrier frequency. Additionally, both TAMS and conventional rectangular pulses activated more superficial fibers in addition to the deeper, target nerve fibers. Our results suggest that current regulated stimulation is more strongly influenced by fiber depth, while voltage regulated stimulation is more strongly influenced by skin thickness. Finally, our model reproduced the threshold-frequency relationship of experimentally measured motor thresholds.

## **Chapter 3: Phantom Model of Transcutaneous Electrical Stimulation**

### **3.1 Introduction**

Electrical stimulation of nerve fibers using high-frequency (HF) signals in the kilohertz range has gained increased attention in recent years due to the potential to penetrate deep in the tissue and to the ability to block fiber conduction. In particular, transcutaneous electrical stimulation (TES) may be optimized by overcoming the impedance of the skin, which declines by several orders of magnitude between hundreds of Hz to hundreds of kHz [23]. Thus, it may be possible to reach deeper structures by adding HF components to the stimulation waveform. Examples of TES applications employing HF signals are the interferential currents, in which the paths of two kHz currents cross and generate an amplitude modulated signal [24], and the transcutaneous amplitude modulated signal (TAMS), in which a high frequency (210 kHz) sinusoidal carrier is modulated by a traditional rectangular pulse [45].

In TES, an electrical field generated by a skin surface electrode is intended to stimulate nerve fibers in the underlying tissue. The excitation properties of nerve fibers by an extracellular field depend on the spatial and temporal characteristics of the field and the electrical properties and geometry of the fiber [113]. Thus, to understand better the effects of HF signals on nerve fiber excitation by TES, it is necessary to quantify the potentials in the tissue, which depends on the dielectric properties of the tissue and the electrode-tissue interface. Mathematical [36, 129, 139] and experimental models [141] have been proposed to quantify the potentials in the volume conductor using surface stimulation. We present a novel physical model to quantify the spatiotemporal distribution of potentials during TES using HF signals.

Phantoms are physical systems that emulate different properties of living tissue, and have been used in a variety of biomedical applications, including ultrasound imaging [172] and

electrical impedance tomography [142]. We developed a phantom model of TES that we used to quantify the potentials generated by HF signals *in vitro* as a function of the frequency of stimulation. We used both agar-based and biological materials in our phantoms, and added dispersion by doping the agar with graphite. We assembled up to three layers of materials and adjusted the composition of the gel to mimic the dielectric properties of living tissue. Additionally, the phantom model was used for *in vitro* experimental validation of a mathematical model of TES [36].

## **3.2 Methods**

### **3.2.1 Phantom Overview**

We used both agar-based and biological materials in our phantoms. Agar is a substance derived from polysaccharide agarose extracted from algae. Since agar provides a moldable solid structure from solution, it is a good candidate for measuring potentials in space using, for example, a penetrating microwire. Furthermore, the conductivity of the gel can be adjusted by varying the concentration of a conductive solute, *e.g.*, sodium chloride [146], and dispersion can be added by doping the gel with graphite [142, 145]. We first measured the dielectric properties of the materials, and then assembled up to three layers of material to create a volume conductor model of TES, in which we measured the potentials *in vitro*.

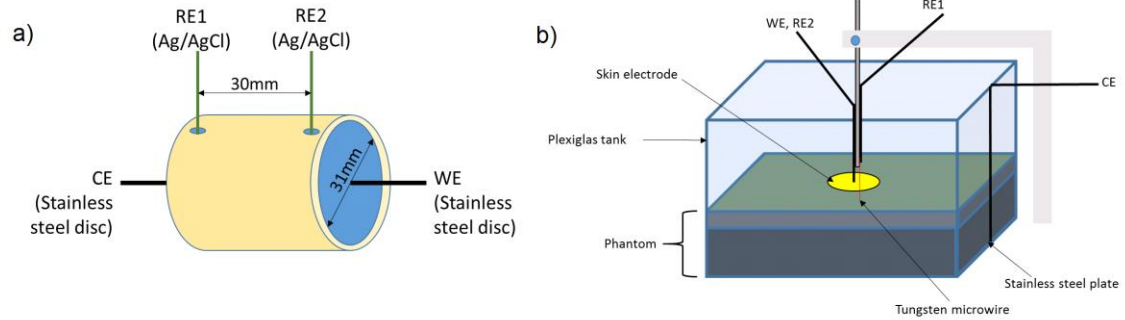


**Figure 3.1 Phantom model of transcutaneous electrical stimulation.**

a) Schematic diagram of the experimental setup to measure the dielectric properties of material samples. The electrodes are connected in a four-electrode configuration. b) Schematic diagram of the TES phantom. A Plexiglas tank contains the agar-based phantom on which electrical stimulation is applied with a skin electrode. The potentials are measured with a tungsten microwire. WE: working electrode. CE: counter electrode. RE1 and RE2: reference electrodes.

### 3.2.2 Agar-based Gel: Mixing Protocol

We prepared saline solutions by adding sodium chloride to deionized water at room temperature, with concentration ranging from 0.01% to 0.4% (w/w). We heated the solution to 50°C and added agar 4% (w/w) (Sigma-Aldrich) while continuously stirring. When the solution reached 85-90°C we removed it from heat and cooled it to 60°C. Then, we added graphite powder (Spectrum Chemical Corp., G1042) while vigorously stirring, as quickly as possible to minimize evaporative losses. We used graphite concentrations between 1% and 15% (w/w). Finally, we poured the solution into a mold (a test cell or a Plexiglas tank as described below) to cool to room temperature, and performed the measurements as soon as the solution solidified, typically after about 20 minutes.

### 3.2.3 Biological and Synthetic Materials

We prepared samples of banana and the skin of zucchini squash that we fitted snugly into a test cell to measure their dielectric properties with the four-electrode technique. These biological materials have been used previously as skin phantoms in electrical impedance tomography [142, 148]. We also measured the dielectric properties of a sheet of a 0.25 mm thick

polyethersulfone polymer [142] (Omega Ultrafiltration Membrane, Pall Corporation), using a thin layer approximation as described below. The material that most closely resembled the dielectric properties of the skin was used in the TES phantom.

### 3.2.4 Dielectric Properties of Materials

We measured the dielectric properties of the materials using the four-electrode technique (Figure 3.1a). A sample of agar-based gel or biological material was placed into a PVC cylindrical test cell of 36 mm length and 35 mm inner diameter. We covered both ends with stainless steel disks (32 mm diameter) that we used as working and counter electrode, respectively, to apply voltage-controlled sinusoidal stimulation. Through two small holes in the cell cylinder, separated by 30 mm, we introduced silver/silver chloride wires that served as the voltage measurement electrodes. This configuration bypasses the voltage drop at the working and counter electrode-material interfaces, thereby accurately measuring the voltage drop in the material. We conducted electrochemical impedance spectroscopy using an electrochemical interface (Model 1287, Solartron Analytical, Hampshire, UK) and frequency response analyzer (Model 1252, Solartron Analytical, Hampshire, UK). The frequency response analyzer applied a 100 mV sinusoidal voltage superposed with a 300 mV dc bias voltage, and the electrochemical interface measured the resulting voltage between the reference electrodes. The frequency of the applied sinusoidal voltage was varied between 1 Hz and 300 kHz. The measured impedance,  $Z$ , was then used to determine the conductivity,  $\sigma$ , and permittivity,  $\epsilon$ , using the formulae:

$$\sigma = \text{Re}\{Z\}/|Z|^2 * d/A, \quad \epsilon = \text{Im}\{Z\}/|Z|^2 * d/(2\pi f * \epsilon_0 * A) \quad (3.1)$$

where  $d$  is the distance between the reference electrodes,  $A$  is the cross-sectional area,  $f$  is the frequency and  $\epsilon_0$  is the permittivity of free space. To determine the electrical properties of the polymer sheet we used a thin-layer approximation described in [173]. For a thin material, we

assume that the problem can be reduced to 2D and that the current flows radially between the stimulation electrodes. Then, integrating the electric field over a line we obtain:

$$\Delta V = I \ln(2) / \pi \sigma t \quad (3.2)$$

where  $\Delta V$  is the measured voltage,  $I$  is the applied current and  $t$  is the sheet thickness. Four linearly aligned microwire electrodes were placed in contact with the polymer sheet and the current was applied between the outer pair of electrodes and the voltage measured between the inner pair of electrodes.

### 3.2.5 TES Phantom

We assembled up to three layers of material in a Plexiglas tank (128 x 128 x 100 mm), as shown in Figure 3.1b. At the bottom of the tank we placed a stainless steel plate (125 x 125 mm) that was used as the counter electrode. On the most superficial layer of the phantom we placed a 51 mm diameter surface electrode (Uni-Patch, Model 627SB) that served as the working and reference electrode. We made a small hole in the center of the surface electrode, through which we introduced a tungsten microwire that we used as a voltage measurement electrode. Since we used the surface electrode as reference, we measured the electrode-material interface impedance by placing the microwire on the surface of the phantom. The microwire penetrated perpendicularly to the surface, and the depth of the microwire tip was varied from 0 to 30 mm using a stereotactic frame. For each depth, we measured the impedance with the instrumentation described in Section 3.2.4, as a function of sinusoidal frequency from 1 Hz to 300 kHz. This procedure was repeated for two different phantoms: a single layer of agar-based gel (0.15% NaCl + 10% graphite), and a three-layer phantom composed of an agar-based gel (0.15% NaCl + 10% graphite), an agar-based gel with no doping, and zucchini skin.

### 3.2.6 Mathematical Model

We developed a mathematical model of a planar multilayer volume conductor, including dispersive media and a representation of the electrode-skin interface impedance [36]. We solved the Helmholtz equation for the potential by Fourier-transforming the  $x$  and  $z$  space variables into the spatial frequencies  $k_x$  and  $k_z$ , respectively. Thus the problem was reduced to a second order ordinary differential equation, with solution:

$$\varphi_{tissue}(y) = A_{tissue}\exp(k_y a y) + B_{tissue}\exp(-k_y a y) \quad (3.3)$$

where  $\varphi_{tissue}$  is the potential in the transformed domain,  $k_y^2 = k_x^2 + k_z^2$ , and the coefficients  $A_{tissue}$  and  $B_{tissue}$  are dependent on the boundary conditions. Next, for a given depth  $y$  we inverted the 2-D Fourier transform to obtain the potential phasor  $\Phi(\omega)$  in the entire volume.

The mathematical model representing each TES phantom was constructed using the respective conductivity and permittivity that we measured for each layer of the phantoms, and the electrode-skin interface impedance was modeled as the measured impedance at the surface of the phantom.

## 3.3 Results

The conductivity of the agar-based phantoms was approximately linearly dependent on the concentration of sodium chloride (Figure 3.2a), in agreement with previous reports [146]. In the frequency range that we used, the pure saline phantoms were non-dispersive, *i.e.*, the conductivity did not depend on frequency (Figure 3.2b, 0% graphite). However, the graphite-doped phantoms exhibited dispersion, which increased with the concentration of graphite. Thus, the conductivity of phantoms with 15% graphite almost doubled between 1 Hz and 100 kHz.

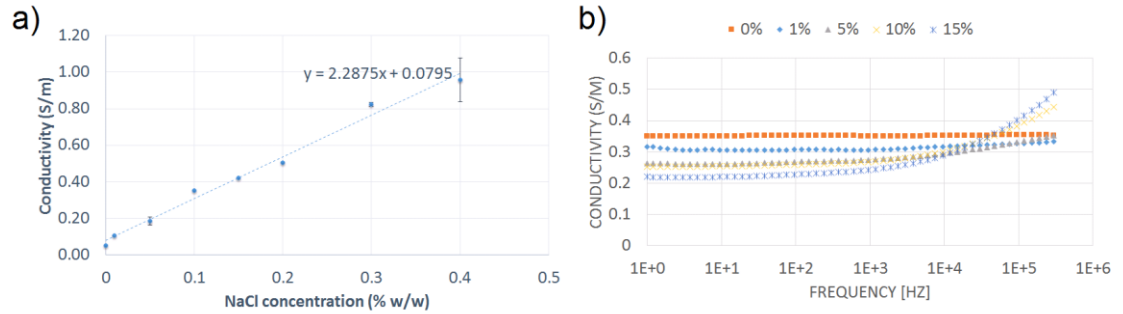


**Figure 3.2. Conductivity of phantoms.**

Conductivity of the agar-based phantoms as a function of a) sodium chloride concentration, and b) sinusoidal frequency for 5 different concentrations of graphite.

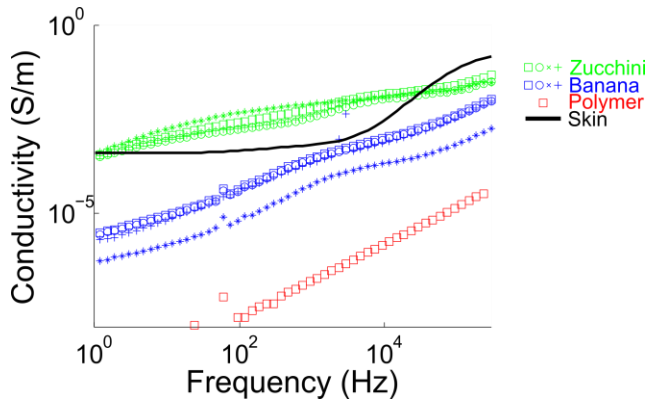


**Figure 3.3. Conductivity of skin and organic and synthetic materials used as skin phantoms.**

Green symbols: four samples of zucchini. Blue symbols: four samples of banana. Red squares: polyestherol polymer. Black line: skin, as measured by [118].

As shown in Figure 3.3, samples of zucchini and banana, and the polymer film, all exhibited dispersion. Our measurements were consistent across samples of the same fruit, except for one sample of banana that showed much lower conductivity. The conductivity of the banana and the polymer was smaller than  $1E-5$  S/m for low frequencies ( $<1$  kHz). On the contrary, in the same frequency range, the conductivity of zucchini was slightly higher than that of skin. The conductivity of zucchini showed the closest resemblance to that of skin, and therefore we used this material to represent the skin in our three-layer phantom.

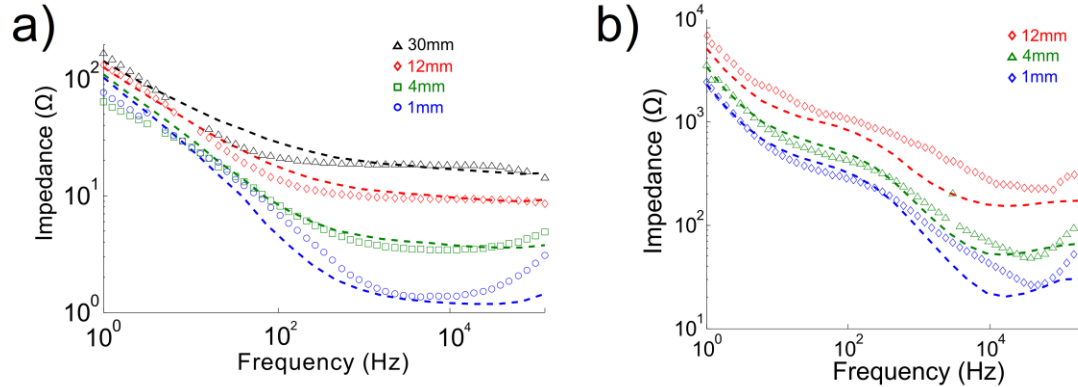


**Figure 3.4. In vitro measurements of impedance.**

Impedance as function of frequency at different depths for a) the single-layer and b) the three-layer TES phantoms. Symbols: experimental measurements. Dashed lines: mathematical model.

Figure 3.4 shows the measured impedance as a function of frequency at different depths, for both the single-layer and the three-layer TES phantoms. The impedance decayed strongly with frequency at all depths. Further, in both phantoms, the reduction of impedance with frequency was more accentuated at more superficial depths. In the single-layer phantom (Figure 3.4 a) the 10 kHz impedance at 1 mm decayed to 1% of its value at 1 Hz (from 77 to 1  $\Omega$ ), whereas at 30 mm it decayed to 11% (from 166 to 18  $\Omega$ ) in the same frequency range. In the three-layer phantom (Figure 3.4 b), the 10 kHz impedance decayed to 22% and 32% of the 1 Hz impedance at 1 and 12 mm, respectively. The three-layer phantom had two order of magnitude larger impedances due to the highly resistive zucchini layer in contact with the electrode. Also shown are the mathematical model solutions for each case (dashed lines in Figure 3.4), which showed good correspondence with the measurements of the single-layer phantom and three-layer phantom. Taken together, these results suggest that HF signals in TES may penetrate deeper in the tissue due to the reduced impedance at any depth.

### **3.4 Discussion**

We developed a phantom model of TES including dispersive materials. We used agar-based gels doped with graphite to create dispersion, and other biological and synthetic materials. We found that by adjusting the concentration of sodium chloride and graphite, it was possible to approximate the dielectric properties of muscle and fat. In addition, the dielectric properties of the zucchini squash were similar to those of the skin.

Previous phantom models of TES [141] used saline solutions, which lack observable dispersion in the kilohertz frequency range. Carbon-loaded phantoms have been used in electrical impedance tomography [142] and assessment of exposure to electromagnetic fields [145], in which the currents contain signals extending to the kilohertz and gigahertz range, respectively. To our knowledge, this is the first demonstration of a phantom model of TES using graphite to create dispersion, which makes it suitable for quantification of potentials as a function of frequency, and in particular in the kilohertz range.

One limitation of our study is that we made phantoms of simplified geometry. Our approach was to assemble materials with dielectric properties similar to those of muscle, fat and skin, respectively, and we used a cubic tank as a mold. We then quantified the impedance at depth and we neglected boundary effects. A more realistic phantom of TES for a particular application can be made with an appropriate mold, for example, of the human head [148, 174] or hand [145]. In addition, it is possible that inhomogeneities may have arisen by decantation of the graphite powder during the solidification of the agar. However, we used high concentration of agar (4% w/w) that quickly solidified (~20-30 min), thereby minimizing the migration of particles. Finally, we did not consider anisotropy, which is present in muscular tissue [118]. Anisotropy modifies the distribution of potentials and can affect nerve excitation [113], and therefore it can be a factor

in TES. Our model may be adapted to incorporate anisotropy by combining many slices of isotropic gel having different conductivities [147].

## **Chapter 4: Nerve Excitation Using an Amplitude-Modulated Signal with Kilohertz-Frequency Carrier and Non-Zero Offset**

### **4.1 Introduction**

Electrical stimulation of peripheral nerves is a treatment option for dysfunction of the lower urinary tract, chronic pain, epilepsy, and other neurological disorders [175]. In many cases, stimulation of peripheral nerves is delivered via an implanted device including an electrode in proximity to the nerve and a pulse generator. Transcutaneous electrical stimulation (TES) is a noninvasive alternative for peripheral nerve stimulation, in which an external electrode and stimulator deliver electrical currents across the skin, thereby reducing the risks and costs associated with implanted devices. Kilohertz frequency signals have been proposed as a means to overcome the high impedance of the skin, which declines several orders of magnitude as the frequency of stimulation extends to the kHz range, and thereby reach deeper structure from the skin surface [24]. For example, in interferential currents therapy, the paths of two kHz currents applied to the skin cross and generate an amplitude modulated signal intended to stimulate peripheral nerves [176]. Recently, a novel waveform called Transdermal Amplitude Modulated Signal (TAMS) composed of a 210 kHz carrier modulated by rectangular pulses, was proposed for bladder control [45] and to treat overactive bladder [47]. In TAMS, the sinusoidal carrier is added to a traditional rectangular pulse of half the amplitude of the carrier, resulting in a sinusoidal pulse (1 ms) with a non-zero mean (offset).

Preclinical studies of TAMS for bladder control via TES of the pudendal nerve in cats [45, 46] concluded that TAMS modulated bladder activity similarly to direct pudendal nerve stimulation. Both inhibitory and excitatory effects on bladder activity were evoked, depending on the frequency of the modulating waveform, *i.e.*, the rate at which the pulses were delivered,

consistent with prior reports on direct nerve stimulation [177]. Elkelini *et al.* [48] applied sacral nerve stimulation in spinally transected rats and found that TAMS reduced detrusor overactivity presumably by inhibiting C-fiber activity. Further, clinical studies showed that TAMS improved the symptoms and quality of life of overactive bladder patients [47, 49]. However, the mechanisms of action of TAMS, which may differ substantially from conventional low-frequency stimulation, remain largely unexplored. In particular, there is no direct comparison of the efficacy and efficiency of TAMS to conventional pulses, and the contribution of each component of the TAMS waveform to nerve excitation has not been determined. Moreover, both experimental and computational modelling results suggest that the high-frequency carrier used in TAMS may not affect nerve excitation. Slovak *et al.* [50] applied TES to the forearm of healthy subjects using conventional pulses and TAMS and recorded sensation thresholds and EMG responses. They found no differences in the measured outcomes if the offset of TAMS was equal to the amplitude of the conventional pulses. Medina and Grill [36] found that TAMS and conventional pulses produced the same thresholds for activation of model nerve fibers thresholds, even though the voltages in the volume conductor were less attenuated at depth for high-frequency carriers.

In the present study, we present a simple yet definitive experiment to quantify the effects of the carrier component of TAMS signal during direct nerve stimulation, *i.e.*, bypassing the filtering properties of the skin and underlying tissue. We conducted *in vivo* experiments in rats and cats to measure electromyogram (EMG) and compound action potential (CAP) responses evoked by sciatic nerve stimulation using conventional pulses, TAMS, and modified versions of TAMS with different amplitudes of the carrier relative to the pulse component of the waveform (Figure 4.1). Additionally, we implemented a computational model of nerve stimulation and quantified activation of model nerve fibers using the same stimulation waveforms. Thresholds were largely unaffected by the amplitude of the carrier if the carrier frequency was greater than

20 kHz, and it was the pulse component of the signal that generated nerve excitation. This quantitative assessment clarifies the contributions of the components of TAMS to nerve excitation and may be important for designing more efficient or effective stimulation waveforms.

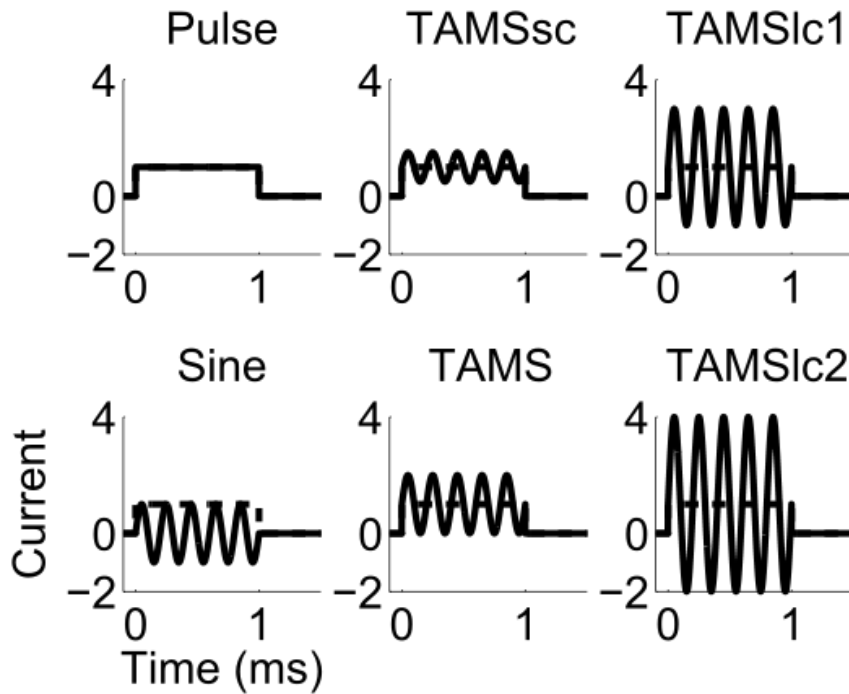


**Figure 4.1. Stimulation waveforms.**

The plots illustrate the rectangular pulse, the sinusoidal pulse, TAMS ( $\alpha=1$ ) and the modified TAMS ( $\alpha=0.5, 2,$  and  $3$ ). All waveforms have an offset ( $K$ ) equal to 1 (dashed lines) and a pulse width of 1 ms, except for the sinusoidal pulse that has zero offset and amplitude 1.

## 4.2 Methods

### 4.2.1 Stimulation waveforms

We quantified nerve excitation with five different stimulation waveforms: rectangular pulse, TAMS, and three modified versions of TAMS that differed in the amplitude of the carrier relative to the pulse component of the waveform (Figure 4.1). In addition to these five waveforms, in the computational simulations we also used a sinusoidal pulse of zero offset. Let

$s(t)$  denote the stimulation waveform and  $f_c$  denote the frequency of the carrier. TAMS and the modified versions of TAMS can be written as:

$$s(t) = K(1 + \alpha \sin(2\pi f_c t)) \quad 0 \leq t \leq PW \quad (4.1)$$

the rectangular pulse:

$$s(t) = K \quad 0 \leq t \leq PW \quad (4.2)$$

and the sinusoidal pulse:

$$s(t) = A \sin(2\pi f_c t) \quad 0 \leq t \leq PW \quad (4.3)$$

where  $PW$  is the pulse width,  $K$  is the signal offset,  $\alpha$  is the amplitude of the carrier, and  $A$  is the amplitude of the sinusoidal pulse. For TAMS  $\alpha=1$ , and we also used  $\alpha=0.5$ ,  $\alpha=2$  and  $\alpha=3$ , termed TAMSsc, TAMS1c1 and TAMS1c2, respectively. We note that in TAMSsc the carrier amplitude is smaller than in TAMS, whereas in the other two modified versions the carrier amplitude is larger than in TAMS. In all experiments, we used  $PW=1$  ms, and  $K$  was varied to construct the input-output curves as nerve excitation as a function of stimulation amplitude.

## 4.2.2 Computational model

We simulated extracellular stimulation of myelinated axons using the McIntyre-Richardson-Grill (MRG) cable model of a mammalian nerve fiber [86]. All axons had a diameter of 11.5  $\mu\text{m}$ , representing the largest motor fibers found in the rat sciatic nerve [55]. We calculated the extracellular potentials generated by two point source electrodes of opposite polarity separated by 2 mm in an infinite anisotropic medium of conductivities 1/3 and 1/12 S/m. We placed 100 axons containing 25 nodes of Ranvier within and parallel to a 1 mm radius cylinder, with the electrodes placed along the edge of the cylinder. The radial and azimuthal coordinates of

the axons axes were drawn from a uniform distribution, and the middle node was randomly positioned with respect to the cathode, but no further than half the internodal length. We applied the potentials to all compartments of the fiber models using the extracellular mechanism in NEURON v7.3, and we neglected axon-to-axon (*i.e.*, ephaptic) interactions. In all simulations, we used a simulation time of 3 ms and a time step of 1  $\mu$ s, *i.e.*, the sampling frequency was ten times the maximum frequency of the applied waveforms to avoid aliasing. We recorded the transmembrane potential at one end of the model axons to detect whether an action potential was elicited.

We constructed input-output (recruitment) curves using conventional pulses, sinusoidal pulses of zero mean, TAMS and modified TAMS, by increasing  $K$  ( $A$  for the sinusoidal pulse) using a step of 5  $\mu$ A until all model nerve fibers were activated. For the sinusoidal pulse, TAMS and modified TAMS we used 7 different (carrier) frequencies: 1, 2, 5, 10, 20, 50 and 100 kHz. We defined  $I_{50}$  as the  $K$  ( $A$  for the sinusoidal pulse) that activated half of the population, and the means and standard errors of these values across 8 different randomized populations of model nerve fibers were calculated.

### **4.2.3 In vivo experiments**

All animal care and experimental procedures were approved by the Institutional Animal Care and Use Committees of Duke University. Experiments were performed on adult rats ( $n=5$ ) and cats ( $n=3$ ), and the procedures for all animals were acute and terminal. Rats were sedated by inhalation of isoflurane, and then anesthetized with urethane (1.2 g/kg, S.Q.), with supplemental doses (0.4 g/kg, S.Q.) given as required. Animal body temperature was regulated with the use of a thermostatically controlled water-circulated blanket. The sciatic nerve was exposed by dissection of the skin from the heel to the vertebral column and reflection of the biceps femoris muscle. A bipolar hook electrode was placed on the sciatic nerve near the sciatic notch to deliver

stimulation. Electromyograms (EMG) from the medial gastrocnemius muscle were recorded using a pair of insulated fine stainless steel wires with exposed tips inserted percutaneously into the gastrocnemius musculature (Figure 4.2).

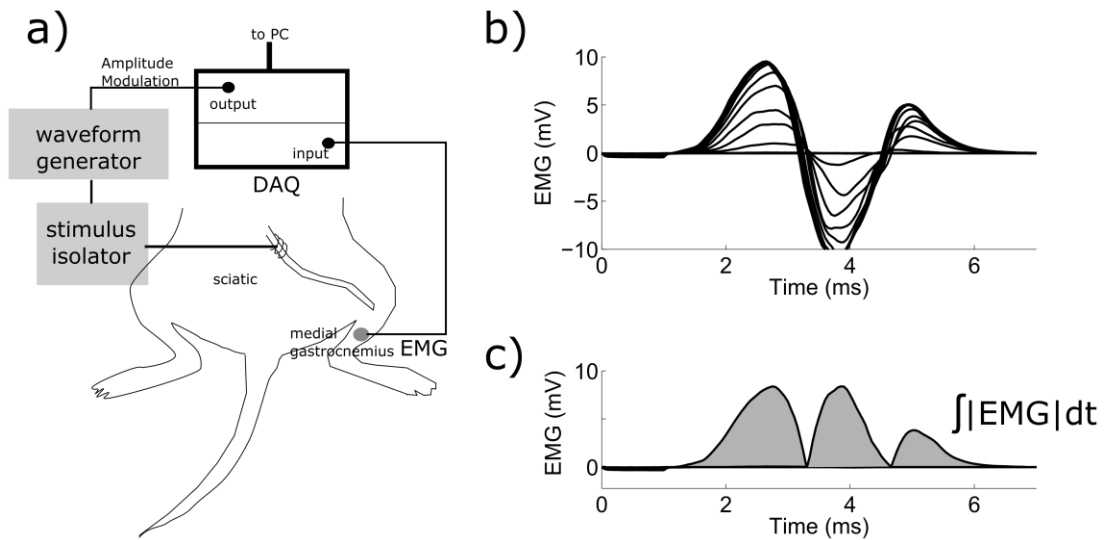


**Figure 4.2. In vivo stimulation of rat sciatic nerve.**

Stimulation was delivered through a pair of hook electrodes using a waveform generator controlled by computer (a). The evoked EMG signal was recorded from the medial gastrocnemius. In (b) the plot shows the evoked EMG activity using pulses of amplitudes 10 – 200  $\mu$ A. The signal was then rectified and integrated (c) to construct input-output curves.

Cats were sedated with acepromazine (0.3 mg/kg, S.Q.), and anesthesia was induced with ketamine HCl (15-35 mg/kg, I.M.) and maintained with alpha-chloralose (65 mg/kg I.V., supplemented at 15 mg/kg). Animals were intubated by tracheotomy and respired to maintain end tidal  $CO_2$  at 3-4%. Body temperature was maintained with a water circulating heating pad, and arterial blood pressure was monitored using a catheter in the carotid artery. Fluids levels were maintained by administering 0.9% saline with 8.4 mg/ml sodium bicarbonate and 5% dextrose (15 ml/kg/hr, I.V.). The sciatic nerve was exposed via an incision on the dorsal aspect of the thigh, and a bipolar hook electrode was placed on the nerve for stimulation. The tibial nerve was exposed via an incision medial to the distal portion of the calcaneal tendon, and a tripolar nerve

cuff electrode (2 mm I.D.; 5 mm intercontact distance) was installed around the tibial nerve to record the compound action potential (CAP). Similar to the rat experiments, the EMG of the medial gastrocnemius muscle was recorded using a pair of stainless steel wires with exposed tips inserted percutaneously.

Stimulation was delivered through the hook electrodes using an arbitrary waveform generator (Agilent 33120A) and a linear voltage-to-current converter (A-M Systems 2200). The EMG and CAP signals were amplified (100-1,000 and 1,000-10,000, for EMG and CAP, respectively) and filtered (3 Hz – 10 kHz) using a low noise voltage amplifier (Grass Technologies P511 AC Amplifier), and recorded using the Powerlab hardware system and the LabChart software suite (ADInstruments Inc) with a sampling rate of 20 kHz.

Input-output curves of the rectified and integrated evoked EMG and CAP signals as a function of  $K$  were measured for conventional pulses, and for TAMS and the three modified versions of TAMS using 7 carrier frequencies: 1, 2, 5, 10, 20, 50 and 100 kHz. The input-output curve was recorded by delivering pulses at 1 Hz and gradually increasing  $K$  in steps of 10-40  $\mu$ A every 6-10 pulses until maximal contraction was evoked. In each experiment, the input-output curve for the conventional pulse was recorded first, followed by the remaining 4 waveforms, and the order of presentation of the 7 carrier frequencies was randomized.

#### **4.2.4 Statistical analysis**

We log-transformed the data and analyzed the effects of carrier frequency and carrier amplitude ( $\alpha$ ) on  $I_{50}$ , which we defined as the  $K$  that produced 50% of the maximum area of the rectified EMG or CAP response. We performed a separate ANOVA for the EMG and CAP data with  $I_{50}$  as the dependent variable and waveform type, carrier frequency (nested within waveform type), and species (in the case of EMG data) as the independent variables. The ANOVA for the EMG data revealed that species had no significant interactions with the other independent

variables ( $p > 0.9$  in both cases), and EMG data from both species were combined for further analysis. For tests that revealed significant differences among waveforms, post hoc paired comparisons were performed using Fisher's protected least significant difference (FPLSD) test at a significance level of  $p < 0.05$ . Although data were log-transformed for analysis, data were plotted in the figures as average percent difference with respect to the pulse.

## **4.3 Results**

### **4.3.1 Simulations in a computational model of peripheral nerve fiber stimulation**

As the offset,  $K$ , (the amplitude,  $A$ , for the sinusoidal pulse) of the stimulation waveform was increased, the number of activated model nerve fibers increased monotonically for all stimulation waveforms (Figure 4.3a). The carrier frequency of TAMS and modified TAMS, as well as the frequency of the sinusoidal pulse, clearly affected the recruitment curves, and as the (carrier) frequency was decreased, the recruitment curve shifted to the left. We quantified the effect of the (carrier) frequency using  $I_{50}$ , *i.e.*, the signal offset (or amplitude) that activated 50% of the population. Figure 4.3b shows the difference in  $I_{50}$  between the sinusoidal pulse, TAMS and modified TAMS, and the rectangular pulse. All four TAMS versions had lower  $I_{50}$  compared to the pulse for all 7 carrier frequencies, and this difference increased for lower carrier frequencies. Further, for any given carrier frequency,  $I_{50}$  decreased more markedly as the size of the carrier increased, *i.e.*, the largest difference with respect to the pulse was obtained for TAMS1c2, followed by TAMS1c1, TAMS and TAMSsc. On the contrary, the zero-offset sinusoid had much higher  $I_{50}$  than the rectangular pulse for all frequencies.

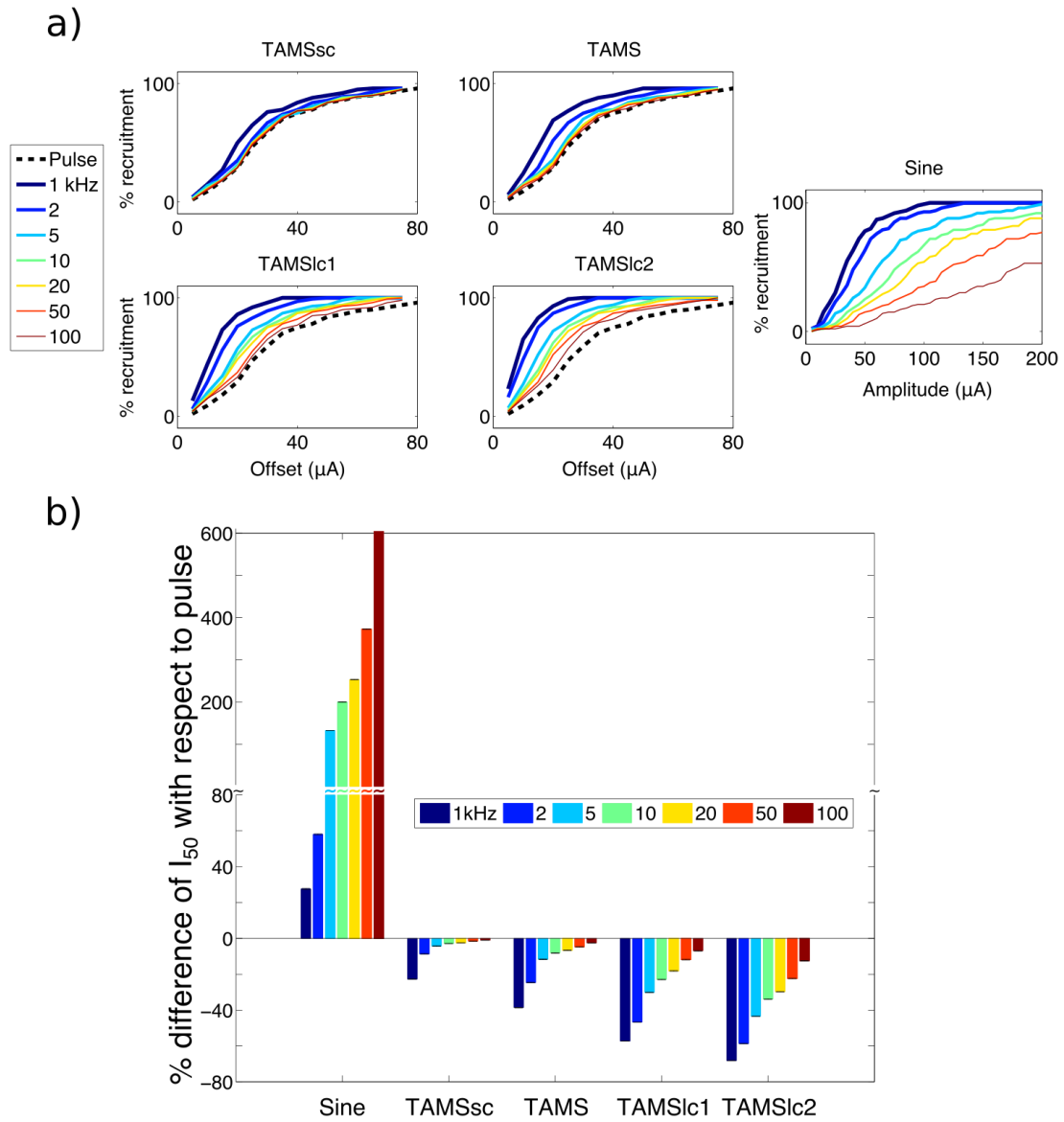
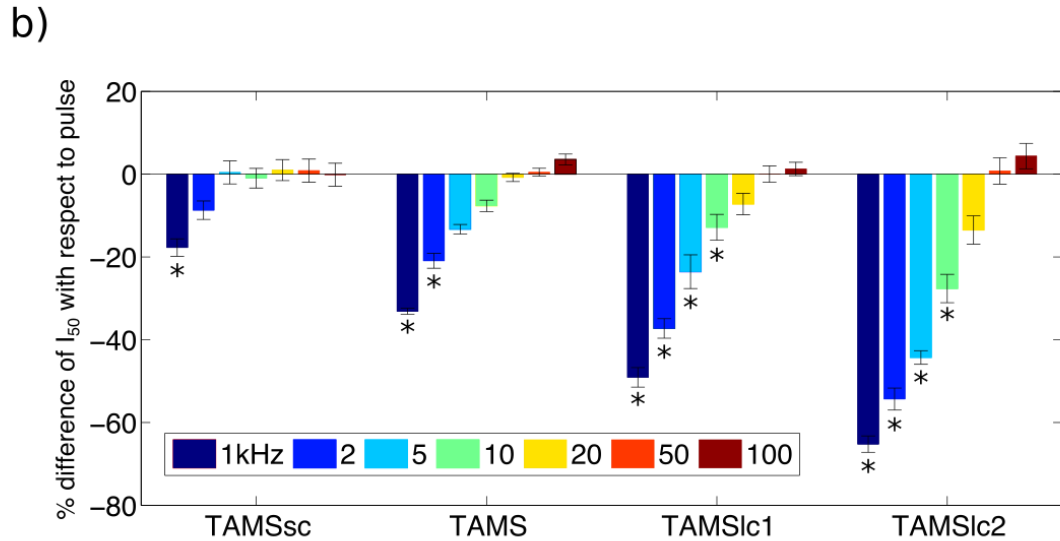
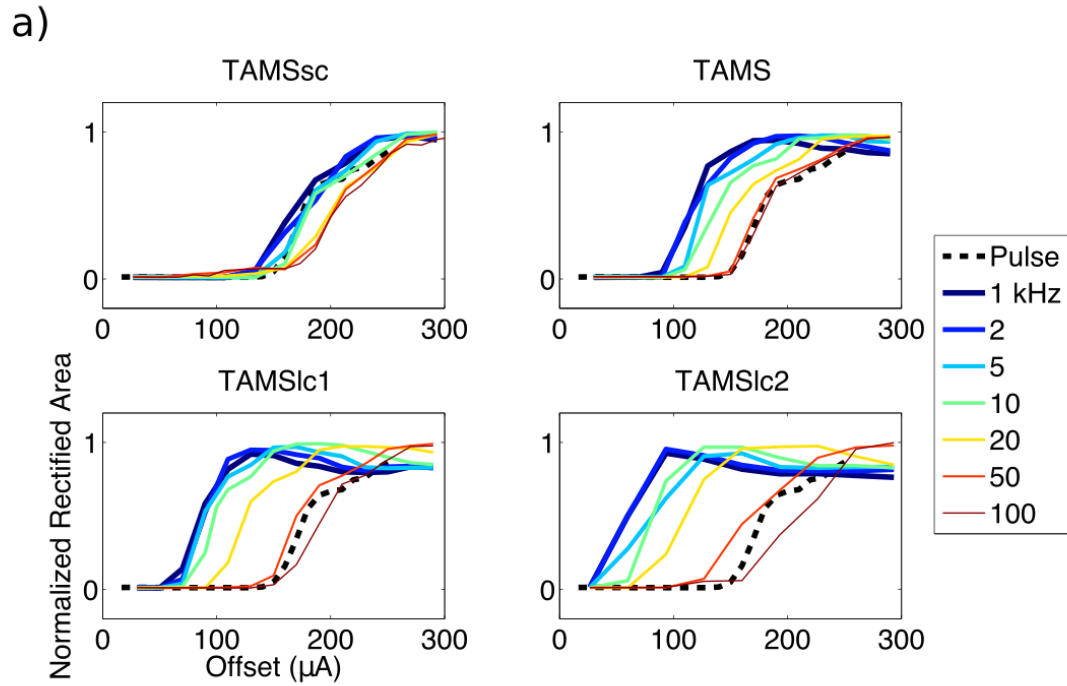


**Figure 4.3. Simulation of nerve stimulation.**

a) Recruitment curves for one sample population for all stimulation waveforms as a function of signal offset or signal amplitude. Each plot shows a different waveform using 7 (carrier) frequencies, except for the recruitment curve for the pulse, which was plotted in the TAMS graphs for comparison. b) Percent difference of  $I_{50}$  with respect to pulse for sinusoidal pulse, TAMS and modified TAMS using 7 (carrier) frequencies. Bars represent the average across 8 different axon populations. Error bars: SE.

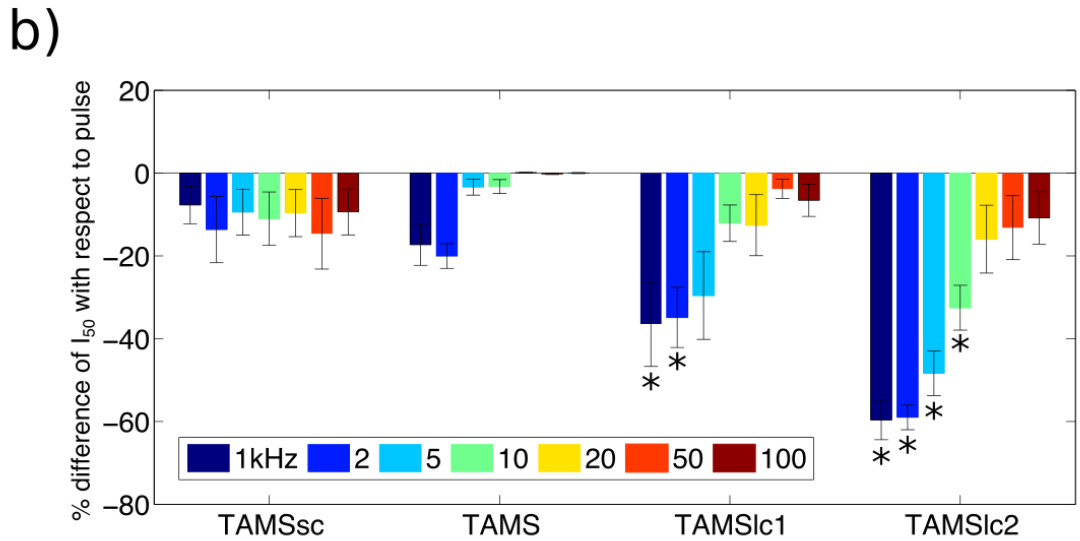
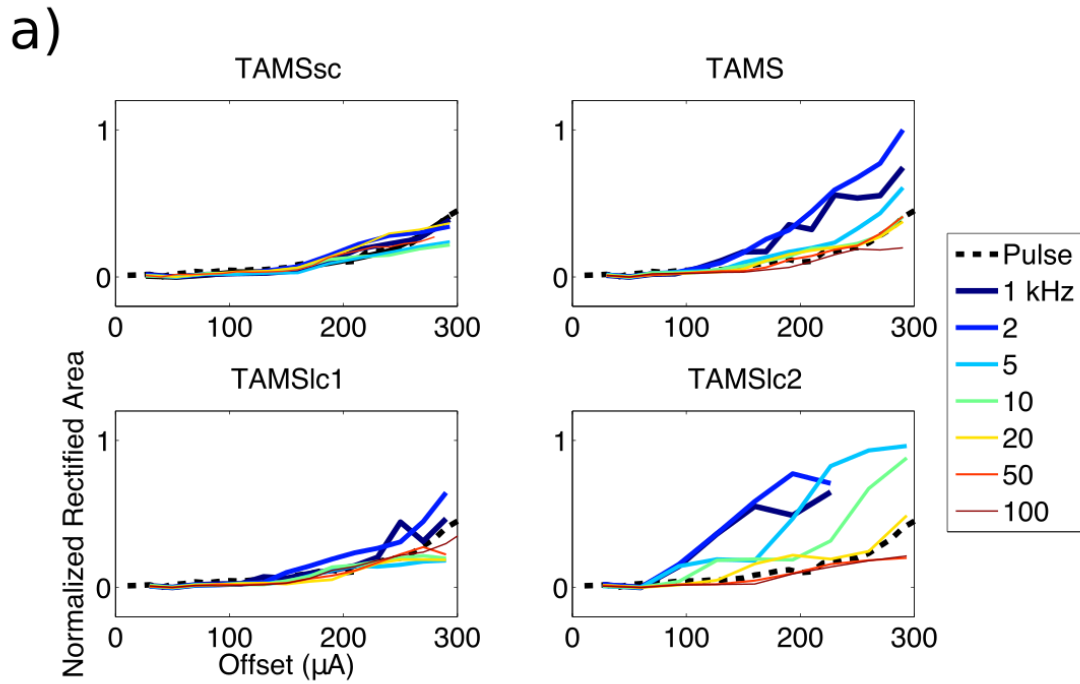
### 4.3.2 In vivo measurements

Figure 4.4 and Figure 4.5 show the effects of waveforms on the *in vivo* EMGs and CAPs, respectively. The rectified EMG area increased as  $K$  was increased, and the input-output curves, which exhibited sigmoidal shapes, shifted to the left as the carrier frequency decreased (Figure 4.4a).  $I_{50}$ , *i.e.*, the  $K$  that produced 50% of the maximal rectified area depended on the carrier frequency. For the 1 kHz carrier,  $I_{50}$  averaged  $142 \pm 23.5 \mu\text{A}$ ,  $114 \pm 18.8 \mu\text{A}$ ,  $94 \pm 24.5 \mu\text{A}$  and  $60 \pm 11.5 \mu\text{A}$  (mean  $\pm$  S.E.) for TAMSSc, TAMS, TAMSlc1 and TAMSlc2, respectively, and for the 100 kHz carrier,  $I_{50}$  averaged  $173 \pm 29.0 \mu\text{A}$ ,  $175 \pm 27.4 \mu\text{A}$ ,  $177 \pm 29.8 \mu\text{A}$  and  $188 \pm 38.2 \mu\text{A}$  (mean  $\pm$  S.E.), respectively. For the rectangular pulse,  $I_{50}$  averaged  $168 \pm 23.0 \mu\text{A}$  (mean  $\pm$  S.E.). A two-way repeated measures ANOVA showed significant effects of waveform type and frequency ( $p < 0.0001$  in both cases). *Post hoc* paired comparisons revealed significant differences (FPLSD,  $p < 0.05$ ) between rectangular pulse, and TAMS and modified TAMS only for certain carrier frequencies (Figure 4.4b). All four TAMS waveforms had significantly lower  $I_{50}$  compared to the rectangular pulse using the 1 kHz carrier, but none showed significant differences with the pulse for carrier frequencies higher than 10 kHz. Further confirmation of nerve responses as quantified by EMG was obtained with the CAP measurements, which showed similar trends. For the rectified area of the CAP, the input-out curves shifted to the left with frequency as well. For the 1 kHz carrier,  $I_{50}$  averaged  $265 \pm 56.6 \mu\text{A}$ ,  $225 \pm 13.5 \mu\text{A}$ ,  $187 \pm 65.2 \mu\text{A}$  and  $120 \pm 35.7 \mu\text{A}$  (mean  $\pm$  S.E.) for TAMSSc, TAMS, TAMSlc1 and TAMSlc2, respectively. For the 100 kHz carrier,  $I_{50}$  averaged  $262 \pm 60.0 \mu\text{A}$ ,  $281 \pm 41.3 \mu\text{A}$ ,  $268 \pm 54.4 \mu\text{A}$ ,  $259 \pm 62.8 \mu\text{A}$  (mean  $\pm$  S.E.), respectively. For the rectangular pulse,  $I_{50}$  averaged  $281 \pm 41.0 \mu\text{A}$ . In this case,  $I_{50}$  for only TAMSlc1 of 1 and 2 kHz, and TAMSlc2 of 1, 2, 5 and 10 kHz, was significantly lower than rectangular pulse (FPLSD,  $p < 0.05$ ).



**Figure 4.4. Evoked EMG activity.**

a) Input-output curves measured in one animal for all stimulation waveforms. Each plot shows a different waveform using 7 carrier frequencies, except for the pulse, which was plotted in all 4 graphs. b) Percent difference of  $I_{50}$  with respect to pulse for TAMS and modified TAMS using 7 carrier frequencies (mean  $\pm$  SE,  $n=8$ , \*  $p<0.05$  difference with pulse).



**Figure 4.5. Evoked CAP activity.**

a) Input-output curves measured in one animal for all stimulation waveforms. Each plot shows a different waveform using 7 carrier frequencies, except for the pulse, which was plotted in all 4 graphs. b) Percent difference of  $I_{50}$  with respect to pulse for TAMS and modified TAMS for 7 carrier frequencies (mean  $\pm$  SE,  $n=3$ , \*  $p<0.05$  difference with pulse).

## 4.4 Discussion

We quantified the contributions of the carrier frequency and amplitude of TAMS to nerve fiber activation *in vivo* and using a computational model. Carrier frequencies of 20 kHz and higher (recall that the default carrier frequency of the original TAMS waveform was 210 kHz) did not contribute to excitation (*i.e.*, activation was equivalent to the conventional pulse) regardless of the amplitude of the carrier, while lower carrier frequencies did contribute to excitation, as reflected by the substantial reductions in  $I_{50}$  relative to the conventional pulse without a carrier. Our simulation results closely matched our experimental measurements, and in the model using a carrier frequency of 1 kHz,  $I_{50}$  declined by 68%, 57%, 39% and 23% with respect to the pulse, for TAMS1c2, TAMS1c1, TAMS and TAMSsc waveforms, respectively, while for the EMG measurements, the reductions were 65%, 49%, 33% and 18%. Further, the model revealed much higher thresholds for the zero offset sinusoid as compared to the rectangular pulse, which supports the conclusion that high frequency signals of zero offset contribute little to nerve fiber excitation. Collectively, these results indicate that amplitude modulated kHz stimulation ( $> 20$  kHz) does not improve the efficacy or efficiency of electrical stimulation of peripheral nerves.

### 4.4.1 Mechanisms of nerve fiber activation using TAMS

TAMS with carrier frequencies below 20 kHz had lower thresholds than conventional pulses. Specifically, for 1 kHz TAMS the reduction in  $I_{50}$  was 33% and 17% for EMG and CAP, respectively. At this frequency, the 1 ms pulse comprises a single cycle of the carrier, and therefore the stimulation waveform may effectively act as a 500  $\mu$ s pulse of amplitude twice the offset. In this case, the strength-duration (SD) relationship, which quantifies nerve fiber threshold as a function of pulse duration, can be used to predict the differences in threshold. The SD curve is commonly described using the equation  $I_{th} = I_{rh}(1 + T_{ch}/PW)$ , where  $PW$  is the pulse width,  $I_{rh}$  is

the rheobase, *i.e.*, threshold current for a very long PW, and  $T_{ch}$  is the chronaxie, *i.e.*, PW to obtain a threshold of twice the rheobase [178]. The motor axons in the cat tibial nerve have a chronaxie of 0.53 ms [179]. It follows that if we consider the 1 kHz TAMS as a 0.5 ms pulse of double amplitude of the pulse, then the SD curve estimates a threshold for 1 kHz TAMS 33% smaller than the conventional pulse, and this matches quite well our measurements of  $I_{50}$ .

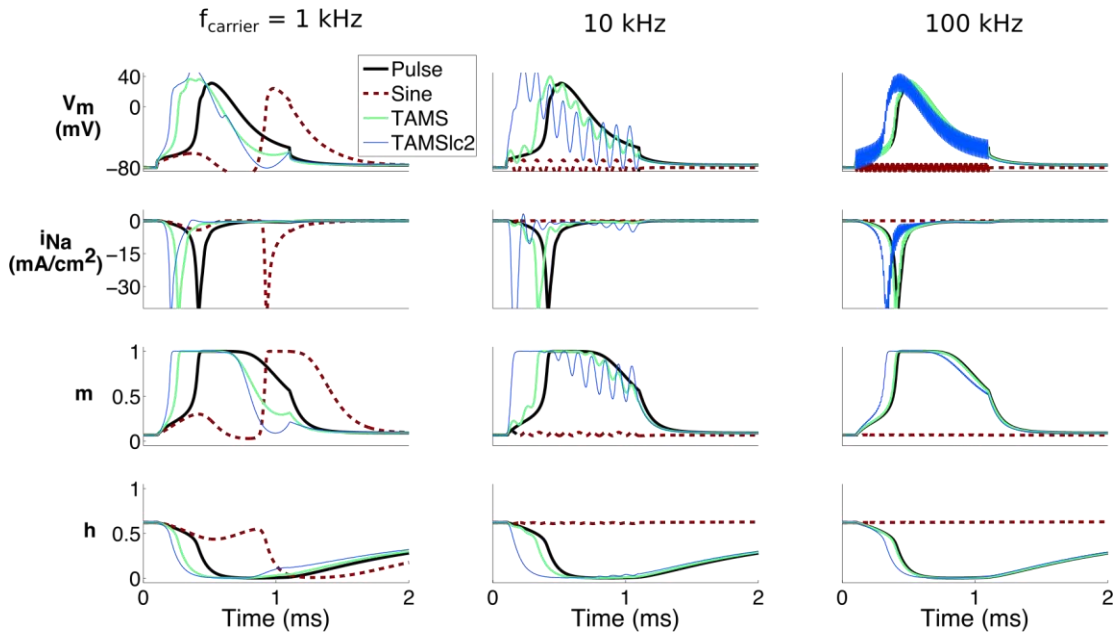


**Figure 4.6. Membrane parameters during stimulation with pulse, sine, TAMS and TAMS1c2.**

Each column represents a different (carrier) frequency, except for the pulse. The offset of the pulse, TAMS and TAMS1c2 was  $70 \mu\text{A}$ , and the amplitude of the sine was  $70 \mu\text{A}$ . The axon triggered an action potential in all cases, except for the 10 kHz and the 100 kHz sine. The pulse duration was 1 ms in all cases.

To understand the mechanisms of nerve fiber activation using TAMS with carrier frequencies greater than 20 kHz, we recorded membrane parameters (membrane voltage, sodium current, and sodium conductance gating parameters) in the model nerve fiber during stimulation with TAMS, the conventional pulse, and sine waves of 1 ms duration. During extracellular stimulation using rectangular pulses, the time course of the gating parameters may differ depending on the amplitude and duration of the pulse, and at threshold, the action potential

initiates near the end of the pulse [167]. As shown in Figure 4.6, the time course of the gating parameters and the sodium current for 100 kHz TAMS and the pulse overlapped, as it would be the case for two rectangular pulses of the same duration and well above threshold. Increasing the relative amplitude of the carrier, *i.e.*, TAMS1c2, only slightly altered the dynamics of the gating parameters, and the initiation of the action potential was shifted very slightly earlier in time. The membrane voltage showed only small oscillations at 100 kHz for the waveforms incorporating this frequency, and the zero-offset 100 kHz sine did not activate the axon. Therefore, the filtering of the membrane that passed the offset but attenuated the 100 kHz carrier, resulted in similar dynamics of the gating parameters, which explains fiber excitation in this frequency range. On the other hand, for the 1 kHz carrier the dynamics of the gating parameters differed greatly. In this case, for a 1 ms duration, TAMS and the sinusoidal pulse comprised only a single cycle of the sine wave. Further, TAMS roughly resembled a 500  $\mu$ s monophasic pulse, and the sinusoidal pulse, a biphasic pulse of 500  $\mu$ s each phase. As a result, the action potential initiated at slightly different times for TAMS and TAMS1c2, and somewhat later for the rectangular pulse, whereas for the sinusoidal pulse axon activation occurred by the end of the hyperpolarizing phase.

Continuous zero mean ac signals in the 1 kHz to 50 kHz range have been used for conduction block (for a review see [33]), but it is unclear whether amplitude modulated stimulation, as used in this study, can produce block. The onset of the kHz frequency block signal generates transient initial axon activation [33], and it is possible that in our experiments we observed a similar phenomenon, in which the transient phase of the stimulation waveform activated the axons. In their computational study, Bhadra *et al.* [32] simulated the onset phenomenon and observed distinct firing frequency responses to increasing signal amplitudes, from few action potentials to continuous firing, for both block and non-block signals. In our simulations, we observed only single action potentials for a wide range of amplitudes limited to

the 1 ms duration of the pulses, and this range, *i.e.*, up to few hundreds of  $\mu\text{A}$ , roughly matches the non-block amplitude range of Bhadra *et al.* using similar simulation conditions.

#### **4.4.2 Implications for transcutaneous electrical stimulation**

TAMS was originally proposed for transcutaneous electrical stimulation and was intended to generate less attenuated voltages at deeper nerves. The idea was inspired by the experimental observation that the impedance of the skin declines by several orders of magnitude as the frequency increases to the kHz range [23]. Thus, by incorporating high-frequency components into the stimulation signal, as in TAMS, it may be possible to overcome the impedance of the skin and underlying tissue to activate more deeply positioned nerves. While indeed our previous work demonstrated less attenuation at depth of high frequency signals [36], the present findings indicate that high frequency components of the TAMS signal do not contribute to activation of nerve fibers, which mitigates the possible benefit of deeper penetration. In our experiments, we bypassed the filtering effects of the skin by applying stimulation directly to the sciatic nerve, and manipulated the amplitude of the carrier. By means of this manipulation, we mimicked a scenario in which the filtering by the skin (and other intervening tissue) attenuates the (dc) offset much more so than the kHz frequency carrier, which we amplified as much as three times the size of the offset (*i.e.*, TAMS1c2). Since we observed no contribution of carriers of 20 kHz and above to nerve fiber activation, any reduction of carrier attenuation in TES will not affect nerve fiber excitation, as well.

Our results are in agreement with those of Slovak *et al.* [50] who found no differences in either motor thresholds or sensation thresholds between TAMS and conventional pulses. In their experiment, the authors applied current-controlled TES to the forearm of ten subjects and recorded the electrode-skin impedance, the motor threshold as identified using the EMG, and the first reported sensation upon increasing stimulation amplitude. Since these measures showed no

differences between TAMS and rectangular pulses, the authors concluded that it is unlikely that TAMS provides any efficacy improvement over conventional stimulation. In their animal studies, Shen *et al.* [45] used voltage-controlled TES, and therefore voltage- versus current-controlled stimulation may at least partially explain the purported benefits of TAMS on bladder control. Voltage pulses applied to the skin result in current peaks of few hundreds of  $\mu\text{s}$  that may be responsible for nerve fiber activation, whereas during current-controlled stimulation the skin voltage rises slowly [180]. Therefore, the tissue filtering effects in both types of stimulation may differentially affect nerve activation. However, our results suggest that such filtering plays a minimal role in fiber excitation using TAMS ( $>20$  kHz) because changing the relative amplitude of the carrier (as a proxy for filtering) had no effect on nerve fiber excitation. As well, prior modelling work showed that nerve fiber thresholds for 100 kHz TAMS and conventional pulses were the same for both voltage- and current-controlled stimulation [36]. Finally, TAMS will not improve the efficiency of stimulation, as the addition of high-frequency carriers on top of the offset only increases the delivered energy. Instead, transcutaneous stimulation may be more efficient using other stimulation waveforms that reduce energy and/or power required for peripheral nerve stimulation [181].

### **4.4.3 Limitations**

One of the limitations of our study was not including frequencies higher than 100 kHz. In the original formulation of TAMS, Shen *et al.* [45] used a carrier of 210 kHz, but it is unclear how this particular frequency was selected. However, the changes in skin conductivity and impedance between 100 kHz to 200 kHz are minimal [23, 118], and thus it is unlikely that we would observe different contributions to excitation between these frequencies. Further, a computational model of TES showed no difference in thresholds for axon activation using TAMS of 100 kHz and 200 kHz.

The axon model that we used in this study, the MRG model, has been used to model conduction block with kHz signal, and the results matched well the experimental data [32]. However, the model has not been thoroughly validated for activation of fibers using kHz signals. For such validation, the model may need to be updated. Firstly, the capacitance of the axon membrane exhibits dispersion, and its conductance declines by a factor of two between dc and 100 kHz [126]. Howell *et al.* [69] quantified the effects of dispersive capacitance by incorporating a frequency-dependent membrane capacitance,  $c(f)$ , in the MRG model. The threshold for generation of a single action potential using kilohertz sinusoidal signals applied for 10 ms declined by up to 14% after incorporating  $c(f)$  in a 11.5  $\mu\text{m}$  axon. Thus, it is possible that incorporating  $c(f)$  would further reduce thresholds in our simulations, but since we observed a greater effect of the offset, such reduction should be marginal. Finally, the MRG model does not include all ionic conductances present in human peripheral myelinated nerve fibers (*e.g.*, [103]), and the mathematical equations describing the dynamics of ion channel were constructed based on experimental observations with low-frequency signals. Therefore, further investigation is needed to determine if the number and type of channels and their responses to kHz signals can accurately describe axon activation using TAMS and other high-frequency signals.

## **4.5 Conclusion**

We performed *in vivo* experiments and computational simulations to quantify the effects of an amplitude-modulated signal with kilohertz carrier and non-zero offset, called TAMS, on nerve fiber activation. TAMS with carrier of 20 kHz or greater generated the same activation as a conventional rectangular pulse, even after increasing the size of the carrier. Therefore, the addition of high-frequency carriers ( $> 20$  kHz) to the stimulation signal did not improve efficacy or efficiency in peripheral nerve stimulation, and in particular in TES, in which kHz signals have been tested as a means to overcome the skin impedance.

## **Chapter 5: Computational Model of a Dorsal Column Fiber and Application to Spinal Cord Stimulation**

### **5.1 Introduction**

Spinal cord stimulation (SCS) is a well-established treatment for several chronic pain conditions, including failed back surgery syndrome, complex regional pain syndrome and post-amputation pain [182]. In SCS, a pulse generator delivers current via an electrode array lead implanted in the epidural space of the spinal cord to the dorsal columns (DCs). It is assumed that SCS relieves pain by activating DC fibers and thereby “closing the gate”, as described by the Gate Control Theory, although this theory only partially explains the mechanism(s) underlying SCS [183].

Computational models of SCS can provide insight into the effects of SCS on DC fibers and spinal circuits, and this knowledge can be used to predict SCS outcomes and to improve clinical applications [18]. For example, volume conductor models coupled to models of spinal axons were used to predict paresthesia thresholds [184], to improve electrode design [185], and to evaluate the efficiency of intradural versus epidural electrodes [2]. However, models of SCS have largely relied on fiber models developed for peripheral nerve fibers, and therefore these models may not represent accurately the excitation properties of DC fibers.

Recently, kilohertz-frequency (KHF) SCS was proposed to relieve pain without paresthesia, *i.e.*, the tingling sensation over the pain area that occurs concomitant with pain relief [6, 9]. In KHF-SCS, short duration biphasic pulses are delivered at 10 kHz, a rate that is much higher than the ~50 Hz commonly used in SCS. The mechanisms of KHF-SCS are not understood, and specifically, it is unclear how DC fibers respond to the KHF waveform.

The objective of this study was to develop a cable model of a DC fiber, validate the model using *in vivo* experimental recordings, and then quantify the responses of model DC fibers

to electrical stimulation of the spinal cord, in particular using KHF signals. By coupling the fiber model to a finite element model of human SCS, we show that thresholds for activation and block of DC fibers exceed the stimulation intensities used clinically. The firing activity that was evoked was largely asynchronous to the stimulation signal and to the firing of other fibers.

## **5.2 *The dorsal columns***

### **5.2.1 Overview**

The dorsal columns (DCs) are white matter in the dorsomedial space of the spinal cord. While a substantial minority of the fibers in the DCs are second-order postsynaptic sensory units, about 85% are branches of myelinated primary afferents fibers that enter the spinal cord via dorsal roots (DRs) [186]. These primary afferents arise from receptors in the skin, subcutaneous tissue and muscle joints. Upon entering the spinal cord, they follow a medial course to reach the DCs and send a caudal and a rostral branch, in a Y-shape fashion. As they ascend, the DC fibers send collaterals to the grey matter at different levels in the spinal cord, and many actually leave the DCs. In fact, only 25% of the fibers entering the DCs at lumbar level reach the dorsal column nuclei in the cat [187], and there is evidence that this is also the case in monkeys and humans [186].

### **5.2.2 Fiber morphology**

Since the vast majority of DC fibers are branches of primary afferents, it is expected that they maintain many morphological characteristics of peripheral sensory fibers. However, as they enter the central nervous system (CNS) via spinal cord, several differences emerge. First, DC fibers conduct more slowly than the corresponding section in the peripheral nervous system (PNS), most likely due to fiber diameter reduction after branching [188, 189]. In the human DC, the distribution of fiber diameters has a peak near 2  $\mu\text{m}$  [20]. Secondly, the myelin sheath is

thicker in the PNS [190, 191]. In contrast to Schwann cells that form a single internode in a single PNS fiber, oligodendrocytes contribute to the formation of several internodes in several fibers in the CNS [190]. Notwithstanding these differences, the fine structural morphology of the myelin sheath, *i.e.*, multilamellar conformation wrapped spirally around the fiber, is essentially the same in CNS and PNS fibers.

The myelin thickness is typically characterized using the *g-ratio*, *i.e.*, the ratio of axon diameter,  $axonD$ , which excludes myelin, to fiber diameter,  $fiberD$ , or fiber thickness including the myelin sheath;  $g-ratio = axonD/fiberD$ . In addition, if the fiber is considered as two concentric cylinders, the outermost representing the myelin sheath, then the myelin thickness,  $MT$ , is approximated by  $MT=(fiberD-axonD)/2$ . Since  $MT$  increases with increasing  $axonD$  [190], and the population of DR fibers contains thicker fibers than DC, the  $MT$  of DR fibers is larger [192]. However, for fibers of the same size, DC fibers show slightly greater *g-ratio* than DR fibers, *i.e.*, thinner myelin. Importantly, there is a nonlinear relationship between *g-ratio* and  $axonD$  so that smaller diameter axons show a steeper increase of *g-ratio* with  $axonD$  compared to larger axons, and this observation is confirmed by measurements of the myelination ratio, *i.e.*, the inverse of *g-ratio* [193].

### 5.2.3 Ion channels

The identity and quantity of ion channels in DC fibers has not been completely determined. However, ion channels have been identified and characterized in peripheral motor, and in particular peripheral sensory nerve fibers, and may be - and in fact some are - expressed in DC fibers, as well. Human peripheral nerve fibers contain at least two functionally distinct types of Na<sup>+</sup> channels, and approximately 98% of nodal sodium channels are of the transient type with fast activating and inactivating kinetics [194]. In addition, a non-inactivating or slowly activating sodium current has been identified in various mammalian neurons including in the DR ganglion

[195]. In DC fibers, the fast Na<sup>+</sup> current has been directly identified [196], and it is very likely that these fibers contain persistent Na<sup>+</sup> currents, as well. Further, the predominant sodium channel isoform in DC fibers is the Nav1.6 [197], and this isoform is also widespread throughout the peripheral nervous system [198]. The Nav1.6 isoform is associated with the so-called resurgent current, a current that reactivates during mild repolarizations following depolarization to positive potentials and may be critical in determining the firing patterns of cerebellar Purkinje neurons [199]. Large diameter dorsal root ganglion neurons but not small ones exhibit resurgent current [200], and resurgent current has been identified in PNS fibers as well [201, 202].

Slow potassium channels are present in highest density in the nodal region of the axonal membrane and possess slow deactivation kinetics [194]. These channels are involved in repolarization following conduction of a single impulse, and are widespread in both the CNS and PNS. Further, fiber excitability is regulated by slow potassium currents, and deficiencies in the function of the slow potassium channel, KCQN, causes neuronal hyper-excitability [203]. The Shaker-type potassium channel Kv1.2 has also been found in DC fibers, segregated within the juxtaparanodal region and in much lower density in the internode [197]. The Kv1-type channels produce fast-acting potassium currents, which are likely to be responsible for limiting re-excitation following conduction of an action potential.

A non-specific voltage-gated inwardly rectifying current, I<sub>h</sub>, has been described in peripheral sensory fibers [103]. This current is mediated by hyperpolarization-activated cyclic nucleotide-gated (HCN) channels and is activated by hyperpolarization. Since I<sub>h</sub> appears to be more active in sensory than motor neurons, it is likely that I<sub>h</sub> plays a role in the differences in accommodation to hyperpolarization, and I<sub>h</sub> modifies various electrophysiological properties, *e.g.*, recovery cycle. It is possible that DC fibers express HCN channels, thereby maintaining the electrophysiological properties that these channels confer on sensory primary afferents.

## 5.3 Methods

### 5.3.1 Model development

We developed a model of a dorsal column (DC) fiber based on a double-cable model of a peripheral nerve fiber, the McIntyre-Richardson-Grill (MRG) model [86]. We updated the morphology and ion channel dynamics of the MRG model to represent better a DC fiber, incorporated a frequency-dependent membrane capacitance (FDMC), and added a mechanism to account for activity-dependent changes in extracellular potassium concentration.

#### 5.3.1.1 Morphology

Our DC fiber model included explicit representation of the myelin and detailed morphology of nodal and internodal sections, as in the MRG model. In addition to the node of Ranvier, the fiber model included paranodal or myelin attachment sections (MYSA), juxtaparanodal sections (FLUT), and the internodes (STIN), and the sections were connected following the sequence: node-MYSA-FLUT-STIN-FLUT-MYSA-node, etc. In the MRG model, the morphological parameters were defined for a discrete set of fiber diameters from 5.7 to 16  $\mu\text{m}$ , and the parameters included axon diameter, myelin thickness, diameter of the node of Ranvier, diameter of the FLUT, and the lengths of the different sections. We defined fiber diameter,  $fiberD$ , as the ‘independent’ variable, and determined the remaining parameters as a function of  $fiberD$ . In our formulation,  $fiberD$  was not discrete, and could take any value between 2 – 16  $\mu\text{m}$ . We used experimental data on myelin thickness measured in rat DC fibers to determine the axon diameter,  $axonD$  [192], from the relationship  $g\text{-ratio} = axonD / fiberD$ . The axon diameter was well fitted by linear regression to ( $R^2 > 0.9$ ):

$$axonD = 0.73 \cdot fiberD - 0.75 \tag{5.1}$$

We determined the diameter of the node of Ranvier,  $nodeD$ , using data from cat dorsal root axons [204, 205]:

$$nodeD = 0.29 \cdot fiberD + 0.36 \quad (5.2)$$

We calculated the internode length,  $INL$ , and juxtaparanode length,  $JPL$ , by linear extrapolation of the respective MRG model parameters, which were taken from measurements in cat ventral root fibers:

$$INL = 92 \cdot fiberD + 108 \quad (5.3)$$

$$JPL = 2.6 \cdot fiberD + 19.6 \quad (5.4)$$

Equation (5.3) matched well with measurements in rabbit ventral spinal fibers [206], and cat DCs [207], and the  $JPL$  has not been measured in spinal axons. Finally, the node and paranode lengths were independent of  $fiberD$  and equal to 1 and 3  $\mu\text{m}$ , respectively, similar to findings in dorsal root fibers of different diameters [208].

### 5.3.1.2 Ion channels

In addition to the membrane dynamics used in the MRG model, *i.e.*, fast and persistent sodium, slow potassium, leakage, and capacitive currents, the DC fiber model incorporated a fast potassium current in the juxtaparanode and a hyperpolarization-activated cation current, *i.e.*, HCN channel, in the internode. We used the Hodgkin-Huxley mathematical formulation to describe the channel kinetics of all non-linear channels (see Appendix B).

### 5.3.1.3 Frequency-dependent membrane capacitance

All biological tissues show dispersion, *i.e.*, variation of their dielectric properties with frequency [115]. This phenomenon also manifests in the cell membrane, and as the frequency

extends to the kilohertz range, the axonal membrane capacitance declines so that by 100 kHz it is reduced to half the value at dc [209]. Thus, membrane capacitance can have an impact on fiber excitation using kHz frequency signals. We developed a mathematical formulation of frequency-dependent membrane capacitance (FDMC) using a first order relaxation process, and incorporated it into all compartments of the fiber model. A detailed description of the implementation and the impact of FDMC on neural excitability was published elsewhere [69]. Briefly, a first order relaxation process is described by the equation:

$$c(f) = c_{\infty} + \frac{c_{dc} - c_{\infty}}{1 + j2\pi f \cdot \tau} \quad (5.5)$$

where  $c(f)$  is the FDMC,  $c_{\infty}$  is the capacitance for  $f \rightarrow \infty$ ,  $c_{dc}$  is the capacitance at dc, and  $\tau$  is the relaxation time. We fitted this model of dispersion to experimental data [209], and scaled the parameters to match the capacitance of mammalian fibers at dc [210]. Thus  $c_{dc} = 1 \mu\text{F}/\text{cm}^2$ ,  $c_{\infty} = 0.55 \mu\text{F}/\text{cm}^2$ , and  $\tau = (2\pi 10^4)^{-1}$  s. We used the ‘LinearMechanism’ in NEURON to define the ordinary differential equations that correspond to Equation (5.5).

#### 5.3.1.4 Dynamics of extracellular potassium concentration

We hypothesized that activity-dependent changes in extracellular  $\text{K}^+$  concentration could explain the profiles of firing rate of single DC fibers recorded *in vivo* during KHF-SCS (Crosby *et al.*, unpublished data). Therefore, we implemented a model of the dynamics of extracellular  $\text{K}^+$  concentration.

Electrical stimulation of peripheral nerves generated transient increases of extracellular  $\text{K}^+$  concentration in the spinal cord [211, 212], and accumulation of  $\text{K}^+$  in the extracellular space is a postulated mechanism of suppression of action potentials during high frequency stimulation

[105, 213, 214]. The changes in concentration are likely the result of the activity-dependent  $K^+$  contributions from many fibers or cells that produce outward  $K^+$  currents during repolarization of an action potential, and consequently, our model included the contribution of many nodes of Ranvier (Figure 5.1).

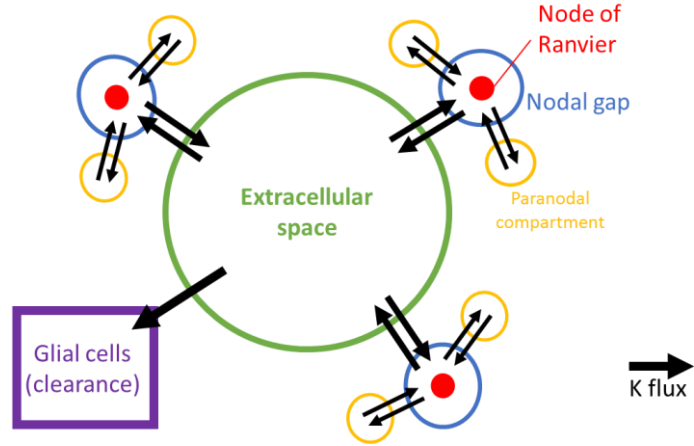


**Figure 5.1. Illustration of the model of extracellular potassium concentration.**

The model included contribution from many nodes of Ranvier to the extracellular bath, and clearance by glial cells.

The diffusion of potassium between a periaxonal volume enclosing a single node (nodal gap) and the extracellular bath, is well described by Fick's second law of diffusion:

$$J_{to-bath} = \frac{DA}{\Delta r} ([K]_{bath} - [K]_{node}) \quad (5.6)$$

$$J_{to-node} = \frac{DA}{\Delta r} ([K]_{node} - [K]_{bath}) \quad (5.7)$$

where  $J$  is the ion flux,  $D$  is the coefficient of diffusion,  $A$  is the area of  $K^+$  exchange, and  $\Delta r$  is the radius of the nodal gap. In Equation (5.6),  $J$  corresponds to the contribution of a single node of Ranvier. It follows that the total flux to the extracellular bath is:

$$J_T = \sum J_{to-bath} = N \frac{DA}{\Delta r} ([K]_{bath} - [K]_{node}) \quad (5.8)$$

In Equation (5.8), it was assumed that there are  $N$  nodes of Ranvier contributing to the flux and they are all identical. Additionally, glial cells and other mechanisms take up  $K^+$  from the bath to restore the concentration at rest,  $[K^+]_0$ , which we defined as 3 mM in accord with experimental measurements in the spinal cord [215]. Thus, the differential equations describing  $K^+$  concentration are:

$$\frac{1}{N_d} \frac{d}{dt} [K^+]_{bath} = \frac{DA}{\Delta r} ([K]_{bath} - [K]_{node}) - ([K^+]_{bath} - [K^+]_0) / \tau_{clearance} \quad (5.9)$$

$$V_{gap} \frac{d}{dt} [K^+]_{node} = \frac{DA}{\Delta r} ([K]_{node} - [K]_{bath}) \quad (5.10)$$

where  $N_d$  is the number of nodes of Ranvier per unit volume,  $\tau_{clearance}$  is the time constant of the first-order clearance mechanism, and  $V_{gap}$  is the volume of the nodal gap. Initially, we used  $1 < \tau_{clearance} < 50$  s, a range consistent with experimental observations [212, 216], and  $1e-4 < N_d < 1e-1$  nodes/ $\mu m^2$ /per length, a range encompassing values reported for human DCs [20].

Additional  $K^+$  clearance from the extracellular space occurred via  $Na^+/K^+$  pumps that were incorporated into the membrane of all nodal compartments. The  $Na^+/K^+$  pump current,  $I_{NaK}$ , was calculated using the equation [214]:

$$I_{NaK} = I_{NaKmax} \frac{[K^+]_o}{[K^+]_o + K_{mK}} \cdot \frac{[Na^+]_i^{1.5}}{[Na^+]_i^{1.5} + K_{mNa}^{1.5}} \cdot \frac{V_m + 150}{V_m + 200} \quad (5.11)$$

where  $I_{NaKmax}$  is the maximum conductance of the pump,  $V_m$  is the transmembrane potential, and  $K_{mK}$  and  $K_{mNa}$  are the equilibrium binding constants.

### 5.3.2 Model validation

We validated the DC fiber model using published experimental data of action potential shape, conduction velocity and current-distance relationship, and *de novo in vivo* recordings of the strength-duration relationship and the recovery cycle of single DC fibers in anesthetized rats (Section 5.3.5).

We applied extracellular stimulation using either a monopolar point-source electrode or two point-source electrodes separated by 2 mm that delivered currents in an infinite medium with homogenous and anisotropic conductivity. The longitudinal ( $\sigma_z$ ) and transverse ( $\sigma_{xy}$ ) conductivities were 1/3 and 1/12 S/m, respectively [217]. We calculated the extracellular potentials,  $\Phi(x,y,z)$ , using the following function:

$$\Phi(x, y, z) = \sum_{i=1}^N \frac{(pol_i) \cdot I_s}{4\pi\sqrt{\sigma_{xy}\sigma_z((x-x_i)^2 + (y-y_i)^2) + \sigma_{xy}^2(z-z_i)^2}} \quad (5.12)$$

where  $x_i$ ,  $y_i$  and  $z_i$  are the electrode coordinates,  $pol_i$  is the polarity of electrode  $i$ ,  $I_s$  is the stimulus amplitude, and  $N=1$  for monopolar and 2, for bipolar. We placed the fibers parallel to the line connecting the bipolar electrodes at different distances from the electrode(s). We calculated the extracellular potentials in MATLAB and used the ‘extracellular’ mechanism in NEURON (v7.3) to apply extracellular stimulation to the model fibers. The equations were solved using backward Euler integration and the time step was 0.05 ms, except where indicated. Thresholds were calculated using a bisection algorithm (relative error < 1%), and the membrane potential at the recording node was inspected *post hoc* to ensure that at least one action potential was evoked. In

some tests, we used other fiber models for comparison, namely the MRG model [86], the Sweeney model [218], and the Wesselink model [219].

We calculated the conduction velocity (CV) of the model fibers by applying a suprathreshold 250  $\mu\text{s}$  rectangular stimulus to a 101-node fiber and averaging local conduction velocities of the propagation of the action potential from node to node. CV is the most common electrophysiology property measured for DC fibers and has been estimated from both single fiber recordings and compound action potentials [188, 217, 220, 221]. Despite the wealth of CV data, a direct validation of the model is not straightforward since CV is strongly dependent on fiber diameter, which is unknown in the experimental recordings. We calculated CV for fiber diameters from 2 to 12  $\mu\text{m}$ , and compared it to the experimentally measured ranges of CV.

The current-distance relationship quantifies the threshold for fiber activation as a function of electrode-to-fiber distance and is well described by the equation [86]:

$$I_{th} = I_o + k \cdot r^2 \quad (5.13)$$

where  $I_{th}$  is the threshold,  $I_o$  is the offset,  $k$  is the slope, and  $r$  is the electrode-to-fiber distance. The current-distance relationship was recorded for nearly 100 cat DC fibers grouped by their CV [217]. It was assumed that DC fibers maintained a constant position in relation to the surface and the midline over several spinal segments, *i.e.*, the electrode-to-fiber distance roughly corresponded to the penetration and distance to the midline of the recording electrode [217]. We simulated this experiment by first estimating fiber diameter using the reported CV, thereby obtaining a representative diameter for each group. We then applied extracellular stimulation and placed a monopolar electrode at a random perpendicular distance to the fiber in the 100-1100  $\mu\text{m}$  interval, and at random horizontal displacements in the 0-INL/2 interval, where INL is the

internodal length. We then calculated thresholds and fitted the results to Equation (5.13) using nonlinear least squares regression.

The threshold stimulus necessary for fiber activation increases as the duration of the rectangular stimulus is decreased, and this phenomenon is described by the strength-duration (SD) relationship. Experimental data are in general well fitted by the Weiss equation:

$$I_{th} = I_{rh} \cdot \left(1 + \frac{T_{ch}}{PD}\right) \quad (5.14)$$

where  $I_{th}$  is the threshold current,  $PD$  is the pulse duration,  $I_{rh}$  is the rheobase, and  $T_{ch}$  is the chronaxie. The SD curve depends on fiber diameter [86] and stimulation modality [222, 223]. Therefore, we calculated a family of SD curves representing fiber diameters between 2 and 10  $\mu\text{m}$ , using a bipolar electrode pair positioned at 3 different distances from the fiber (0.2, 0.4 and 0.6 mm) and at 5 horizontal displacements with respect to the middle node (0,  $\pm 0.25$  and  $\pm 0.5$  internodal lengths). We calculated thresholds and fitted the results to Equation (5.14) with rheobase constrained to  $\pm 5\%$  of the threshold for a 1 ms pulse.

The recovery cycle (RC) quantifies the variations in threshold for a second pulse delivered at different intervals after a first (conditioning) supra-threshold pulse [84]. To quantify the RC, the threshold for the second 0.5 ms rectangular pulse was measured as a function of the inter-pulse interval (IPI) using fiber diameters from 2 -10  $\mu\text{m}$  at an electrode-to-fiber distance of 0.6 mm using a monopolar point source electrode positioned over the middle node of Ranvier.

Finally, we quantified the firing activity of model DC fibers using the firing rate as a function of time, and compared the activity to that of single DC fibers recorded *in vivo* during KHF-SCS (Crosby *et al.*, unpublished data). We applied the KHF-SCS signal for 20 s to model fibers placed at distances between 0.1 and 1 mm from the bipolar electrode, and we used

amplitudes between 0.1 – 8 mA. We calculated the firing rate as a function of time by averaging the number of spikes in a time window of 1 s shifted in steps of 0.1 s.

### 5.3.3 Patient-specific model of spinal cord stimulation

We used a finite element model (FEM) of spinal cord stimulation (SCS) in humans to calculate the potentials generated by epidural SCS [2]. The geometry of the FEM model was constructed using MRI data from 5 human subjects (Figure 5.2A), and included an implanted three-contact epidural electrode that delivered bipolar stimulation. The model was implemented in COMSOL Multiphysics v3.4. We placed 40 model fibers close to the midline of the DCs (Figure 5.2B) and extracted the potentials corresponding to the locations of the compartments of each DC fiber. We multiplied the potentials by a single rectangular pulse of 300  $\mu$ s, or by a train of 30  $\mu$ s per phase biphasic pulses of delivered at 10 kHz, and applied them to the DC fiber model in NEURON (v7.3) to calculate thresholds for excitation and conduction block using the method described in [32]. We note that the initiation of the KHF signal at amplitudes sufficient to produce block was often accompanied by an onset activation, *i.e.*, a finite number of action potentials generated immediately after the electrode was turned on, within a time window of few milliseconds. Fiber length was 300 mm in all cases to cover the entire length of the DCs in the volume conductor, and we used fiber diameters between 2 and 14  $\mu$ m. The vast majority of DC fibers are  $\sim$  2-3  $\mu$ m in diameter, and the largest fibers are about 10-11  $\mu$ m (Figure 5.2C). Additionally, for a subset of superficial fibers (Figure 5.2B) we recorded activity during continuous application of the KHF-SCS signal for 500 ms using different amplitudes of stimulation, and quantified the patterns of activity using the metrics described in Section 5.3.4.

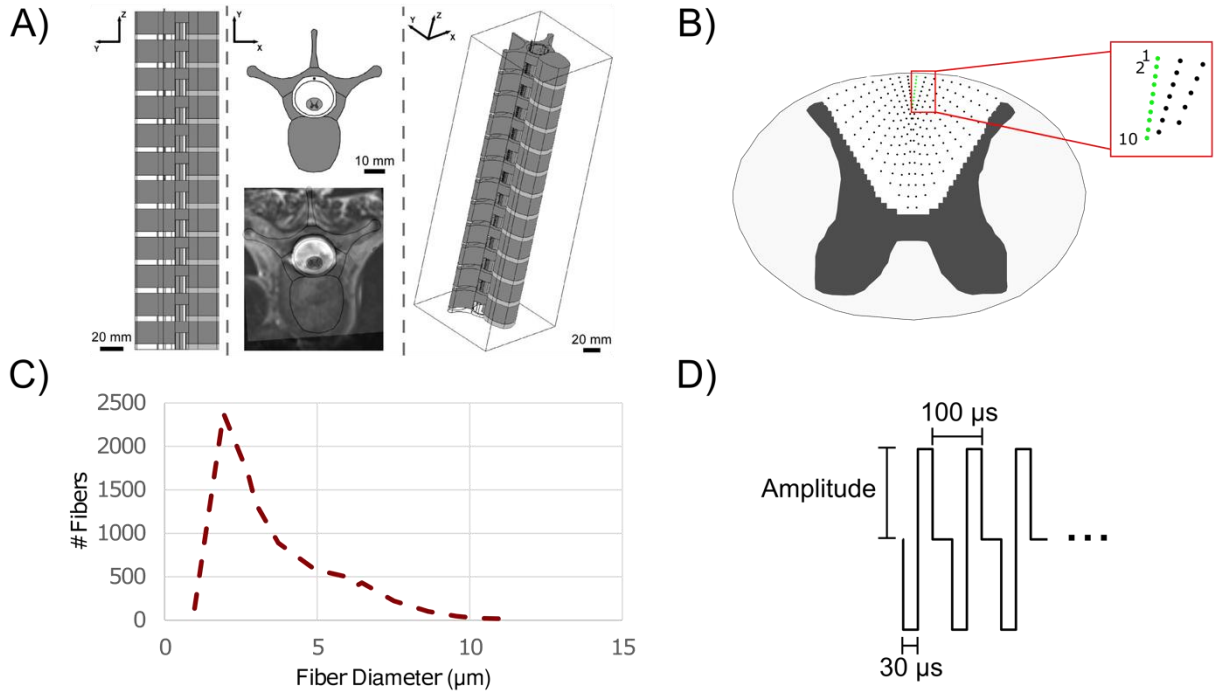


**Figure 5.2. Human model of spinal cord stimulation using kilohertz-frequency signals.**

A) Finite element model of spinal cord stimulation in humans. The geometry of a vertebra and the spinal cord was constructed from MRI images of the spine. The model included several identical vertebrae and an epidural electrode was placed to generate potentials. Sagittal and transverse views of the model are illustrated. Modified from [2]. B) Transverse section of the spinal cord and the location of the fibers in the dorsal columns. Thresholds were quantified for the locations represented as black dots closest to and on both sides of the midline (40 fibers total), and activation patterns were quantified for the subset of locations shown in green. C) Histogram of fiber diameter in the human dorsal column. Adapted from [20]. D) Illustration of the KHF-SCS waveform.

### 5.3.4 Metrics to quantify activation patterns

We used the vector strength to quantify the synchronization of model fiber activity to the stimulation signal, [224]. The vector strength,  $r$ , measures the synchrony of the spike train to the stimulation pulse train using the phase between each spike and the closest stimulation pulse, and is defined as:

$$r = \sqrt{\left(\sum x_i\right)^2 + \left(\sum y_i\right)^2} / n \quad (5.15)$$

where  $x_i = \cos(\theta_i)$ ,  $y_i = \sin(\theta_i)$ , and  $\theta_i$  is the phase angle between the  $i$ -th spike and the closest stimulation pulse. Thus,  $r=1$  implies perfect phase synchrony, and  $r=0$  implies a random relation between stimulus and response.

We used the Hamming distance and the spike train distance to quantify the (dis)similarity between the activity generated by the KHF-SCS signal in two model nerve fibers (Figure 5.3). The Hamming distance [225] between two strings of the same length is the number of positions with different symbols. For each spike train, we constructed a string of the number of spikes within bins of  $T$  ms. We calculated the Hamming distance,  $h$ , between the strings  $S_a$  and  $S_b$  using the formula:

$$h = \sum S_a(i) \neq S_b(i) / N \quad (5.16)$$

where  $N$  is the length of the string.

The spike train distance [226],  $d(q)$ , was calculated as the minimum cost of transforming  $S_a$  into  $S_b$  by means of three basic operations (Figure 5.3): spike insertion (cost 1), spike deletion (cost 1) and shifting a spike by some interval  $\Delta t$  (cost  $q|\Delta t|$ ), with  $q$  the cost of shifting per time unit. For  $q=0$ , the spike train distance is simply the difference in spike counts, while for large  $q$  the distance approaches the number of non-coincident spikes because it is less costly to delete and reinsert all non-coincident spikes than to shift them. Thus, by increasing  $q$  the distance is transformed from a rate distance to a temporal distance. We used  $q=1 \text{ ms}^{-1}$  and normalized  $d(q=1)$  by the spike train distance  $d(q \rightarrow \infty)$ .

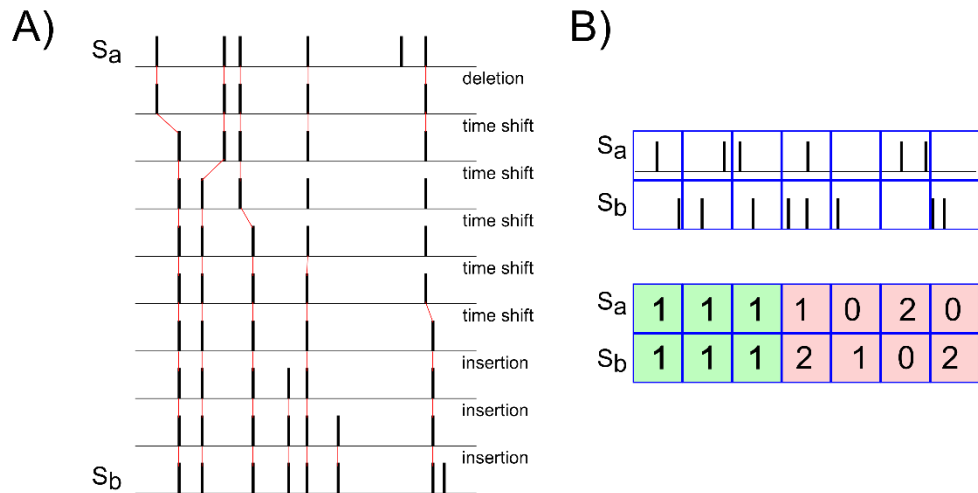


**Figure 5.3. Metrics of spike train similarity.**

A) Example of calculation of the spike time distance between two spike trains,  $S_a$  and  $S_b$ , using insertion, deletion and time shift of spikes. The distance is calculated as the cost to transform  $S_a$  into  $S_b$  by applying these operations. Adapted from [226]. B) Example of calculation of the Hamming distance between  $S_a$  and  $S_b$  using the bins depicted in blue. Four out of 7 bins contain different number of spikes (red boxes), i.e., the Hamming distance is 4/7 in this case.

### 5.3.5 Experimental measurements

We recorded the strength-duration relationship and the recovery cycle of single fibers *in vivo* in urethane anesthetized rats. We applied epidural stimulation at the cervical level of the spinal cord and recorded the responses of individual fibers at the lumbar level using high impedance metal microelectrodes. We quantified thresholds for eliciting action potentials using rectangular pulses for each test, as described below.

#### 5.3.5.1 Animal preparation

All animal care and experimental procedures were approved by the Institutional Animal Care and Use Committee of Duke University. Male Sprague-Dawley rats (300–500 g) were initially anesthetized by inhalation of 3.0% isoflurane and subcutaneous injection of urethane (1.2 g/kg). Supplemental intraperitoneal doses of urethane (0.4 g/kg,) were administered if a withdrawal reflex occurred in response to pinching of the hindpaw. Following tracheotomy, the

animal was connected to a pressure-controlled ventilator (Kent Scientific MouseVent G500). Oxygen saturation and heart rate were monitored using a pulse oximeter (Kent Scientific MouseVent G500 module) on the hindpaw and maintained within physiological levels (SpO<sub>2</sub> > 90%, heart rate < 450 bpm). Body temperature was maintained at 35–37°C using a heating blanket (Gaymar T/Pump). The head was mounted in a stereotaxic frame (Kopf Instruments), and the vertebral column was suspended from vertebral clamps (Kopf Instruments). Laminectomies were performed to expose the cervical (C1) and thoracic-lumbar (T10-L2) spinal cord. The dura over the thoracic-lumbar region was resected and the pia of the target spinal surface was removed carefully using fine forceps. At the completion of the surgery, but before fiber recording, the animal was paralyzed using gallamine triethiodide (20 mg/h; Sigma-Aldrich) delivered through an intraperitoneal catheter. A 1.5 mm wide bipolar paddle electrode with 1.0-mm-long platinum electrodes spaced 2.0 mm apart was inserted into the epidural space at C1 to deliver stimulation. A recording microelectrode (stainless steel, 8-10 MΩ impedance; Microprobes) was lowered into the middle posterior lumbar spinal cord, and a search stimulus (pulse duration: 0.5 ms, amplitude < 500 μA,) was applied to the C1 stimulation electrode at 1 Hz while the recording electrode was advanced and retracted through the dorsal columns until a unit was observed to follow the search stimulus, *i.e.*, a candidate fiber was found. Neuronal signals were amplified and filtered using an X-Cell amplifier (gain = 10,000, passband = 500-2,000 Hz; FHC), recorded using a Powerlab data acquisition system (ADInstruments), and sorted *post hoc* using manual principal component-based clustering in Offline Sorter (Plexon). We used two criteria to verify that the unit was indeed a fiber activated by the C1 stimulus: the fiber followed single pulse C1 stimulation at a latency that varied less than the pulse width of the search stimulus, and the fiber followed triplets of C1 stimulation delivered at > 200 Hz.

### **5.3.5.2 Strength-duration relationship**

We recorded the SD relationship of 4 fibers from 3 different animals. We applied pulses using the C1 electrode, and the pulse duration was in the range 20 – 1000  $\mu$ s, similar to other studies [217]. For each pulse duration, we applied stimulation of increasing amplitude until an action potential was elicited. We defined threshold as the minimum stimulus amplitude that elicited at least 2 action potentials for three applied pulses.

### **5.3.5.3 Recovery cycle**

We recorded the RC of 10 different fibers from 8 animals. First, we estimated roughly the threshold for a single pulse of 0.5 ms by applying pulses of increasing amplitude until an action potential was elicited. Then, we applied pairs of pulses at different IPIs, and we kept the amplitude of the first pulse at 50% above threshold, *i.e.*, a supra-threshold stimulus. We varied the amplitude of the second pulse between -40% and +40% of threshold, using a step of 2%. The threshold for the second pulse was estimated offline as the minimum amplitude of the second pulse that elicited at least 2 action potentials for three applied second pulses.

## **5.4 Results**

### **5.4.1 Model validation**

#### **5.4.1.1 Action potential shape and conduction velocity**

Action potentials of single dorsal column (DC) fibers were recorded using intra-axonal electrodes in response to dorsal root and DC extracellular stimulation [227, 228]. The model action potential resembled that recorded by [228] with similar amplitude ( $> 100$  mV), but differed from the recordings of [227] in amplitude (model:  $\sim 120$  mV, data:  $\sim 60$  mV) and width (model:  $< 1$  ms, data:  $\sim 2$  ms) (Figure 5.4). The range of conduction velocity (CV) calculated using the fiber

model matched well the experimental measurements for fiber diameter within the reported range for rat, cat and sheep DC fibers (Figure 5.4).

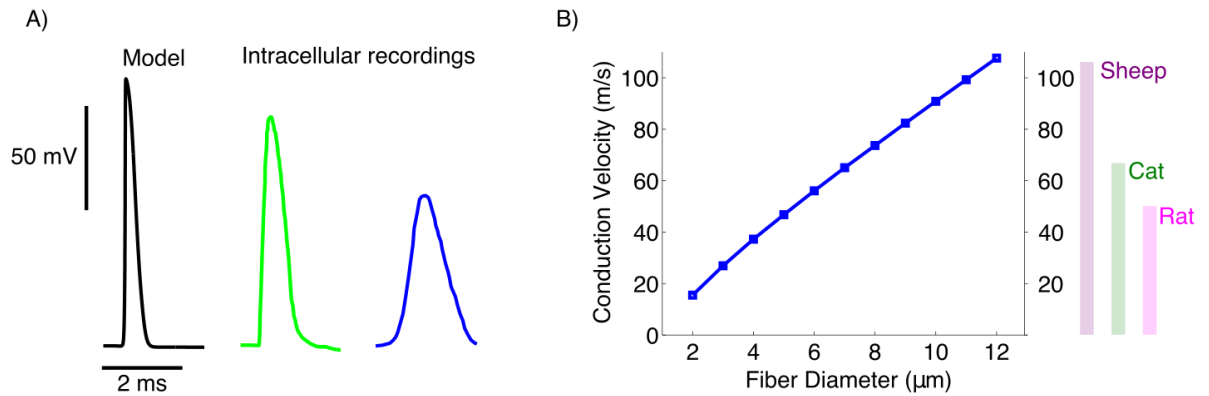


**Figure 5.4. Action potential shape and conduction velocity of DC fibers.**

A) Comparison of action potential shape of model (left), and intra-axonal recordings of rat DC fibers (middle, Kocsis and Waxman 1982; right, Kohama et al 2001). B) Conduction velocity as a function of fiber diameter for the DC fiber model, and the experimentally measured range (bars) in rat [220, 229], cat [217] and sheep [221].

#### 5.4.1.2 Current-distance relationship

The current-distance relationship calculated with the DC fiber model matched well experimental measurements in cat DCs [217] for electrode-to-fiber distances  $\leq 600 \mu\text{m}$ , and thresholds were slightly underestimated for larger distances ( $>800 \mu\text{m}$ ), especially for smaller diameter fibers (Figure 5.5). The MRG model showed similar results, but somewhat lower thresholds. The offset,  $I_0$  (see Equation (5.13)), for the model current-distance curves was 31.1, 38.6, 43.9 and 54.6  $\mu\text{A}$ , respectively, (experimental range: 0-25  $\mu\text{A}$ ), and the slope,  $k$ , was 252.2, 185.0, 148.2 and 125.0  $\mu\text{A}/\text{mm}^2$ , respectively (experimental range 120-270  $\mu\text{A}/\text{mm}^2$ ).

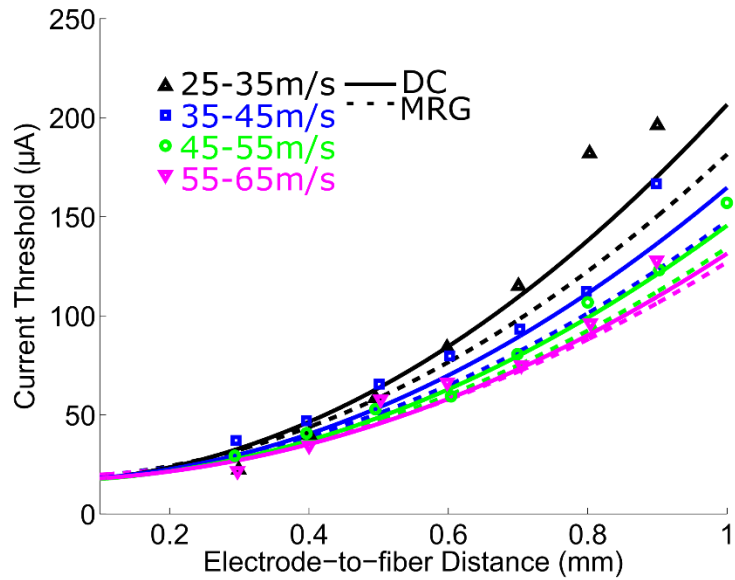


**Figure 5.5. Current-distance relationship of DC fibers.**

The current-distance relationship measured experimentally for 94 DC fibers (BeMent and Ranck, 1969) grouped by conduction velocity (symbols), and calculated using the DC fiber model (solid lines) and the MRG model (dashed lines). For the fiber models, fiber diameter was selected to represent each conduction velocity group, and the thresholds were averaged over a number of fiber locations.

### 5.4.1.3 Strength-duration relationship

The SD relationship of the DC fiber model matched well with our experimental data as well as previous measurements on DC fibers [217] (Figure 5.6). The average chronaxie of the model was 70.4  $\mu$ s (59.4 - 82.3  $\mu$ s) was comparable to that from the experimental data 73.4  $\mu$ s (55.1 - 85.9  $\mu$ s).

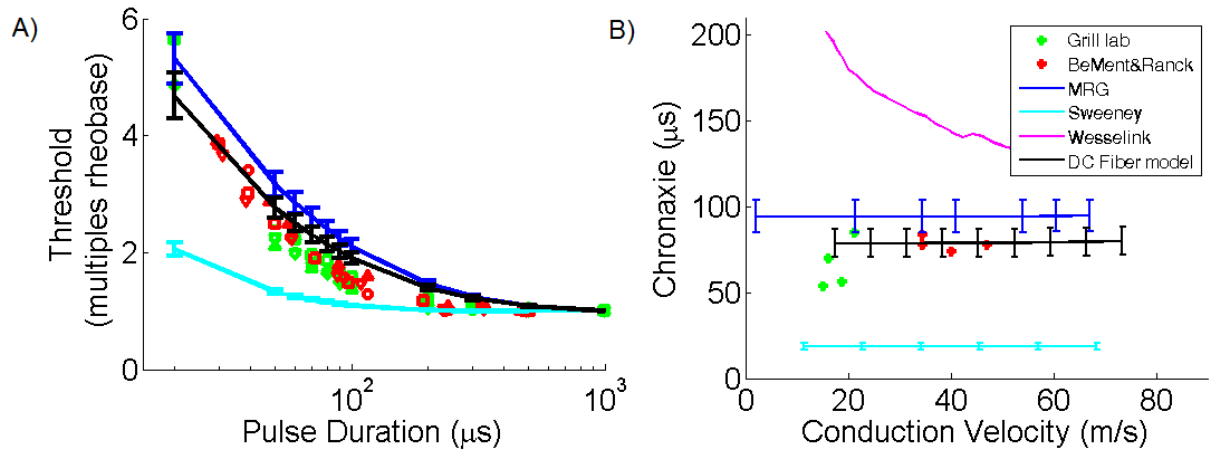


**Figure 5.6. Strength-duration relationship of DC fibers.**

A) Strength-duration relationship for 8 DC fibers (green symbols: our data, red symbols: BeMent and Ranck data) and simulation results for three fiber models: DC fiber model (black), MRG model (blue), and Sweeney model (cyan). B) Chronaxies measured experimentally and predicted by 4 different fiber models (error bars: standard deviation).

#### 5.4.1.4 Recovery cycle

Consistent with findings in the peripheral nervous system, the recovery cycle (RC) of the DC fibers exhibited a supranormal period, *i.e.*, lower threshold, in the 2 – 10 ms IPI range, followed by a subnormal period, *i.e.*, higher threshold, in the tens of ms range (Figure 5.7). After 100 ms, the majority of fibers recovered full excitability. Using measurements of conduction velocity, the estimated fiber diameter of the recorded units was between 1.9 – 4.8  $\mu\text{m}$ . The DC fiber model matched quite well the experimental data, and in particular, the smallest fiber model (2  $\mu\text{m}$ ), exhibited a recovery cycle that fit well within the 95% confidence intervals.

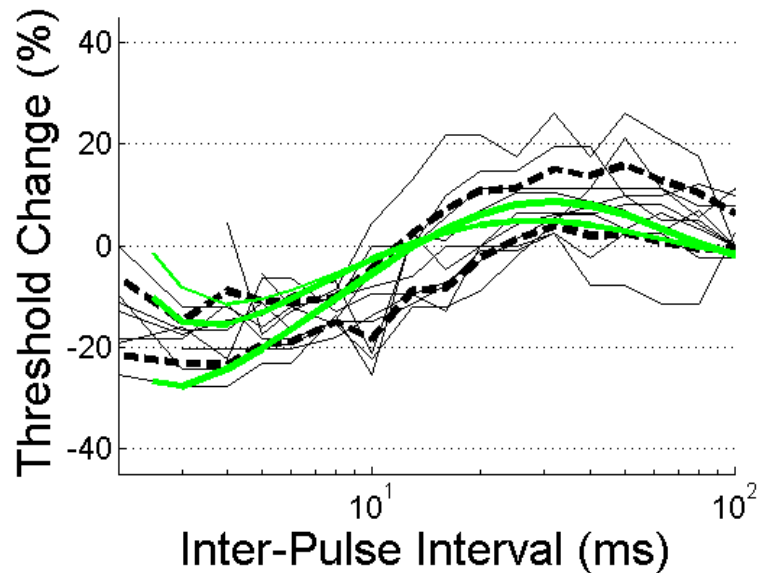


**Figure 5.7. Recovery cycle of DC fibers.**

Recovery cycle of 10 DC fibers (solid black lines) and model predictions. Dashed lines: 95% confidence intervals. Green lines: DC fiber model predictions for fiber diameters of 2  $\mu\text{m}$  (thick line) to 10  $\mu\text{m}$  (thin line).

#### 5.4.2 Dynamic effects of extracellular potassium concentration

We applied a train of pulses at 50 Hz and recorded the ion concentration in the space around the node of Ranvier (Figure 5.8). For a low density of nodes of Ranvier in the extracellular space, the fiber fired synchronously with the stimulation signal (Figure 5.8A), and when the stimulus was turned off,  $\text{K}^+$  was slowly cleared from the extracellular space according to the first-order dynamics of the clearance mechanism. After increasing the node density, the total flux of  $\text{K}^+$  into the extracellular space increased markedly (Figure 5.8B). Axonal conduction was blocked at about 2 s due to  $\text{K}^+$  accumulation – resulting in axonal depolarization and inactivation of  $\text{Na}^+$  channels – that exhausted the clearance mechanism, and even after the stimulus was stopped the fiber remained blocked. Under these conditions, the depolarized membrane increased the conductance of the  $\text{K}^+$  channels, thereby creating a positive feedback

loop. An equilibrium was reached after several seconds when the efflux of  $K^+$  from many nodes equaled the clearance and the extracellular concentration plateaued.

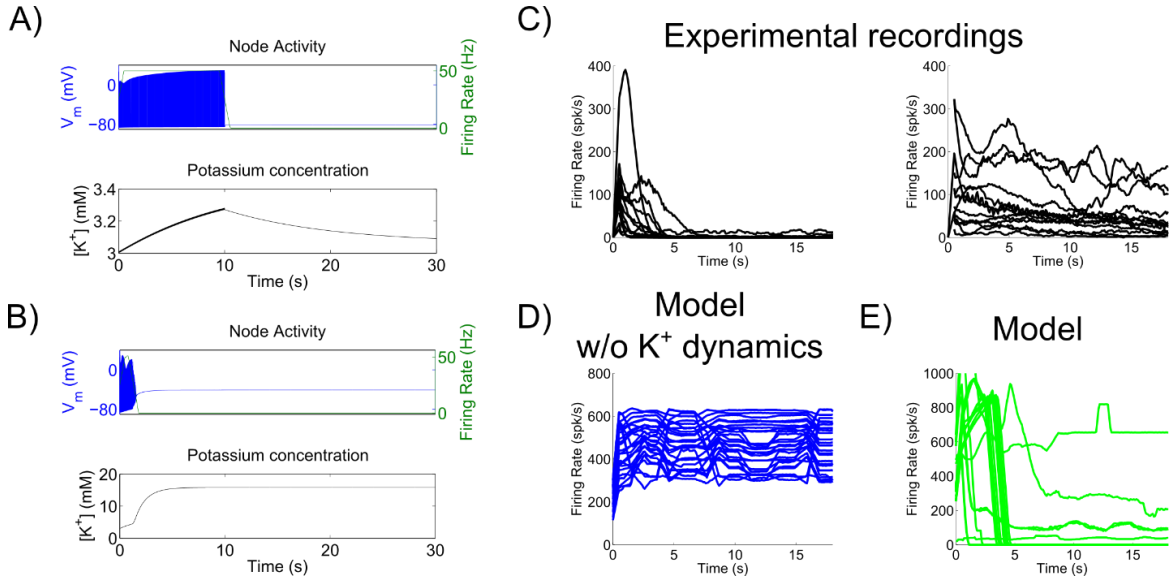


**Figure 5.8. Effects of potassium diffusion.**

A,B) Node potential and  $K^+$  concentration dynamics using 50 Hz stimulation applied during 10 s, for A) low node density ( $N_d=1e-3 \mu m^{-2}$ ), and B) high node density ( $N_d=1e-1 \mu m^{-2}$ ). C) Firing rate of DC fibers recorded experimentally (Crosby *et al.*, unpublished data). D,E) Firing rate of the DC fiber model during stimulation with the KHF-SCS signal of different amplitudes and at different distances to the electrode, without (D) and including (E) the model of potassium concentration dynamics.

We applied the KHF-SCS signal for 20 s and calculated the firing rate as a function of time for a number of stimulus amplitudes and electrode-to-fiber distances, and compared the model responses to experimental recordings of single DC fibers (Crosby *et al.*, unpublished data) (Figure 5.8). The experimental recordings exhibited firing activity that in some cases lasted for only a few seconds (Figure 5.8C, left), and in others, persisted beyond 20 s with a firing rate that decayed as time progressed (Figure 5.8C, right). The DC fiber model replicated these behaviors, *i.e.*, it exhibited onset firing activity for few seconds in some cases, and a time-decaying firing rate in others, although the firing rate ranges were higher as compared to the experimental data (Figure 5.8E). The model of  $K^+$  concentration was necessary to match the profile of firing rate

activity observed experimentally, and without  $K^+$  concentration dynamics, the model fiber exhibited firing rates that did not decay with time (Figure 5.8D).

### 5.4.3 Thresholds calculated in a patient-specific model of spinal cord stimulation

We quantified activation (Figure 5.9, Figure 5.10) and block (Figure 5.11) thresholds using a model of SCS in human coupled to the DC fiber model. Activation thresholds using the KHF-SCS signal increased sharply for fibers positioned deeper in the DCs, and larger diameter fibers exhibited lower thresholds. The minimum thresholds, *i.e.*, for large, superficial fibers, were  $> 5$  mA, the upper limit used clinically for KHF-SCS [6]. In contrast, the activation thresholds using a conventional 50 Hz SCS signal were on the order of few mA for large, superficial fibers, and at any given depth in the DCs, the thresholds for conventional 50 Hz SCS were up to five times lower than the thresholds for KHF-SCS. Thresholds for conduction block with the KHF-SCS signal were higher than about 30 mA for all fiber diameters and locations in the DCs.

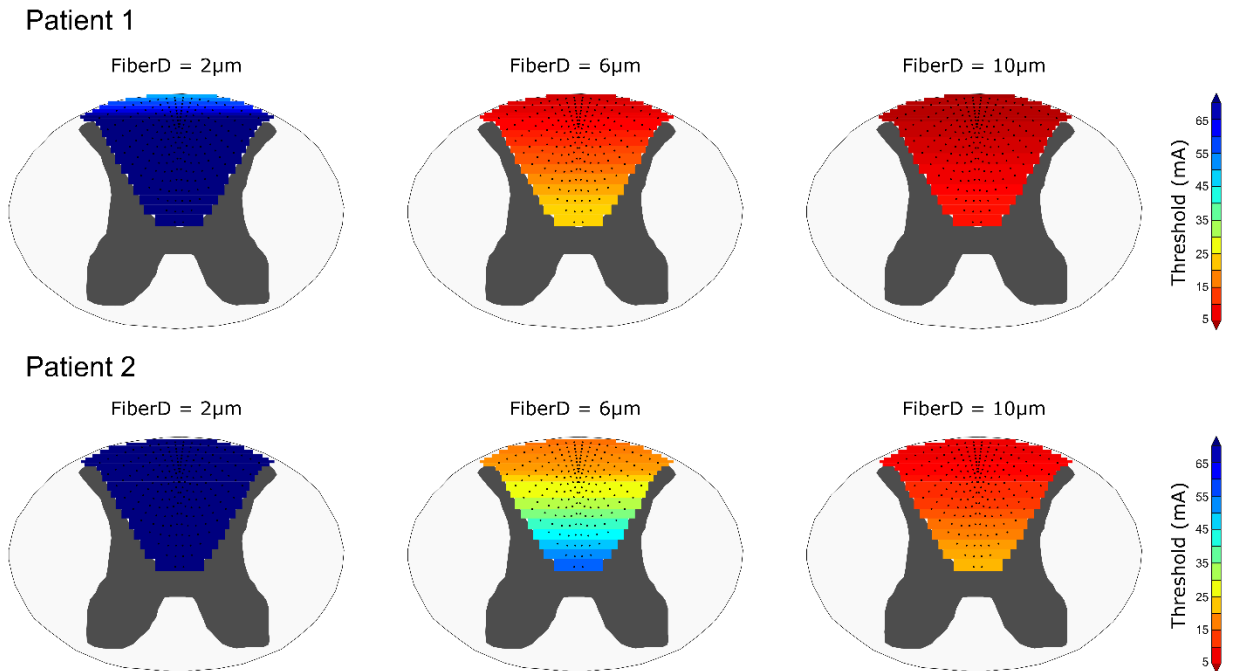
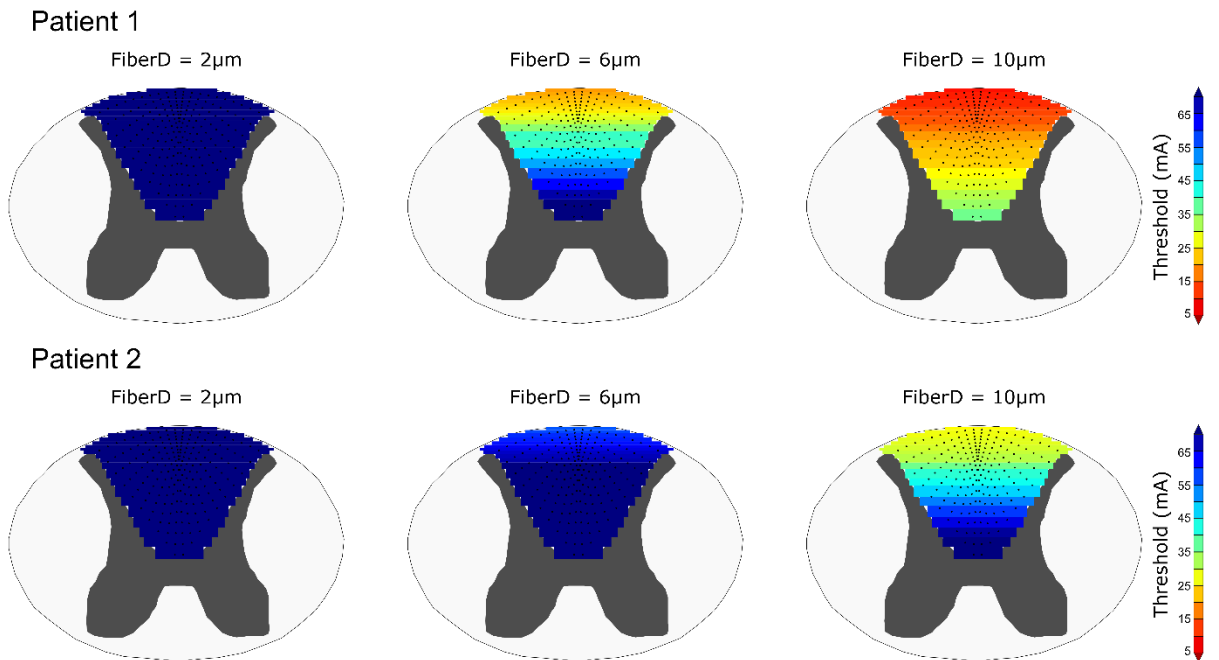
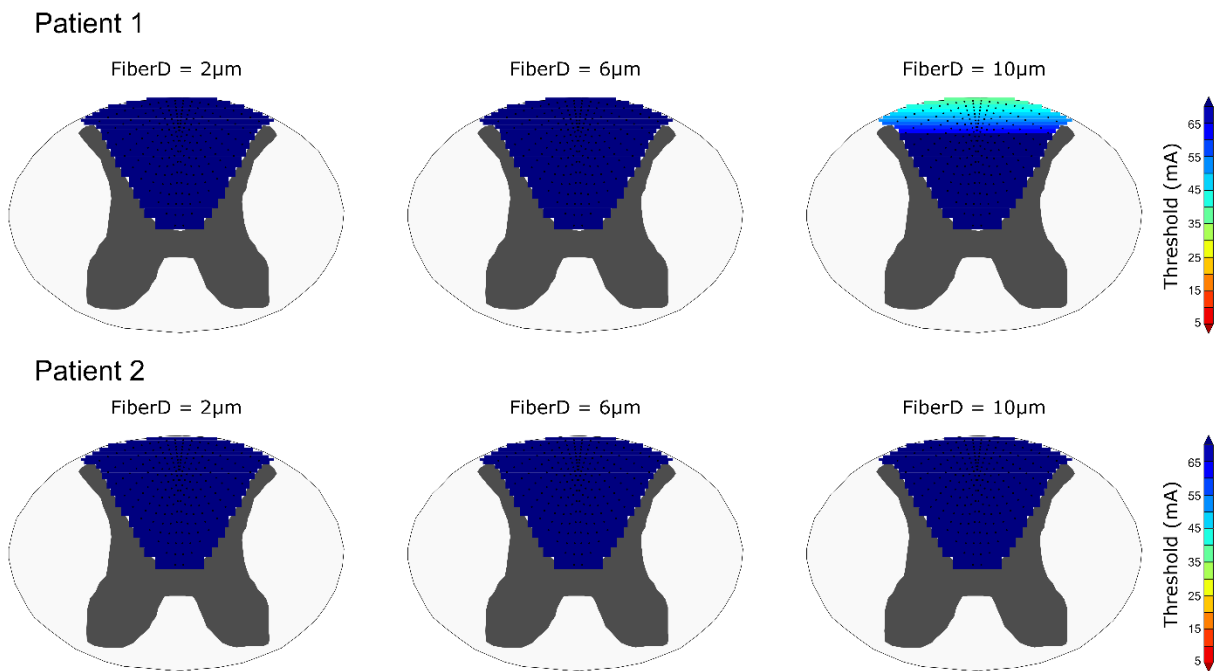


Figure 5.9. Activation thresholds for two patients using conventional SCS.



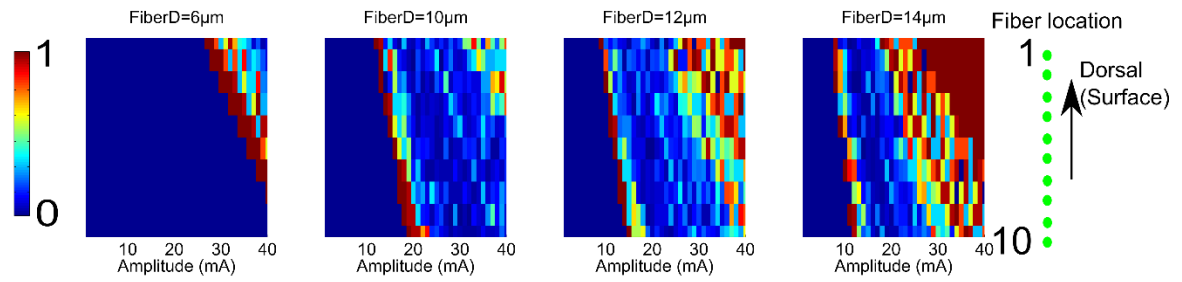
**Figure 5.10. Activation thresholds for two patients using KHF-SCS.**



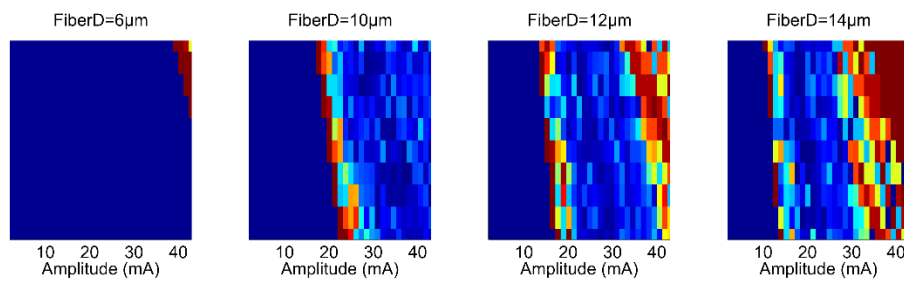
**Figure 5.11. Block thresholds for two patients using KHF-SCS.**

The firing activity of model nerve fibers that were activated by the KHF-SCS signal was asynchronous to the stimulation signal and to other activated fibers, as indicated by the vector strength (Figure 5.12), and by the metrics of dissimilarity between pairs of spike trains (Figure 5.13), respectively. We plotted the vector strength as a function of stimulus amplitude for the 10 most superficial fibers for model geometries from three different patients (Figure 5.12). The blue areas, *i.e.*,  $r=0$ , for the lower amplitude stimuli correspond to sub-threshold regions where no activity was generated. As the stimulus amplitude was increased the vector strength increased sharply to values of 1, as illustrated by the dark red “borders” in the color plots, and for deeper fibers this peak was shifted toward higher amplitudes. As the amplitude was increased further,  $r$  decreased to close to zero and there was a range of amplitudes for which  $r$  remained small. Finally,  $r$  increased to 1 for very high amplitudes. The vector strength for fibers that fired at least 1 action potential indicated a low degree of synchronization to the KHF-SCS signal over the intermediate range of amplitudes. Similarly, the metrics of similarity between pairs of spike trains revealed that the activation patterns of fibers that were further separated in space were more dissimilar than fibers that were closer to one another (Figure 5.13).

Pat. 1



Pat. 3



Pat. 4

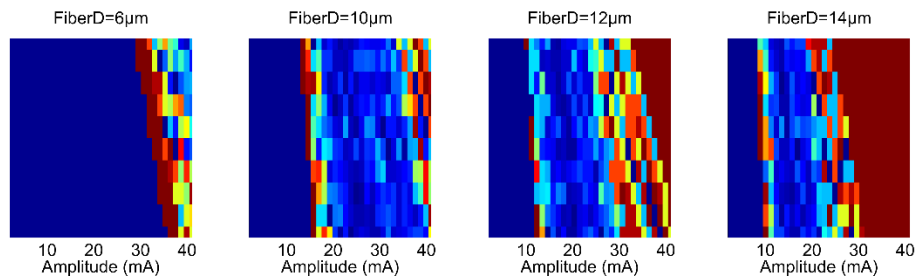


**Figure 5.12. Vector strength of DC fiber activity.**

Vector strength as a function of signal amplitude for 3 patients and 4 fiber diameters. Fiber activity was quantified at 10 different locations.

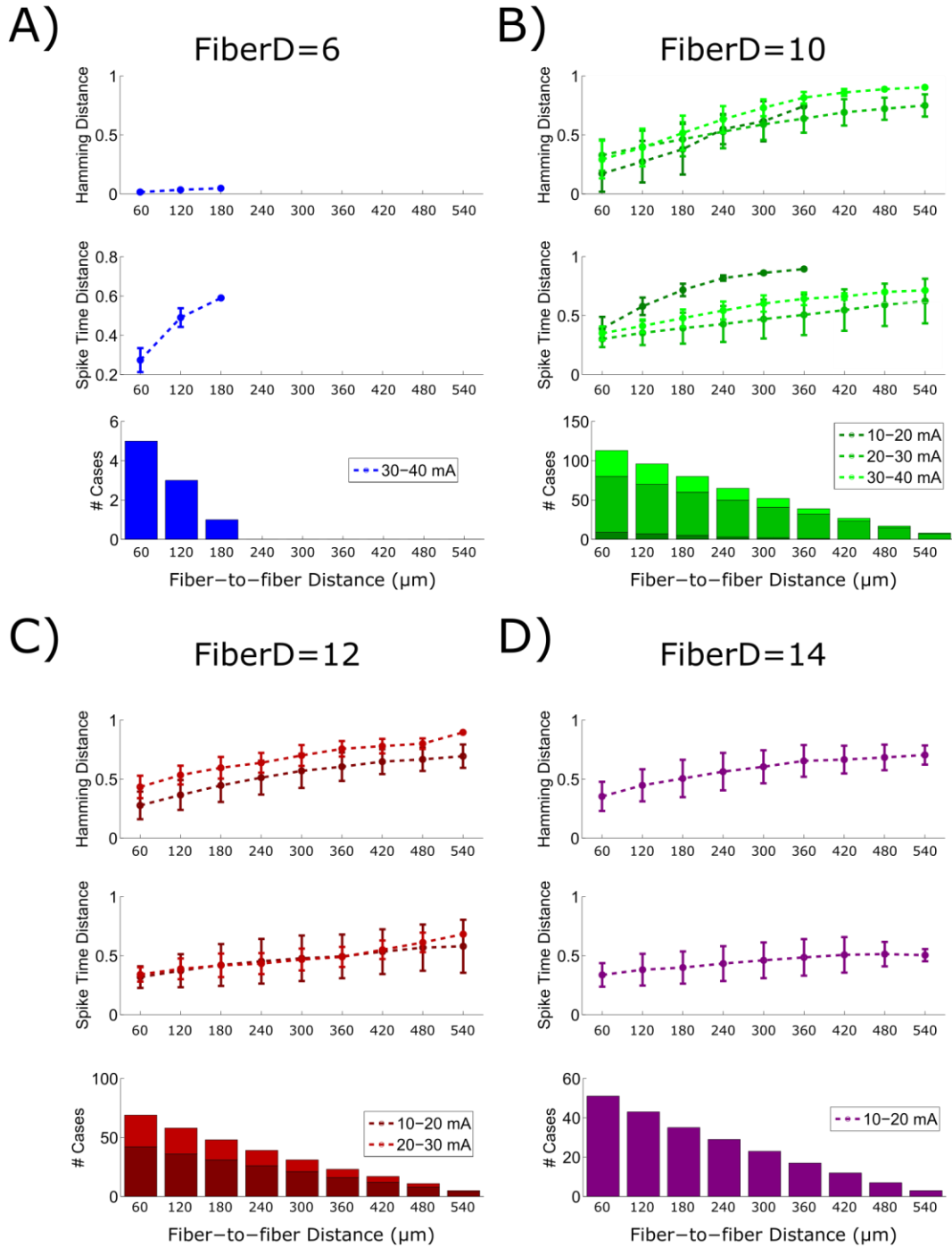


**Figure 5.13. Similarity of spike activity of DC fibers.**

Spike time distance and Hamming distance between pairs of spike trains as a function of fiber-to-fiber distance for 4 fiber diameters A) 6  $\mu\text{m}$ , B) 10  $\mu\text{m}$ , C) 12  $\mu\text{m}$ , and D) 14  $\mu\text{m}$ . The histograms show the number of pairs for which the metric was calculated in each case.

## 5.5 Discussion

We developed a double cable model of a dorsal column (DC) fiber, validated the model using experimental data measured *in vivo*, and quantified model nerve fiber responses to kilohertz-frequency (KHF) spinal cord stimulation (SCS). The thresholds for activation and block were above the clinical range (0.5 – 5 mA), and for the few fibers that exhibited persistent activation, the firing activity was asynchronous to the stimulation signal and to the activity of other activated fibers.

### 5.5.1 The strength-duration relationship

The chronaxies of the DC fiber models matched the chronaxies recorded experimentally more closely than did the MRG model (Figure 5.6). The improvement over the MRG model can be explained by differences in passive membrane properties, as the chronaxie depends on electrotonic time constant [222]. For example, halving the membrane capacitance reduced chronaxie by 16% in a myelinated fiber model [222], and increasing myelin conductance slightly increased rheobase and reduced chronaxie in a different model [230]. In our model the membrane capacitance at dc was 1  $\mu\text{F}/\text{cm}^2$ , a value that has been measured throughout the nervous system [210], whereas in the MRG model the membrane capacitance was 2  $\mu\text{F}/\text{cm}^2$ . Further, we used a myelin conductance per lamella of 2  $\text{mS}/\text{cm}^2$ , twice the value used in the MRG. These two changes reduced chronaxies by 10% in our model. In addition, stimulation modality can affect chronaxie measurements [222, 223], and, for example, faster chronaxies are recorded for tripolar stimulation as compared to monopolar stimulation [222]. Initially, we simulated monopolar stimulation and obtained chronaxies that were ~5% longer than for bipolar stimulation for all fiber models. We also calculated chronaxies for two other mammalian nerve fiber models, and obtained chronaxies well below (Sweeney model) or above (Wesselink model) the experimental measurements.

Our measurements of the SD relationship were within the range of the SD recorded in cat DC fibers [217], even though the fibers differed in diameter and species. In humans, chronaxies were estimated using perception and discomfort thresholds as  $109 \pm 12 \mu\text{s}$  [231]. In these measurements, chronaxies likely captured the excitation properties of a group of DC fibers of different sizes. Other fibers in the CNS and PNS have slower chronaxies. For example, cat myelinated bulbospinal fibers with conduction velocities in the 16-63 m/s range had chronaxies of  $180 \pm 60 \mu\text{s}$  [232], and chronaxies of single motor units of the human median nerve averaged  $463 \pm 52 \mu\text{s}$ , well above spinal axons [85].

### 5.5.2 The recovery cycle

Our model matched quite well our experimental measurements of recovery cycle (RC), and the threshold variations predicted by the model were within the 95% confidence intervals of the experimental recordings (Figure 5.7). The RC is affected by both passive electrical properties and active mechanisms of the fiber [86]. In early versions of the model, we quantified the impact of several model parameters on the RC, and we used this analysis for coarse parameter tuning. In particular, we observed that reducing the fast potassium conductance produced an RC that matched better the supranormal period of the RCs that we recorded *in vivo*.

We quantified the impact of both the conductance of the paranodal axolemma and the resistance of the paranodal seal on the RC, since the variations in membrane voltage following an action potential are mediated by passive charging of the internodal axolemma and subsequent discharging through or under the myelin [233]. Increasing the resistance of the paranodal axolemma or the paranodal seal had a similar net effect: more pronounced supernormal and subnormal periods, and the effect was more marked for the paranodal seal resistance. The paranodal seal resistance had a greater impact on the supernormal period, *i.e.*, reduced threshold

for short inter-pulse interval, but the subnormal period became disproportionately accentuated, in particular for the 2  $\mu\text{m}$  fiber.

We also quantified the impact of modifying the maximum conductances of the fast potassium, persistent sodium and slow potassium channels (Figure 5.14). In early versions of the model we also quantified the impact of incorporating the resurgent  $\text{Na}^+$  current, but we observed no effect on the RC and other tests. Since there is no evidence of the resurgent  $\text{Na}^+$  current in DC fibers, we did not further explore this ion current. The fast potassium current,  $I_{Kf}$ , may affect the supernormal period because it hyperpolarizes the axon with fast dynamics. Reducing the maximum conductance of  $I_{Kf}$  by 40% reduced the thresholds in the supernormal period by no more than 5%, and eliminating  $I_{Kf}$  produced marked threshold reductions (Figure 5.14A). For the default model, as we increased the fiber diameter the RC shifted downwards, but for the model with no  $I_{Kf}$  the opposite occurred for short IPIs. In early versions of the model we used a maximum fast potassium conductance of 0.02 S/cm<sup>2</sup> [86], and in our final version we reduced it to 0.002 S/cm<sup>2</sup> to match better the supranormal period of the experimental data.

The persistent sodium current,  $I_{Nap}$ , has been implicated in the origin of the afterpotentials [86], and therefore it can affect the RC.  $I_{Nap}$  returns to its baseline after about 25 ms the action potential occurred, and consequently, it affected only the 2 – 25 ms IPI range of the RC (Figure 5.14B). Increasing the maximum conductance of  $I_{Nap}$  by 40% increased the supernormal period by 5%. Although this current has not been directly measured in the dorsal columns, it is well documented in both sensory and motor PNS fibers [103]. Our default maximum  $I_{Nap}$  conductance was 0.01 S/cm<sup>2</sup>, but other models have used higher values [103].

Finally, the slow potassium current,  $I_{Ks}$ , affected the RC for all IPIs (Figure 5.14C). Consistent with its role in the origin of the afterhyperpolarization several tens of ms after an action potential [86],  $I_{Ks}$  affected the subnormal period as well. In the node of Ranvier of DC

fibers, potassium currents are much smaller than sodium currents [196], and accordingly, the maximum fast sodium conductance was about 30 times larger than the slow potassium conductance in the default model version.

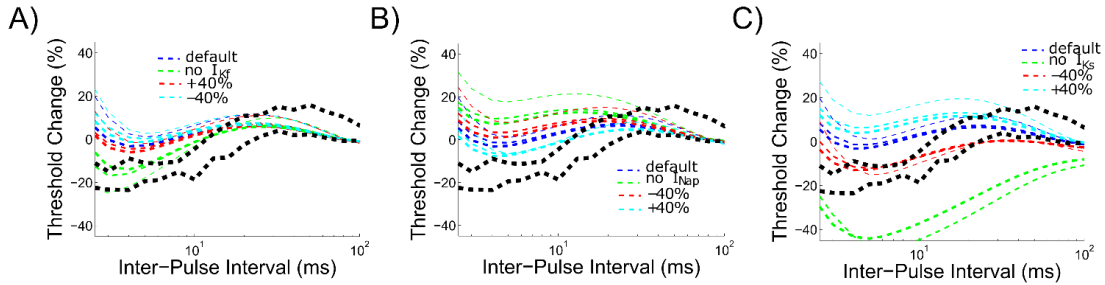


**Figure 5.14. Effects of ion currents on the recovery cycle of the fiber model.**

A) Fast potassium current,  $I_{Kf}$ , B) persistent sodium current,  $I_{Nap}$ , and C) slow potassium current,  $I_{Ks}$ . Fiber diameter: 2, 4 and 6  $\mu\text{m}$  (thicker line represents bigger fiber). Black dashed lines: 95% confidence intervals of experimental measurements.

### 5.5.3 Effects of extracellular potassium concentration

The dynamics of extracellular  $\text{K}^+$  concentration were necessary to match the profiles of firing rates recorded in DC fibers *in vivo* (Figure 5.8). Our approach to model  $\text{K}^+$  diffusion differed from others [214, 234] in that we let the ion accumulate not only in the submyelin space and the immediate vicinity of the node but also in the extracellular bath. This approach better represents experimental setups in which  $\text{K}^+$  concentration was recorded by placing a glass electrode in the extracellular medium. For example, the extracellular  $\text{K}^+$  concentration was measured in the alveolar section of an *in vitro* preparation of the rat hippocampus [105], and it is unlikely that these recordings captured the variations in submyelin  $\text{K}^+$  that have been postulated to affect axonal conduction [214] or that they sampled exclusively the  $\text{K}^+$  concentration in the perinodal region. In a model of a subthalamic nucleus axon with  $\text{K}^+$  dynamics,  $\text{K}^+$  concentration increased about four times in the submyelin space of the juxtaparanode in an activity-dependent manner, and the AP amplitude decayed as time progressed. It was hypothesized that this effect would produce “functional block” since small APs would not be able to release neurotransmitter,

thereby blocking the transmission of information [214]. In our model, we also observed a decay of the amplitude of the action potentials and functional block, but  $K^+$  accumulated in the extracellular space in addition to the juxtaparanodal submyelin space, where concentration changes were more modest ( $<1$  mM). In contrast, the concentration in the extracellular space increased up to  $>10$  mM in some cases, and depolarization block was often observed for high extracellular concentration increases. Thus, the main contributor to the effects of  $K^+$  concentration was extracellular  $K^+$ . In a different fiber model, the electrical properties of myelin were dependent on  $K^+$  concentration to account for Schwann cell swelling due to  $K^+$  accumulation [234]. In this model, increasing submyelin  $K^+$  reduced the resistance of the myelin, and bursting patterns of activity were recorded for a number of stimulation frequencies in the range of hundreds of Hz. Again, the observed effects were attributed to  $K^+$  accumulation in the juxtaparanode, and  $K^+$  accumulation in the extracellular space was not modeled. Our results indicate that  $K^+$  concentration dynamics may be an important feature to reproduce the responses of DC fibers to KHF signals. Incorporating  $K^+$  diffusion generated time-decaying firing rate in some cases, using either very low node density with slow time constant, or high density with fast time constant, and both cases favored  $K^+$  accumulation in the extracellular space.

#### **5.5.4 Implications for spinal cord stimulation**

In agreement with another recent model of KHF-SCS [235], our results suggest that KHF-SCS may act through mechanisms other than conduction block because the amplitudes required to achieve conduction were well above the range of amplitudes used clinically. Lempka *et al.* used a finite element model of human SCS and the MRG model to calculate activation and block thresholds for DC and dorsal root fibers using traditional SCS and KHF-SCS. Their model showed that only large DC fibers of  $15\ \mu\text{m}$  diameter were activated by the KHF-SCS signal using amplitudes less than  $5\ \text{mA}$ , *i.e.*, within the range used clinically. Further, the amplitude to activate

smaller fibers increased sharply, and thresholds for 7.3  $\mu\text{m}$  fibers at the superficial edge of the DCs were higher than 10 mA. In addition, the minimum block thresholds were about twice as high as the minimum activation thresholds, and block thresholds were less than 5 mA only for a very thin dorsal cerebrospinal fluid (CSF) layer of 2 mm and for the most superficial fibers. The thresholds for our fibers were greater, and up to one order of magnitude in the case of block thresholds, than those reported by Lempka *et al.* for two reasons. First, we used smaller fiber diameters, *i.e.*, 2 – 10  $\mu\text{m}$  versus 7.3 – 15  $\mu\text{m}$ , and larger diameter fibers have lower thresholds for both activation and block [32]. In humans, the vast majority of DC fibers are  $\sim$  2-3  $\mu\text{m}$  in diameter, and the largest fibers are about 10-11  $\mu\text{m}$  [20]. We selected appropriate diameters to represent human DCs. Secondly, thresholds increase with increasing distance to the electrode. In our volume conductor model the distance from the electrode to the DCs, *i.e.*, the dorsal CSF thickness, varied between 3.5 and 6 mm, and in Lempka *et al.* the CSF thickness ranged from 2 to 4.4 mm. Regardless of the differences in absolute thresholds, both studies showed block thresholds well above the clinical range, while activation threshold were toward the high end of this range. Thus, it appears that only few large, superficial fibers are activated during KHF-SCS. Similarly, it has been postulated that DC fiber recruitment during traditional SCS is restricted to diameters  $>$  10  $\mu\text{m}$  within the outermost 0.25 mm layer of the DC [21]. In traditional SCS, the pulse duration is typically longer ( $\sim$  300  $\mu\text{s}$ ), thresholds are consequently lower [235], and amplitudes are higher (1 – 20 mA). Therefore, the recruitment hypothesis for traditional SCS may represent an ‘upper bound’ for KHF-SCS, *i.e.*, fewer and larger fibers would be activated in this case.

In contrast to traditional SCS, KFHSCS relieves pain without paresthesia [6, 9]. A possible explanation for the absence of paresthesia is asynchronous activation of fibers. In peripheral neuroprostheses for amputees, periodic patterns of stimulation applied to sensory fibers

generated paresthesia, whereas pulse-duration modulated patterns were perceived as a more natural sensation [236]. The modulated pattern may have produced less synchronous activity in the fiber population because each pulse activated a different number of fibers. A similarly patterned waveform relieved pain via SCS in a small group of patients who also reported a more comfortable sensation than traditional SCS [17]. A computational model suggested that the modulated waveform triggered burst firing of DC fibers, with the intra-burst activity varying from fiber to fiber, whereas traditional SCS evoked synchronous rhythmic firing across the population of activated fibers. Similar to the pulse-duration modulated waveform, our results showed that the KHF-SCS signal produced asynchronous activation of fibers, without any rhythmicity or synchronization. However, if KHF-SCS acts through asynchronous activation of few large, superficial fibers, it is yet to be determined how this activity affects the circuits involved in pain processing and perception.

## **5.6 Conclusion**

We implemented a model of a dorsal column (DC) fiber that we validated using experimental data. The model was used to calculate the responses of DC fibers to spinal cord stimulation (SCS), and the model incorporated features that make it suitable for simulations using kilohertz-frequency (KHF) signals, including frequency-dependent membrane capacitance and a dynamic representation of activity-dependent extracellular potassium concentration. In our simulations using a model of human SCS, the activity of DC fibers was not synchronized to the KHF-SCS signal, the activity of activated fibers was poorly correlated with activity in other fibers. Thus, if KHF-SCS for pain relief acts through activation of large, superficial fibers, then the firing activity is likely to be asynchronous.

## Chapter 6: Conclusions and Future Directions

### 6.1 Conclusions

The goal of this dissertation was to analyze quantitatively electrical stimulation of nerve fibers using kilohertz-frequency (KHF) signals. The outcomes of this work contribute to the understanding of KHF neurostimulation by establishing the importance of the tissue filtering properties on the distribution of potentials, assessing quantitatively the impact of KHF stimulation on nerve fiber excitation, and developing and validating a detailed model of a dorsal column (DC) fiber to characterize the effects of KHF stimulation on DC axons.

Tissues exhibit dispersion, *i.e.*, the conductivity and the permittivity of tissues depend on the stimulation frequency. The conductivity of the skin, for instance, increases several orders of magnitude from dc to 100 kHz, and this property was exploited in clinical applications of transcutaneous electrical stimulation (TES) to reach deep nerve fibers from surface electrodes. Our mathematical model of TES showed that KHF signals indeed generate larger potentials at depth than lower frequencies. However, incorporating KHF signals in the stimulation waveform failed to facilitate fiber excitation. Specifically, we demonstrated in models and with *in vivo* experiments that an amplitude-modulated signal with KHF carrier (210 kHz) and non-zero offset, called TAMS, generate the same nerve activation as a conventional rectangular pulse. In our model of TES, nerve fiber threshold varied non-monotonically with the carrier frequency, and for carriers  $> 100$  kHz, thresholds were identical to those obtained using rectangular pulses. In addition, prior work speculated that TAMS was optimal for TES because it bypassed more superficial sensory fibers, but our model showed that TAMS and rectangular pulses activated superficial fibers in addition to the deeper, target nerve fibers. Our *in vivo* measurements provided additional conclusive evidence that the carrier of TAMS did not contribute to nerve excitation. In

rat and cat sciatic nerves, TAMS with carriers of 20 kHz or greater generated the same nerve activation as a rectangular pulse, even after increasing the amplitude of the carrier. Therefore, the addition of KHF carriers ( $> 20$  kHz) to the stimulation signal did not improve efficacy or efficiency in peripheral nerve stimulation.

We implemented a model of a DC fiber that we validated using experimental data, and we used the model to calculate the responses of DC fibers to spinal cord stimulation (SCS) – a well-established treatment for chronic pain conditions – using a 10 kHz biphasic pulse waveform. Our simulations indicated that the thresholds for activation and block of DC fibers were above the amplitudes used clinically. Further, the activity of stimulated DC fibers was not synchronized to the KHF-SCS signal and was poorly correlated with activity in other stimulated DC fibers. KHF-SCS for pain relief acts through activation of few, large, superficial fibers, and the firing activity of stimulated DC fibers is likely to be asynchronous.

## **6.2 Future directions**

The work presented here advanced our understanding of KHF neurostimulation, and our findings are relevant in particular for TES and SCS. However, there remain opportunities for further investigating many aspects of TES and SCS, and our models of TES and DC fiber may be used to examine other applications of KHF stimulation as well.

### **6.2.1 Kiloherertz-frequency transcutaneous electrical stimulation**

Our volume conductor model of TES presented in Chapter 2 may be used to determine the spatiotemporal distribution of currents and potentials for waveforms other than TAMS that contain KHF components, as well. Next, coupled to models of nerve fibers, it can be used to estimate fiber thresholds, in a similar manner to our study of the TAMS waveform. For example, in interferential current (IFC) therapy, it is intended that two current paths produce an interference effect where they intersect, but the actual stimulation signal experienced by the fibers

is not known, and the degree of modulation depends on fiber location and orientation with respect to the skin electrodes. Future work can determine the distribution of currents in IFC, and our model may be used for this task. Then, thresholds for motor and sensory fibers placed in the volume conductor at different distances from the electrode may be used as proxies for force output and discomfort threshold, respectively. It may be possible that some fibers are blocked and others activated, depending on the degree of modulation of the stimulation signal, as unmodulated sinusoids can block the conduction of action potentials [33]. Further, a model-based approach can be used to determine the sets of stimulation parameters that maximize force output or minimize discomfort level. These outcomes are affected differently by different stimulation parameters [24], and future research should be directed to determine the basis of these differences.

### **6.2.2 Kilohertz-frequency spinal cord stimulation**

A biophysical network model of the dorsal horn including wide-dynamic range (WDR) projection neurons was proposed to study the mechanism(s) underlying SCS [237]. The firing activity of WDR neurons was used as a proxy for pain relief, and SCS (<150 Hz) provided input to the model by means of DC fiber activation represented as constant-frequency spike trains. The DC fiber model presented in Chapter 5 can be coupled to this network model to determine the responses of WDR neurons to KHF-SCS. In this case, the firing activity of model DC fibers evoked by the KHF-SCS signal would be the input to the network model. One possibility is that KHF-SCS inhibits WDR neuron activity similar to traditional SCS, and in this case it is hypothesized that both SCS modalities share similar spinal mechanisms. However, it is also possible that KHF-SCS relieves pain through different mechanisms, and thus the KHF-SCS signal may not reduce WDR neuron activity. Either way, our model suggested that KHF-SCS only activates few, large, superficial DC fibers for the amplitude ranges used clinically, and

therefore it is necessary to select carefully the inputs to the spinal network that represent the fiber recruitment characteristics in KHF-SCS.

In addition, our DC fiber model may be used to determine the effects of SCS on the activity of dorsal column nuclei (DCN) – relay centers involved in the processing of tactile information – to investigate the basis of SCS-evoked tactile percepts. Specifically, the firing patterns of model DC fibers in response to SCS may be used as inputs to DCN models [238]. Traditional SCS evokes a tingling sensation known as paresthesia, whereas KHF-SCS evokes no paresthesia [9]. Other non-tonic patterns of SCS produce more comfortable and natural percepts than paresthesia [17]. Our DC fiber model coupled to a model of DCN may help determine the neural basis of the differences in the percepts evoked by the different SCS modalities. These differences may be related to the rhythmic versus asynchronous activation patterns generated by traditional SCS and KHF-SCS, respectively.

### **6.2.3 Neural responses to kilohertz-frequency signals**

The responses of axons and other cells to KHF signals can vary significantly and can be classified in two broad categories, activation and block. Therefore, axonal output measures other than activation thresholds, such as firing rate and block thresholds, may be relevant for KHF stimulation. For single pulses, the quasi-static assumption that is commonly used in neural stimulation modeling introduces errors in the calculation of the potentials that are time-dependent and reach a maximum at the edges of the pulse [122]. Therefore, during repetitive stimulation the error may vary depending on the pulse rate. Future research should quantify the error resulting from using the quasi-static solution on the firing rate and the block thresholds in response to KHF stimulation.

Finally, in Chapter 5 we showed that including a model of the dynamics of extracellular potassium concentration was necessary to match the time-decaying firing activity of DC fibers

recorded *in vivo*. Similar activation patterns were recorded from peripheral motor and sensory fibers *in vivo* [76, 77], and it may be possible that extracellular potassium accumulation was involved in the response to the KHF signal there, as well. This hypothesis could be tested by incorporating our model of potassium diffusion in a model of a peripheral nerve fiber, *e.g.*, the MRG model [86], using appropriate fiber diameters. However, in our formulation we adjusted some parameters according to measurements of potassium accumulation in the central nervous system. Activity-dependent potassium dynamics may differ in the peripheral nervous system, and therefore the model of potassium diffusion should be updated accordingly to reflect these differences.

## Appendix A: Volume Conductor Model of Transcutaneous Electrical Stimulation – Coefficients of Fourier Method

The coefficients of Equation (2.3) were:

-Voltage-controlled stimulation

$$B_{skin} = \frac{V_{source} \cdot Y_{interface} + A_{skin} (\alpha_{skin} \cdot k_y - Y_{interface})}{Y_{interface} + \alpha_{skin} \cdot k_y}$$

$$A_{skin} = \frac{V_{source} + (Y_{interface} + \alpha_{skin} \cdot k_y)(X \cosh(k_y \cdot h) - Z \sinh(k_y \cdot h)) - V_{source} \cosh(k_y \cdot h)}{2(Y_{interface} \sinh(k_y \cdot h) + \alpha_{skin} k_y \cosh(k_y \cdot h))}$$

$$B_{fat} = X - A_{fat}$$

$$A_{fat} = \frac{(\alpha_{fat} \cdot k_y - \alpha_{muscle} \cdot k_{ya}) \exp(-k_{ya}(h+d)) B_{muscle}}{2\alpha_{fat} k_y \exp(k_y(h+d))}$$

$$B_{muscle} = \frac{X \cosh(k_y(h+d)) - Z \sinh(k_y(h+d))}{\exp(-k_{ya}(h+d))}$$

$$A_{muscle} = 0$$

where

$$X = \frac{-\alpha_s \cdot Y_{interface} \cdot V_{source}}{\sinh^2(k_y h)(\alpha_{fat} Y_{interface} + \alpha_{skin}^2 k_y Z) - \cosh^2(k_y h)(\alpha_{skin} \alpha_{fat} k_y Z + \alpha_{skin} Y_{interface}) + \sinh(k_y h) \cosh(k_y h)(\alpha_{skin} \alpha_{fat} k_y + (\alpha_{skin} - \alpha_{fat}) Z Y_{interface} - \alpha_{skin}^2 k_y)}$$

$$Z = \frac{\alpha_{fat} k_y \tanh(k_y(h+d)) + \alpha_{muscle} k_{ya}}{\alpha_{muscle} k_{ya} \tanh(k_y(h+d)) + \alpha_{fat} k_y}$$

$Y_{interface}$ : admittance of the electrode-skin interface;  $\alpha = \sigma + j\omega\epsilon$ .

-Current-controlled stimulation

$$B_{skin} = \frac{I_{source}}{\alpha_{skin} \cdot k_y + A_{skin}}$$

$$A_{skin} = \frac{I_{source}}{2(\alpha_{skin} \cdot k_y)} (\tanh(k_y h) - 1)W(1 - Z \tanh(k_y h))$$

$$B_{fat} = W - A_{fat}$$

$$A_{fat} = \frac{(\alpha_{fat} \cdot k_y - \alpha_{muscle} \cdot k_{ya}) \exp((-k_{ya} + k_y)(h + d)) B_{muscle}}{2\alpha_{fat} k_y}$$

$$B_{muscle} = \frac{W \cosh(k_y(h + d)) - Z \sinh(k_y(h + d))}{\exp(-k_{ya}(h + d))}$$

$$A_{muscle} = 0$$

where

$$W = \frac{I_{source}}{k_y(\alpha_{fat} Z + (\alpha_{skin} - \alpha_{fat}) \sinh(2k_y h) / 2 + (\alpha_{fat} - \alpha_{skin}) Z \sinh^2(k_y h))}$$

## Appendix B: Model of Dorsal Column Fiber – Ion Channel Kinetics

The kinetics of fast and persistent sodium, and slow potassium channels, were taken from [86]. We incorporated fast potassium channels in the juxtaparanode of the fiber model. We used a Hodgkin-Huxley formulation so that the kinetics are described by:

$$\frac{dn}{dt} = \alpha_n(1-n) - \beta_n n$$

Where  $n$  is the gate variable. The voltage-dependent parameters,  $\alpha_n$  and  $\beta_n$ , were calculated using the following expressions as in Howells *et al.* (2012):

$$\alpha_n = 0.0221(V_m + 90.8)/(1 - \exp(-90.8 - V_m)/7.7)$$

$$\beta_n = 0.0393(-73.6 - V_m)/(1 - \exp(V_m + 73.6)/7.35)$$

Next, the fast potassium current,  $I_{K,fast}$ , was calculated by:

$$I_{K,fast} = G_{K,fast} n^4 (E - E_K)$$

Where the default value of  $G_{K,fast}$  was 20.7 mS/cm<sup>2</sup>.

We incorporated HCN channels in the internodal sections of our DC fiber model. We used a Hodgkin-Huxley formulation so that the kinetics are described by:

$$\frac{dq}{dt} = \alpha_q(1-q) - \beta_q q$$

Where  $q$  is the gate variable. The voltage-dependent parameters,  $\alpha_q$  and  $\beta_q$ , were calculated using the following expressions as in Howells *et al.* (2012):

$$\alpha_q = 0.00522 \exp(-(V_m + 94.2)/12.2)$$

$$\beta_q = 0.00522 / \exp(-(V_m + 94.2)/12.2)$$

Next,  $I_h$  was calculated by:

$$I_h = G_h q (E - E_q)$$

Where  $G_q = 0.025 \text{ mS/cm}^2$  and  $E_q = -52.7 \text{ mV}$ .

## Appendix C: Simplified Model of Spinal Cord Stimulation

We implemented a simplified model of SCS using two point-source electrodes that delivered bipolar stimulation in an anisotropic medium (Figure C.1). We placed model fibers parallel to the line connecting the electrodes at distances ranging from 0.1 to 1 mm from this line. The conductivity of the medium was 1/3 S/m in the longitudinal direction, *i.e.*, parallel to the fibers, and 1/12 S/m in the transverse direction, *i.e.*, perpendicular to the fibers. We applied the KHFSCS signal at frequencies of 1 and 10 kHz, and the simulation time was 20 s. To model the intrinsic activity of the fiber or that generated by test pulses applied by a different electrode, we applied intracellular current pulses to one end of the fiber and recorded the activity at the other end. The intracellular pulses were delivered at 3 Hz, and the KHFSCS signal started after 1 s of simulation.

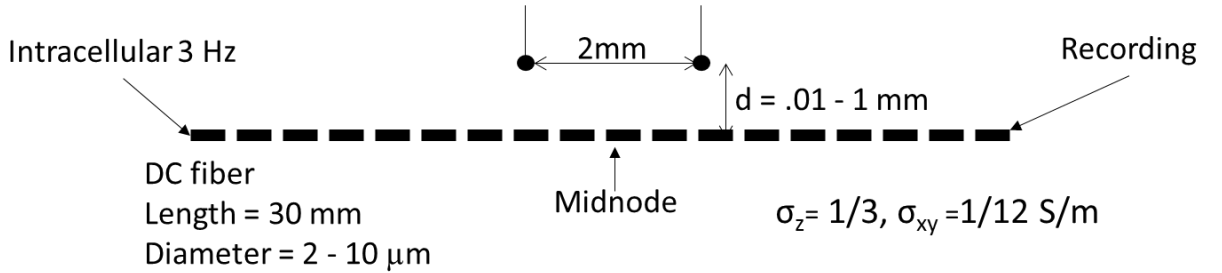


**Figure C.1. Simplified model of spinal cord stimulation.**

Bipolar stimulation delivered the KHFSCS signal. Intracellular pulses at one end generated “intrinsic activity” at 3 Hz. Fiber activity was recorded at the other end.

The potentials at position  $(x,y,z)$  in space were calculated using the equation:

$$\Phi(x, y, z) = \frac{I_s}{4\pi\sqrt{\sigma_{xy}\sigma_z((x-x_1)^2 + (y-y_1)^2) + \sigma_{xy}^2(z-z_1)^2}} - \frac{I_s}{4\pi\sqrt{\sigma_{xy}\sigma_z((x-x_2)^2 + (y-y_2)^2) + \sigma_{xy}^2(z-z_2)^2}}$$

Where  $I_s$  is the stimulation signal,  $x_i, y_i, z_i$  ( $i=1,2$ ) are the coordinates of the electrodes,  $\sigma_z$  is the conductivity in the longitudinal direction, and  $\sigma_{xy}$  is the conductivity in the transverse direction.

Figure C.2 shows the raster plots of the activity of a 2  $\mu\text{m}$  fiber in response to the 10 kHz KHFS signal for three different electrode-to-fiber distances. The red lines represent action potentials (APs) evoked by the KHFS signal, and the blue lines correspond to APs evoked by the intracellular test electrode. The pattern of activations were heterogeneous and very sensitive to the amplitude of stimulation. For the electrode-to-fiber distance of 0.1 mm, all applied amplitudes blocked the conduction of APs evoked by the test pulses. For the electrode-to-fiber distance of 0.5 mm, amplitudes smaller than 0.6 mA had no effect on the transmission of activity evoked by test pulses, amplitudes between 0.8 and 1.2 mA generated persistent activation, and higher amplitudes blocked the conduction of test APs. However, very high amplitudes  $> 6$  mA generated persistent activity. In sum, as we increased the amplitude, the fiber response transitioned from transmission of APs to fiber activation to conduction block to fiber activation. Finally, for the electrode-to-fiber distance of 1 mm, the transmission of action potentials was largely unaffected, and no block was observed in the simulated amplitude range.

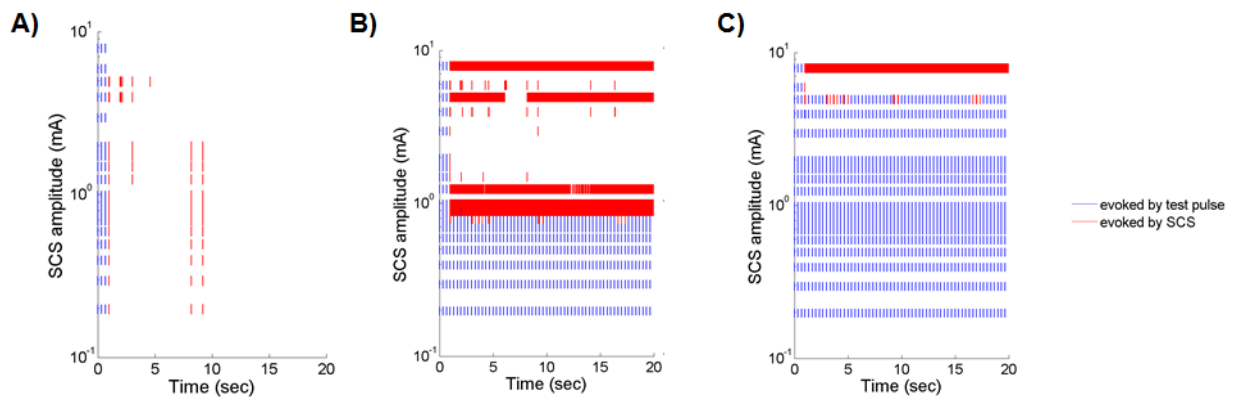


**Figure C.2. Raster plots for a 2  $\mu\text{m}$  fiber placed at three different distances from the electrode: A) 0.1 mm, B) 0.5 mm, and C) 1 mm.**

In addition, we applied a 1 kHz KHFS signal. Figure C.3 shows raster plots for selected electrode-to-axon distances using the 1 kHz signal. In general, the pattern of activation

was more homogeneous as compared to that observed using the 10 kHz signal. Further, we observed conduction block using the 1 kHz signal, but only for very high amplitudes at a certain electrode-to-fiber distance.

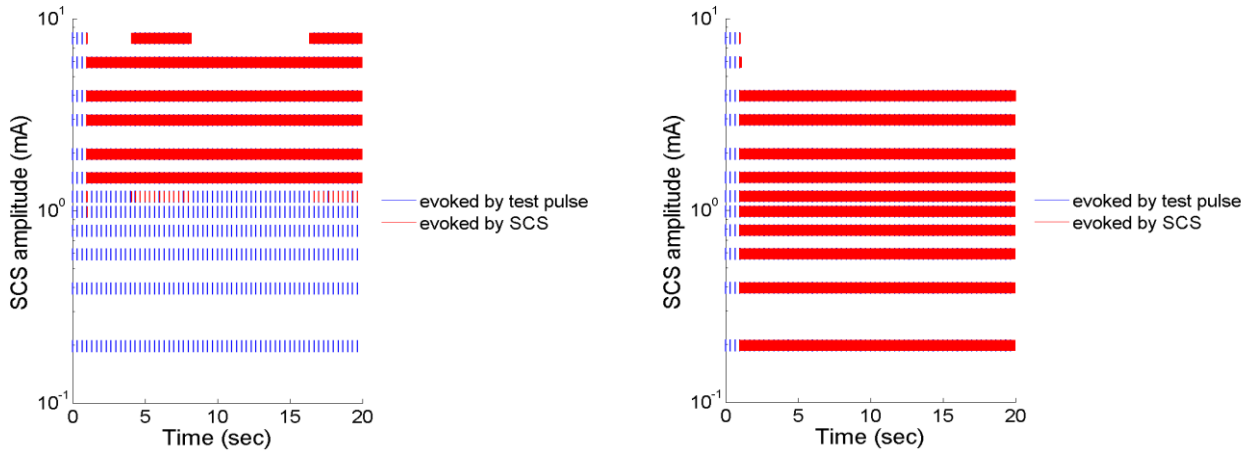


**Figure C.3. Raster plots for the 1 kHz signal as a function of signal amplitude. Electrode-to-axon distance: A) 0.2 mm, b) 0.6 mm. Fiber diameter: 2  $\mu\text{m}$ .**

To quantify the degree of synchronization of the firing activity to the KHFSCS signal, we used the vector strength. As shown in Figures C.4 and C.5, the vector strength was higher for the 1 kHz signal for a number of amplitude/distance pairs. This result is consistent with experimental recordings (Crosby et al., unpublished data), for which the vector strength was higher for the 1 kHz signal for all the amplitudes that were tested. However, the model results showed much higher vector strength than the experimental measurements.

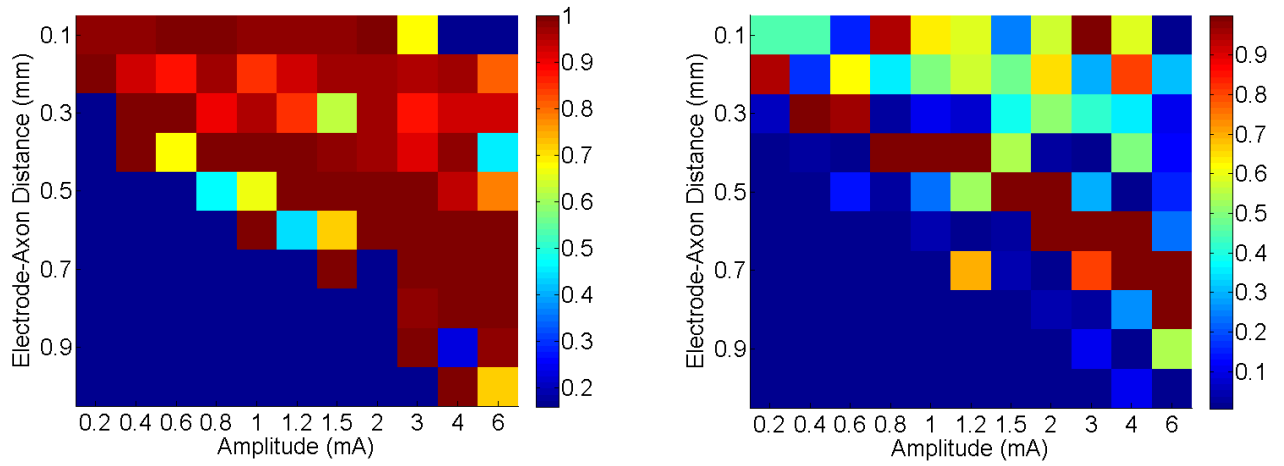


**Figure C.4.** Vector strength as a function of signal amplitude and electrode-to-axon distance for A) 1 kHz and B) 10 kHz. Fiber diameter: 2  $\mu\text{m}$ .

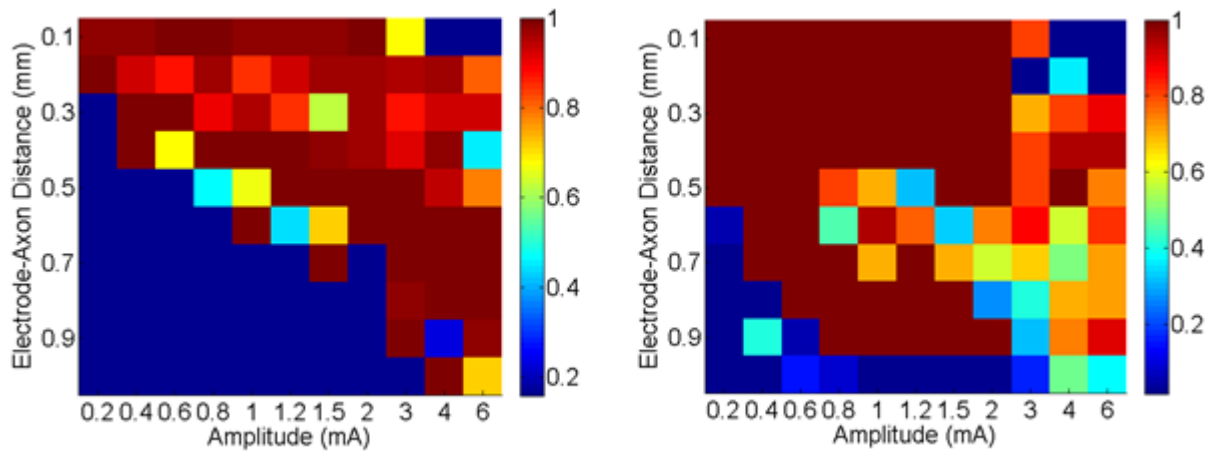


**Figure C.5.** Vector strength as a function of signal amplitude and electrode-to-axon distance for A) 1 kHz and B) 10 kHz. Fiber diameter: 6  $\mu\text{m}$ .

## References

1. Krames ES, Hunter Peckham P, Rezai A, Aboelsaad F: **What Is Neuromodulation?** In *Neuromodulation*. Edited by Krames ES, Hunter Peckham P, Rezai AR. Academic Press - Elsevier; 2009:3–8.
2. Howell B, Lad SP, Grill WM: **Evaluation of Intradural Stimulation Efficiency and Selectivity in a Computational Model of Spinal Cord Stimulation.** *PLoS One* 2014;1–25.
3. Dorval AD, Kuncel AM, Birdno MJ, Turner D a, Grill WM: **Deep brain stimulation alleviates parkinsonian bradykinesia by regularizing pallidal activity.** *J Neurophysiol* 2010, **104**:911–21.
4. Kumar K, Rizvi S: **Cost-effectiveness of spinal cord stimulation therapy in management of chronic pain.** *Pain Med* 2013, **14**:1631–49.
5. Alo K, Holsheimer J: **New trends in neuromodulation for the management of neuropathic pain.** *Neurosurgery* 2002, **50**:690–704.
6. Tiede J, Brown L, Gekht G, Vallejo R, Yearwood T, Morgan D: **Novel spinal cord stimulation parameters in patients with predominant back pain.** *Neuromodulation* 2013, **16**:370–375.
7. Al-Kaisy A, Van Buyten J-P, Smet I, Palmisani S, Pang D, Smith T: **Sustained effectiveness of 10 kHz high-frequency spinal cord stimulation for patients with chronic, low back pain: 24-month results of a prospective multicenter study.** *Pain Med* 2014, **15**:347–54.
8. Van Buyten J-P, Al-Kaisy A, Smet I, Palmisani S, Smith T: **High-frequency spinal cord stimulation for the treatment of chronic back pain patients: results of a prospective multicenter European clinical study.** *Neuromodulation* 2012, **16**:59–65; discussion 65–6.
9. Kapural L, Yu C, Doust MW, Gliner BE, Vallejo R, Todd Sitzman B, Amirdelfan K, Morgan DM, Brown LL, Yearwood TL, Bundschu R, Burton AW, Yang T, Benyamin R, Burgher AH: **Novel 10-kHz High-frequency Therapy (HF10 Therapy) Is Superior to Traditional Low-frequency Spinal Cord Stimulation for the Treatment of Chronic Back and Leg Pain.** *Anesthesiology* 2015, **123**:851–60.
10. Perruchoud C, Eldabe S, Batterham AM, Madzinga G, Brookes M, Durrer A, Rosato M, Bovet N, West S, Bovy M, Rutschmann B, Gulve A, Garner F, Buchser E: **Analgesic efficacy of high-frequency spinal cord stimulation: A randomized double-blind placebo-controlled study.** *Neuromodulation* 2013, **16**:363–369.
11. Sweet J, Badjatiya A, Tan D, Miller J: **Paresthesia-Free High-Density Spinal Cord Stimulation for Postlaminectomy Syndrome in a Prescreened Population: A Prospective Case Series.** *Neuromodulation Technol Neural Interface* 2015, **2015**:n/a–n/a.

12. Shechter R, Yang F, Xu Q, Cheong Y, He S, Sdrulla A, Carteret AF, Wacnik PW, Dong X, Meyer R a, Raja SN, Guan Y: **Conventional and kilohertz-frequency spinal cord stimulation produces intensity- and frequency-dependent inhibition of mechanical hypersensitivity in a rat model of neuropathic pain.** *Anesthesiology* 2013, **119**:422–32.
13. Cuellar JM, Alataris K, Walker A, Yeomans DC, Antognini JF: **Effect of high-frequency alternating current on spinal afferent nociceptive transmission.** *Neuromodulation* 2013, **16**:318–327.
14. Song Z, Viisanen H, Meyerson B a, Pertovaara A, Linderoth B: **Efficacy of kilohertz-frequency and conventional spinal cord stimulation in rat models of different pain conditions.** *Neuromodulation* 2014, **17**:226–34; discussion 234–5.
15. Qin C, Yang X, Wu M, Farber JP, Linderoth B, Foreman RD: **Modulation of neuronal activity in dorsal column nuclei by upper cervical spinal cord stimulation in rats.** *Neuroscience* 2009, **164**:770–776.
16. Witham CL, Baker SN: **Modulation and transmission of peripheral inputs in monkey cuneate and external cuneate nuclei.** *J Neurophysiol* 2011, **106**:2764–75.
17. Tan D, Tyler D, Sweet J, Miller J: **Intensity Modulation: A Novel Approach to Percept Control in Spinal Cord Stimulation.** *Neuromodulation Technol Neural Interface* 2015, **2015**:n/a–n/a.
18. Holsheimer J, Buitenweg JR: **Review: Bioelectrical Mechanisms in Spinal Cord Stimulation.** *Neuromodulation Technol Neural Interface* 2015, **18**:161–170.
19. Lempka SF, Kilgore KL, McIntyre CC, Machado AG, Restoration N, Clinic C, Stokes L, Veterans C, Medical A, Engineering B, Western C: **Computational model of high-frequency spinal cord stimulation for chronic pain management.** In *Society for Neuroscience Meeting*; 2014.
20. Feirabend HKP, Choufoer H, Ploeger S, Holsheimer J, van Gool JD: **Morphometry of human superficial dorsal and dorsolateral column fibres: significance to spinal cord stimulation.** *Brain* 2002, **125**(Pt 5):1137–1149.
21. Holsheimer J: **Which neuronal elements are activated directly by spinal cord stimulation.** *Neuromodulation* 2002, **5**:25–31.
22. Doucet BM, Lam A, Griffin L: **Neuromuscular electrical stimulation for skeletal muscle function.** *Yale J Biol Med* 2012, **85**:201–15.
23. Rosell J, Colominas J, Riu P, Pallas-Areny R, Webster JG: **Skin impedance from 1 Hz to 1 MHz.** *IEEE Trans Biomed Eng* 1988, **35**:649–651.
24. Ward AR: **Electrical stimulation using kilohertz-frequency alternating current.** *Phys Ther* 2009, **89**:181–190.
25. Nemeč H: **Interferential therapy: a new approach in physical medicine.** *Br J Physiother*

1959.

26. Fuentes JP, Armijo-Olivo S, Magee DJ, Gross DP: **Effectiveness of interferential current therapy in the management of musculoskeletal pain: a systematic review and meta-analysis.** *Phys Ther* 2010, **90**:1219–1238.
27. Chase J, Robertson VJ, Southwell B, Hutson J, Gibb S: **Pilot study using transcutaneous electrical stimulation (interferential current) to treat chronic treatment-resistant constipation and soiling in children.** *J Gastroenterol Hepatol* 2005, **20**:1054–1061.
28. Furuta T, Takemura M, Tsujita J, Oku Y: **Interferential electric stimulation applied to the neck increases swallowing frequency.** *Dysphagia* 2012, **27**:94–100.
29. Agharezaee M, Mahnam A: **A computational study to evaluate the activation pattern of nerve fibers in response to interferential currents stimulation.** *Med Biol Eng Comput* 2015, **53**:713–720.
30. Kilgore KL, Bhadra N: **Nerve conduction block utilising high-frequency alternating current.** *Med Biol Eng Comput* 2004, **42**:394–406.
31. Patel Y, Butera RJ: **Differential fiber-specific block of nerve conduction in mammalian peripheral nerves using kilohertz electrical stimulation.** *J Neurophysiol* 2015;jn.00529.2014.
32. Bhadra N, Lahowetz E a., Foldes ST, Kilgore KL: **Simulation of high-frequency sinusoidal electrical block of mammalian myelinated axons.** *J Comput Neurosci* 2007, **22**:313–326.
33. Kilgore KL, Bhadra N: **Reversible nerve conduction block using kilohertz frequency alternating current.** *Neuromodulation* 2014, **17**:242–254.
34. Joseph L, Butera RJ: **High-frequency stimulation selectively blocks different types of fibers in frog sciatic nerve.** *IEEE Trans Neural Syst Rehabil Eng* 2011, **19**:550–557.
35. Mesin L, Merletti R: **Distribution of electrical stimulation current in a planar multilayer anisotropic tissue.** *IEEE Trans Biomed Eng* 2008, **55**:660–670.
36. Medina LE, Grill WM: **Volume conductor model of transcutaneous electrical stimulation with kilohertz signals.** *J Neural Eng* 2014, **11**:066012.
37. Ward AR, Robertson VJ: **Variation in motor threshold with frequency using kHz frequency alternating current.** *Muscle and Nerve* 2001, **24**:1303–1311.
38. Andrianova GG, Prokopenko GI, Shabashevich LB, Khvostov LN: **An apparatus for electrical stimulation of muscles, model Stimul-1.** *Biomed Eng (NY)* 1977, **11**:72–74.
39. Ward AR, Shkuratova N: **Russian electrical stimulation: the early experiments.** *Phys Ther* 2002, **82**:1019–1030.
40. Ward a R, Robertson VJ: **Variation in torque production with frequency using medium frequency alternating current.** *Arch Phys Med Rehabil* 1998, **79**:1399–1404.

41. Laufer Y, Elboim M: **Effect of burst frequency and duration of kilohertz-frequency alternating currents and of low-frequency pulsed currents on strength of contraction, muscle fatigue, and perceived discomfort.** *Phys Ther* 2008, **88**:1167–1176.
42. Ward AR, Oliver WG, Buccella D: **Wrist Extensor Torque Production and Discomfort Associated With Low-Frequency and Burst-Modulated Kilohertz-Frequency Currents.** *Phys Ther* 2006, **86**:1360–1367.
43. Ozcan J, Ward AR, Robertson VJ: **A comparison of true and premodulated interferential currents.** *Arch Phys Med Rehabil* 2004, **85**:409–415.
44. Bellew JW, Beiswanger Z, Freeman E, Gaerte C, Trafton J: **Interferential and burst-modulated biphasic pulsed currents yield greater muscular force than Russian current.** *Physiother Theory Pract* 2012, **28**:384–390.
45. Shen B, Roppolo JR, Subbaroyan J, Diubaldi A, Wahlgren S, de Groat WC, Tai C: **Neuromodulation of bladder activity by stimulation of feline pudendal nerve using a transdermal amplitude modulated signal (TAMS).** *Neurol Urodyn* 2011, **30**:1686–94.
46. Tai C, Shen B, Wang J, Liu H, Subbaroyan J, Roppolo JR, De Groat WC: **Inhibition of bladder overactivity by stimulation of feline pudendal nerve using transdermal amplitude-modulated signal (TAMS).** *BJU Int* 2012, **109**:782–787.
47. Monga AK, Linselmeyer TL: **Clinical Trial To Investigate the Efficacy of Acute Sacral Neurostimulation Using a Novel Transdermal Amplitude-Modulated Signal (Tams) in Subjects With Neurogenic Detrusor Overactivity.** *Eur Urol Suppl* 2011, **10**:190.
48. Elkelini MS, Pravdivyi I, Hassouna MM: **Mechanism of action of sacral nerve stimulation using a transdermal amplitude-modulated signal in a spinal cord injury rodent model.** *Can Urol Assoc J* 2012, **6**:227–230.
49. Monga A, Dmochowski R, Miller D: **Evaluation of a novel, non-invasive, patient-managed neuromodulation system (PMNS) on urgency, urinary incontinence and patient-reported outcomes in subjects with overactive bladder (OAB) syndrome who had previously failed therapy: a four week, multicentre.** In *International Continence Society Annual Meeting, Glasgow 2011*; 2011.
50. Slovak M, Barker a T, Chapple CR: **The assessment of a novel electrical stimulation waveform recently introduced for the treatment of overactive bladder.** *Physiol Meas* 2013, **34**:479–486.
51. Tyler WJ, Boasso AM, Charlesworth JD, Marlin MA, Aebersold K, Aven L, Wetmore DZ, Pal SK: **Transdermal neuromodulation of noradrenergic activity suppresses psychophysiological and biochemical stress responses in humans.** *bioRxiv* 2015(August):015032.
52. Gerasimenko Y, Gorodnichev R, Puhov A, Moshonkina T, Savochin A, Selionov V, Roy RR, Lu DC, Edgerton VR: **Initiation and modulation of locomotor circuitry output with multisite**

**transcutaneous electrical stimulation of the spinal cord in noninjured humans.** *J Neurophysiol* 2015, **113**(November 2014):834–842.

53. Soin A, Syed Shah N, Fang Z-P: **High-Frequency Electrical Nerve Block for Postamputation Pain: A Pilot Study.** *Neuromodulation Technol Neural Interface* 2015, **18**:197–206.

54. Soin A, Fang Z-P, Velasco J, Shah N, Guirguis M, Mekhail M: **High-frequency peripheral electric nerve block to treat postamputation pain.** *Tech Reg Anesth Pain Manag* 2014, **18**:156–162.

55. Schmalbruch H: **Fiber composition of the rat sciatic nerve.** *Anat Rec* 1986, **215**:71–81.

56. Bhadra N, Kilgore KL: **High-frequency electrical conduction block of mammalian peripheral motor nerve.** *Muscle and Nerve* 2005, **32**:782–790.

57. Waataja JJ, Tweden KS, Honda CN: **Effects of high-frequency alternating current on axonal conduction through the vagus nerve.** *J Neural Eng* 2011, **8**:056013.

58. Sarr MG, Billington CJ, Brancatisano R, Brancatisano A, Toouli J, Kow L, Nguyen NT, Blackstone R, Maher JW, Shikora S, Reeds DN, Eagon JC, Wolfe BM, O'Rourke RW, Fujioka K, Takata M, Swain JM, Morton JM, Ikramuddin S, Schweitzer M, Chand B, Rosenthal R: **The EMPOWER study: randomized, prospective, double-blind, multicenter trial of vagal blockade to induce weight loss in morbid obesity.** *Obes Surg* 2012, **22**:1771–1782.

59. Camilleri M, Toouli J, Herrera MF, Kulseng B, Kow L, Pantoja JP, Marvik R, Johnsen G, Billington CJ, Moody FG, Knudson MB, Tweden KS, Vollmer M, Wilson RR, Anvari M: **Intra-abdominal vagal blocking (VBLOC therapy): Clinical results with a new implantable medical device.** *Surgery* 2008, **143**:723–731.

60. Tweden KS, Sarr MG, Camilleri M, Kendrick ML, Moody FG, Bierk MD, Knudson MB, Wilson RR, Anvari M: **46: Vagal Blocking for Obesity Control (VBLOC): Studies of pancreatic and gastric function and safety in a porcine model.** *Surg Obes Relat Dis* 2006, **2**:301–302.

61. Ikramuddin S, Blackstone RP, Brancatisano A, Toouli J, Shah SN, Wolfe BM, Fujioka K, Maher JW, Swain J, Que FG, Morton JM, Leslie DB, Brancatisano R, Kow L, O'Rourke RW, Deveney C, Takata M, Miller CJ, Knudson MB, Tweden KS, Shikora S a., Sarr MG, Billington CJ: **Effect of reversible intermittent intra-abdominal vagal nerve blockade on morbid obesity: the ReCharge randomized clinical trial.** *Jama* 2014, **312**:915–22.

62. Cottrell DF: **Conduction velocity and axonal diameter of alimentary C fibres.** *Q J Exp Physiol* 1984, **69**:355–64.

63. Pelot NA, Behrend CE, Grill WM: **Modeling the Response of Small Myelinated and Unmyelinated Axons to Kilohertz Frequency Signals.** In *IEEE EMBS Conference on Neural Engineering*; 2015:406–409.

64. Antal A, Paulus W: **Transcranial alternating current stimulation (tACS)**. *Front Hum Neurosci* 2013, **7**(June):317.
65. Chaieb L, Antal A, Paulus W: **Transcranial alternating current stimulation in the low kHz range increases motor cortex excitability**. *Restor Neurol Neurosci* 2011, **29**:167–175.
66. Kirson ED, Dbaly V, Tovarys F, Vymazal J, Soustiel JF, Itzhaki a, Mordechovich D, Steinberg-Shapira S, Gurvich Z, Schneiderman R, Wasserman Y, Salzberg M, Ryffel B, Goldsher D, Dekel E, Palti Y: **Alternating electric fields arrest cell proliferation in animal tumor models and human brain tumors**. *Proc Natl Acad Sci* 2007, **104**:10152–10157.
67. Stupp R, Taillibert S, Kanner AA, Kesari S, Steinberg DM, Toms SA, Taylor LP, Lieberman F, Silvani A, Fink KL, Barnett GH, Zhu JJ, Henson JW, Engelhard HH, Chen TC, Tran DD, Sroubek J, Tran ND, Hottinger AF, Landolfi J, Desai R, Caroli M, Kew Y, Honnorat J, Idbaih A, Kirson ED, Weinberg U, Palti Y, Hegi ME, Ram Z: **Maintenance Therapy With Tumor-Treating Fields Plus Temozolomide vs Temozolomide Alone for Glioblastoma**. *Jama* 2015, **314**:2535.
68. Wick W: **TTFields: where does all the skepticism come from?** *Neuro Oncol* 2016, **18**:303–305.
69. Howell B, Medina LE, Grill WM: **Effects of frequency-dependent membrane capacitance on neural excitability**. *J Neural Eng* 2015, **12**:056015.
70. Collins KL, Lehmann EM, Patil PG: **Deep brain stimulation for movement disorders**. *Neurobiol Dis* 2010, **38**:338–345.
71. Benabid AL, Pollak P, Gao D, Hoffmann D, Limousin P, Gay E, Payen I, Benazzouz A: **Chronic electrical stimulation of the ventralis intermedius nucleus of the thalamus as a treatment of movement disorders**. *J Neurosurg* 1996, **84**:203–214.
72. Grill WM, Snyder AN, Miocinovic S: **Deep brain stimulation creates an informational lesion of the stimulated nucleus**. *Neuroreport* 2004, **15**:1137–1140.
73. Couto J, Grill WM: **Kilohertz Frequency Deep Brain Stimulation Is Ineffective at Regularizing the Firing of Model Thalamic Neurons**. *Front Comput Neurosci* 2016, **10**(March):1–12.
74. Weinberg SH: **High-frequency stimulation of excitable cells and networks**. *PLoS One* 2013, **8**.
75. Rattay F: **High frequency electrostimulation of excitable cells**. *J Theor Biol* 1986, **123**:45–54.
76. Woo MY, Campbell B: **Asynchronous firing and block of peripheral nerve conduction by 20 kc alternating current**. *Bull Los Angel Neuro Soc* 1964, **29**:87–94.
77. Bowman BR, McNeal DR: **Response of single alpha motoneurons to high-frequency pulse trains. Firing behavior and conduction block phenomenon**. *Appl Neurophysiol* 1986, **49**:121–

138.

78. Mino H, Rubinstein JT: **Effects of neural refractoriness on spatio-temporal variability in spike initiations with electrical stimulation.** *IEEE Trans Neural Syst Rehabil Eng* 2006, **14**:273–280.
79. Gerges M, Foldes EL, Ackermann DM, Bhadra N, Bhadra N, Kilgore KL: **Frequency- and amplitude-transitioned waveforms mitigate the onset response in high-frequency nerve block.** *J Neural Eng* 2010, **7**:066003.
80. Krauthamer V, Croscheck T: **Effects of high-rate electrical stimulation upon firing in modelled and real neurons.** *Med Biol Eng Comput* 2002, **40**:360–6.
81. Hirsch HR: **Squid giant axon: repetitive responses to alternating current stimulation.** *Nature* 1965, **208**:1218–1219.
82. Hartmann R, Topp G, Klinke R: **Discharge patterns of cat primary auditory fibers with electrical stimulation of the cochlea.** *Hear Res* 1984, **13**:47–62.
83. Boërio D, Hogrel J-Y, Créange A, Lefaucheur J-P: **Méthodes et intérêt clinique de la mesure de la période réfractaire nerveuse périphérique chez l'homme.** *Neurophysiol Clin Neurophysiol* 2004, **34**:279–291.
84. Kiernan MC, Mogyoros I, Burke D: **Differences in the recovery of excitability in sensory and motor axons of human median nerve.** *Brain* 1996, **119** ( Pt 4):1099–1105.
85. Trevillion L, Howells J, Bostock H, Burke D: **Properties of low-threshold motor axons in the human median nerve.** *J Physiol* 2010, **588**(Pt 13):2503–2515.
86. McIntyre CC, Richardson AG, Grill WM: **Modeling the excitability of mammalian nerve fibers: influence of afterpotentials on the recovery cycle.** *J Neurophysiol* 2002, **87**:995–1006.
87. Hill A V., Katz B, Solandt DY: **Nerve excitation by alternating current.** *Proc R Soc London Ser B, Biol Sci* 1936, **121**:74–133.
88. Katz B: **Nerve excitation by high-frequency alternating current.** *J Physiol* 1939, **96**:202–224.
89. Rakhmilevich LS: **Analysis of the stimualting effect of a half-wave and full-wave rectified current of varying frequency.** *Bull Exp Biol Med USSR* 1966, **61**:460–462.
90. Rubinstein JT: **Threshold fluctuations in an N sodium channel model of the node of Ranvier.** *Biophys J* 1995, **68**:779–785.
91. Rubinstein JT, Wilson BS, Finley CC, Abbas PJ: **Pseudospontaneous activity: Stochastic independence of auditory nerve fibers with electrical stimulation.** *Hear Res* 1999, **127**:108–118.
92. Cai C, Twyford P, Fried S: **The response of retinal neurons to high-frequency stimulation.**

*J Neural Eng* 2013, **10**:036009.

93. Twyford P, Cai C, Fried S: **Differential responses to high-frequency electrical stimulation in ON and OFF retinal ganglion cells.** *J Neural Eng* 2014, **11**:025001.
94. Kameneva T, Maturana MI, Hadjinicolaou AE, Cloherty SL, Ibbotson MR, Grayden DB, Burkitt AN, Meffin H: **Retinal ganglion cells: mechanisms underlying depolarization block and differential responses to high frequency electrical stimulation of ON and OFF cells.** *J Neural Eng* 2016, **13**:016017.
95. Cohen ED: **Prosthetic interfaces with the visual system: biological issues.** *J Neural Eng* 2007, **4**:R14–R31.
96. Tai C, De Groat WC, Roppolo JR: **Simulation of nerve block by high-frequency sinusoidal electrical current based on the Hodgkin-Huxley model.** *IEEE Trans Neural Syst Rehabil Eng* 2005, **13**:415–422.
97. Ackermann DM, Bhadra N, Gerges M, Thomas PJ: **Dynamics and sensitivity analysis of high-frequency conduction block.** *J Neural Eng* 2011, **8**:065007.
98. Bromm B: **Spike frequency of the nodal membrane generated by high-frequency alternating current.** *Pflugers Arch* 1975, **353**:1–19.
99. Pyragas K, Novičenko V, Tass PA: **Mechanism of suppression of sustained neuronal spiking under high-frequency stimulation.** *Biol Cybern* 2013, **107**:669–684.
100. Zhang F, Miller CA, Robinson BK, Abbas PJ, Hu N: **Changes across time in spike rate and spike amplitude of auditory nerve fibers stimulated by electric pulse trains.** *JARO - J Assoc Res Otolaryngol* 2007, **8**:356–372.
101. Negm M, Bruce I: **The Effects of HCN and KLT Ion Channels on Adaptation and Refractoriness in a Stochastic Auditory Nerve Model.** *IEEE Trans Biomed Eng* 2014, **9294**(c):1–12.
102. Chen C: **Hyperpolarization-activated current (I<sub>h</sub>) in primary auditory neurons.** *Hear Res* 1997, **110**:179–190.
103. Howells J, Trevillion L, Bostock H, Burke D: **The voltage dependence of I<sub>h</sub> in human myelinated axons.** *J Physiol* 2012, **590**(Pt 7):1625–40.
104. Woo J, Miller CA, Abbas PJ: **Simulation of the electrically stimulated cochlear neuron: Modeling adaptation to trains of electric pulses.** *IEEE Trans Biomed Eng* 2009, **56**:1348–1359.
105. Jensen a L, Durand DM: **Suppression of axonal conduction by sinusoidal stimulation in rat hippocampus in vitro.** *J Neural Eng* 2007, **4**:1–16.
106. Tanner JA: **Reversible blocking of nerve conduction by alternating-current excitation.** *Nature* 1962, **195**:712–713.

107. Joseph L, Butera RJ: **Unmyelinated Aplysia nerves exhibit a non monotonic blocking response to high frequency stimulation.** *IEEE Trans Neural Syst Rehabil Eng* 2009, **17**:537–544.
108. Ackermann DM, Ethier C, Foldes EL, Oby ER, Tyler D, Bauman M, Bhadra N, Miller L, Kilgore KL: **Electrical conduction block in large nerves: High-frequency current delivery in the nonhuman primate.** *Muscle Nerve* 2011, **43**:897–899.
109. Fisher KM, Jillani NE, Oluoch GO, Baker SN: **Blocking central pathways in the primate motor system using high frequency sinusoidal current.** *J Neurophysiol* 2014:00347.
110. Zhao S, Yang G, Wang J, Roppolo JR, de Groat WC, Tai C: **Effect of non-symmetric waveform on conduction block induced by high-frequency (kHz) biphasic stimulation in unmyelinated axon.** *J Comput Neurosci* 2014, **37**:377–386.
111. Franke M, Bhadra N, Bhadra N, Kilgore K: **Direct current contamination of kilohertz frequency alternating current waveforms.** *J Neurosci Methods* 2014, **232**:74–83.
112. Franke M, Vrabc T, Wainright J, Bhadra N, Bhadra N, Kilgore K: **Combined KHfAC + DC nerve block without onset or reduced nerve conductivity after block.** *J Neural Eng* 2014, **11**:056012.
113. Grill WM: **Modeling the effects of electric fields on nerve fibers: influence of tissue electrical properties.** *IEEE Trans Biomed Eng* 1999, **46**:918–928.
114. Plonsey R, Heppner DB: **Considerations of quasi-stationarity in electrophysiological systems.** *Bull Math Biophys* 1967, **29**:657–664.
115. Foster KR, Schwan HP: **Dielectric properties of tissues and biological materials: a critical review.** *Crit Rev Biomed Eng* 1989, **17**:25–104.
116. Bédard C, Kröger H, Destexhe A: **Modeling extracellular field potentials and the frequency-filtering properties of extracellular space.** *Biophys J* 2004, **86**:1829–42.
117. Gabriel C, Gabriel C, Gabriel S, Gabriel S, Corthout E, Corthout E: **The dielectric properties of biological tissues: I. Literature survey.** *Phys Med Biol* 1996, **41**:2231–49.
118. Gabriel S, Lau RW, Gabriel C: **The dielectric properties of biological tissues: II. Measurements in the frequency range 10 Hz to 20 GHz.** *Phys Med Biol* 1996, **41**:2251–2269.
119. Geddes LA, Baker LE: **The specific resistance of biological material - A compendium of data for the biomedical engineer and physiologist.** *Med Biol Eng* 1967, **5**:271–293.
120. Weerasuriya A, Spangler RA, Rapoport SI, Taylor RE: **AC impedance of the perineurium of the frog sciatic nerve.** *Biophys J* 1984, **46**:167–74.
121. Gabriel S, Lau RW, Gabriel C: **The dielectric properties of biological tissues: III. Parametric models for the dielectric spectrum of tissues.** *Phys Med Biol* 1996, **41**:2271–2293.

122. Bossetti C a, Birdno MJ, Grill WM: **Analysis of the quasi-static approximation for calculating potentials generated by neural stimulation.** *J Neural Eng* 2008, **5**:44–53.
123. Butson CR, McIntyre CC: **Tissue and electrode capacitance reduce neural activation volumes during deep brain stimulation.** *Clin Neurophysiol* 2005, **116**:2490–2500.
124. Grant PF, Lowery MM: **Effect of dispersive conductivity and permittivity in volume conductor models of deep brain stimulation.** *IEEE Trans Biomed Eng* 2010, **57**(10 PART 1):2386–2393.
125. Awayda MS, Van Driessche W, Helman SI: **Frequency-dependent capacitance of the apical membrane of frog skin: dielectric relaxation processes.** *Biophys J* 1999, **76**(1 Pt 1):219–232.
126. Haydon BYD a, Requena J, Urban BW: **Some effects of aliphatic hydrocarbons on the electrical capacity and ionic currents of the squid giant membrane.** *J Physiol* 1980, **309**:229–245.
127. Kuhn A, Keller T, Lawrence M, Morari M: **The influence of electrode size on selectivity and comfort in transcutaneous electrical stimulation of the forearm.** *IEEE Trans Neural Syst Rehabil Eng* 2010, **18**:255–262.
128. Raicu V, Kitagawa N, Irimajiri a: **A quantitative approach to the dielectric properties of the skin.** *Phys Med Biol* 2000, **45**:L1–L4.
129. Kuhn A, Keller T, Lawrence M, Morari M: **A model for transcutaneous current stimulation: Simulations and experiments.** *Med Biol Eng Comput* 2009, **47**:279–289.
130. Cantrell DR, Inayat S, Taflove A, Ruoff RS, Troy JB: **Incorporation of the electrode-electrolyte interface into finite-element models of metal microelectrodes.** *J Neural Eng* 2008, **5**:54–67.
131. Merrill DR, Bikson M, Jefferys JGR: **Electrical stimulation of excitable tissue: Design of efficacious and safe protocols.** *J Neurosci Methods* 2005, **141**:171–198.
132. McAdams ET, Jossinet J, Lacknermeier a., Risacher F: **Factors affecting electrode-gel-skin interface impedance in electrical impedance tomography.** *Med Biol Eng Comput* 1996, **34**:397–408.
133. Panescu D, Webster JG, Stratbucker R a: **A nonlinear finite element model of the electrode-electrolyte-skin system.** *IEEE Trans Biomed Eng* 1994, **41**:681–687.
134. Vargas Luna JL, Krenn M, Cortés Ramírez JA, Mayr W: **Dynamic Impedance Model of the Skin-Electrode Interface for Transcutaneous Electrical Stimulation.** *PLoS One* 2015, **10**:e0125609.
135. Sawan M, Laaziri Y, Mounaim F, Elzayat E, Corcos J, Elhilali MM: **Electrode-tissues interface: modeling and experimental validation.** *Biomed Mater* 2007, **2**:S7–S15.

136. Wei XF, Grill WM: **Impedance characteristics of deep brain stimulation electrodes in vitro and in vivo.** *J Neural Eng* 2009, **6**:046008.
137. Lempka SF, Miocinovic S, Johnson MD, Vitek JL, McIntyre CC: **In vivo impedance spectroscopy of deep brain stimulation electrodes.** *J Neural Eng* 2009, **6**:046001.
138. Butson CR, Moks CB, McIntyre CC: **Sources and effects of electrode impedance during deep brain stimulation.** *Clin Neurophysiol* 2006, **117**:447–454.
139. Rattay F: **Modeling the excitation of fibers under surface electrodes.** *IEEE Trans Biomed Eng* 1988, **35**:199–202.
140. Wiley JD, Webster JG: **Analysis and control of the current distribution under circular dispersive electrodes.** *IEEE Trans Biomed Eng* 1982, **29**:381–385.
141. Sagi-Dolev AM, Prutchi D, Nathan RH: **Three-dimensional current density distribution under surface stimulation electrodes.** *Med Biol Eng Comput* 1995, **33**(3 SPEC. ISSUE):403–408.
142. Kao TJ, Saulnier GJ, Isaacson D, Szabo TL, Newell JC: **A versatile high-permittivity phantom for EIT.** *IEEE Trans Biomed Eng* 2008, **55**:2601–2607.
143. Gagnon H, Cousineau M, Adler A, Hartinger AE: **A resistive mesh phantom for assessing the performance of EIT systems.** *IEEE Trans Biomed Eng* 2010, **57**:2257–2266.
144. Medina LE, Grill WM: **Phantom Model of Transcutaneous Electrical Stimulation with Kilohertz Signals.** In *IEEE EMBS Conference on Neural Engineering. Volume 2015-July*; 2015:22–24.
145. Gabriel C: **Tissue equivalent material for hand phantoms.** *Phys Med Biol* 2007, **52**:4205–4210.
146. Bennett D: **NaCl doping and the conductivity of agar phantoms.** *Mater Sci Eng C* 2011, **31**:494–498.
147. Sadleir RJ, Neralwala F, Te T, Tucker A: **A controllably anisotropic conductivity or diffusion phantom constructed from isotropic layers.** *Ann Biomed Eng* 2009, **37**:2522–2531.
148. Tidswell AT, Bagshaw AP, Holder DS, Yerworth RJ, Eadie L, Murray S, Morgan L, Bayford RH: **A comparison of headnet electrode arrays for electrical impedance tomography of the human head.** *Physiol Meas* 2003, **24**:527–544.
149. Pope JE, Falowski S, Deer TR: **Advanced waveforms and frequency with spinal cord stimulation: burst and high-frequency energy delivery.** *Expert Rev Med Devices* 2015, **12**:431–437.
150. Shannon R V: **A Model of Safe Levels for Electrical Stimulation.** *IEEE T Bio-Med Eng* 1992, **39**:424–426.

151. Cogan SF, Ludwig KA, Welle CG, Takmakov P: **Tissue damage thresholds during therapeutic electrical stimulation.** *J Neural Eng* 2016, **13**:021001.
152. McCreery DB, Agnew WF, Yuen TGH, Bullara LA: **Relationship between stimulus amplitude, stimulus frequency and neural damage during electrical stimulation of sciatic nerve of cat.** *Med Biol Eng Comput* 1995, **33**(3 SPEC. ISSUE):426–429.
153. McCreery DB, Yuen TGH, Agnew WF, Bullara LA: **A characterization of the effects on neuronal excitability due to prolonged microstimulation with chronically implanted microelectrodes.** *IEEE Trans Biomed Eng* 1997, **44**:931–939.
154. Butterwick A, Vankov A, Huie P, Freyvert Y, Palanker D: **Tissue damage by pulsed electrical stimulation.** *IEEE Trans Biomed Eng* 2007, **54**:2261–2267.
155. Xu J, Shepherd RK, Millard RE, Clark GM: **Chronic electrical stimulation of the auditory nerve at high stimulus rates: A physiological and histopathological study.** *Hear Res* 1997, **105**:1–29.
156. Michael Tykocinski, Shepherd RK, Clark GM: **Reduction in excitability of the auditory nerve following electrical stimulation at high stimulus rates.** *Hear Res* 1995, **88**:124–142.
157. Sluka KA, Smith HS, Walsh DM: **Transcutaneous electrical nerve stimulation: A review.** In *Neuromodulation*. Edited by Krames ES, Peckham PH, Rezai AR. Elsevier Ltd; 2009.
158. Hartinger AE, Guardo R, Kokta V, Gagnon H: **A 3-D hybrid finite element model to characterize the electrical behavior of cutaneous tissues.** *IEEE Trans Biomed Eng* 2010, **57**:780–789.
159. McNeal DR: **Analysis of a model for excitation of myelinated nerve.** *IEEE Trans Biomed Eng* 1976, **23**:329–337.
160. Farina D, Rainoldi A: **Compensation of the effect of sub-cutaneous tissue layers on surface EMG: A simulation study.** *Med Eng Phys* 1999, **21**:487–497.
161. Tracey B, Williams M: **Computationally efficient bioelectric field modeling and effects of frequency-dependent tissue capacitance.** *J Neural Eng* 2011, **8**:036017.
162. Kaufmann S, Ardelt G, Ryschka M: **Measurements of Electrode Skin Impedances using Carbon Rubber Electrodes – First Results.** *J Phys Conf Ser* 2013, **434**:012020.
163. McAdams ET, Lacknermeier A, Jossinet J: **AC impedance of the hydrogel-skin interface.** *Proc 16th Annu Int Conf IEEE Eng Med Biol Soc* 1994:0–1.
164. Cole KS, Cole RH: **Dispersion and Absorption in Dielectrics I. Alternating Current Characteristics.** *J Chem Phys* 1941, **9**:341–351.
165. Hines ML, Carnevale NT: **The NEURON simulation environment.** *Neural Comput* 1997, **9**:1179–1209.

166. Rattay F: **Analysis of models for extracellular fiber stimulation.** *IEEE Trans Biomed Eng* 1989, **36**:676–682.
167. Warman EN, Grill WM, Durand D: **Modeling the effects of electric fields on nerve fibers: Determination of excitation thresholds.** *IEEE Trans Biomed Eng* 1992, **39**:1244–1254.
168. Dorgan SJ, Reilly RB: **A model for human skin impedance during surface functional neuromuscular stimulation.** *IEEE Trans Rehabil Eng* 1999, **7**:341–348.
169. Durand DM, Grill WM, Kirsch R: *Electrical Stimulation of the Neuromuscular System.* 2005.
170. Chen CF, Chen WS, Chou LW, Chang YJ, Chen SC, Kuo TS, Lai JS: **Pulse energy as a reliable reference for twitch forces induced by transcutaneous neuromuscular electrical stimulation.** *IEEE Trans Neural Syst Rehabil Eng* 2012, **20**:574–583.
171. Mørch CD, Hennings K, Andersen OK: **Estimating nerve excitation thresholds to cutaneous electrical stimulation by finite element modeling combined with a stochastic branching nerve fiber model.** *Med Biol Eng Comput* 2011, **49**:385–395.
172. Nightingale K, Palmeri M, Trahey G: **Analysis of contrast in images generated with transient acoustic radiation force.** *Ultrasound Med Biol* 2006, **32**:61–72.
173. Plonsey R: *Bioelectric Phenomena.* McGraw-Hill; 1969.
174. Sperandio M, Guermandi M, Guerrieri R: **A four-shell diffusion phantom of the head for electrical impedance tomography.** *IEEE Trans Biomed Eng* 2012, **59**:383–389.
175. Grill WM, Norman SE, Bellamkonda R V: **Implanted neural interfaces: biochallenges and engineered solutions.** *Annu Rev Biomed Eng* 2009, **11**:1–24.
176. Beatti A, Rayner A, Chipchase L, Souvlis T: **Penetration and spread of interferential current in cutaneous, subcutaneous and muscle tissues.** *Physiotherapy* 2011, **97**:319–326.
177. Boggs JW, Wenzel BJ, Gustafson KJ, Grill WM: **Frequency-dependent selection of reflexes by pudendal afferents in the cat.** *J Physiol* 2006, **577**(Pt 1):115–126.
178. Geddes L a, Bourland JD: **The strength-duration curve.** *IEEE Trans Biomed Eng* 1985, **32**:458–459.
179. Moldovan M, Krarup C: **Persistent abnormalities of membrane excitability in regenerated mature motor axons in cat.** *J Physiol* 2004, **560**:795–806.
180. Vargas Luna JL, Krenn M, Löfler S, Kern H, Cortes Ramirez JA, Mayr W: **Comparison of twitch responses during current- or voltage-controlled transcutaneous neuromuscular electrical stimulation.** *Artif Organs* 2015, **39**:868–875.
181. Wongsarnpigoon A, Grill WM: **Energy-efficient waveform shapes for neural stimulation revealed with a genetic algorithm.** *J Neural Eng* 2010, **7**:046009.

182. Kapural L: **Spinal cord stimulation for intractable chronic pain.** *Curr Pain Headache Rep* 2014, **18**:18–23.
183. Zhang TC, Janik JJ, Peters R V, Chen G, Ji R-R, Grill WM: **Spinal Sensory Projection Neuron Responses to Spinal Cord Stimulation Are Mediated by Circuits Beyond Gate Control.** *J Neurophysiol* 2015;jn.00147.2015.
184. Struijk JJ, Holsheimer J, Barolat G, He J, Boom HBK: **Paresthesia thresholds in spinal cord stimulation: a comparison of theoretical results with clinical data.** *IEEE Trans Rehabil Eng* 1993, **1**:101–108.
185. Struijk JJ, Holsheimer J, Spincemaille GH, Gielen FL, Hoekema R: **Theoretical performance and clinical evaluation of transverse tripolar spinal cord stimulation.** *IEEE Trans Rehabil Eng* 1998, **6**:277–285.
186. Davidoff RA: **The dorsal columns.** *Neurology* 1989:1377–1385.
187. Glees P, Soler J: **Fibre content of the posterior column and synaptic connections of nucleus gracilis.** *Zeitschrift fur Zellforsch und Mikroskopische Anat* 1951, **36**:381–400.
188. Horch KW: **Ascending collaterals of cutaneous neurons in the fasciculus gracilis of the cat during peripheral nerve regeneration.** *Brain Res* 1976, **117**:19–32.
189. Brown AG: **Cutaneous afferent fibre collaterals in the dorsal columns of the cat.** *Exp Brain Res* 1968, **5**:293–305.
190. Waxman SG, Kocsis JD, Stys PK: *The Axon: Structure, Function, and Pathophysiology.* Oxford University Press; 1995.
191. Fraher JP: **The maturation of the ventral root-spinal cord transitional zone. An ultrastructural study.** *J Neurol Sci* 1978, **36**:427–449.
192. Bélanger E, Crépeau J, Laffray S, Vallée R, De Koninck Y, Co<sup>^</sup>té D: **Live animal myelin histomorphometry of the spinal cord with video-rate multimodal nonlinear microendoscopy.** *J Biomed Opt* 2012, **17**:021107.
193. Nashmi R, Fehlings MG: **Changes in axonal physiology and morphology after chronic compressive injury of the rat thoracic spinal cord.** *Neuroscience* 2001, **104**:235–251.
194. Krishnan A V., Lin CSY, Park SB, Kiernan MC: **Axonal ion channels from bench to bedside: A translational neuroscience perspective.** *Prog Neurobiol* 2009, **89**:288–313.
195. Kiernan MC, Baker MD, Bostock H: **Characteristics of late Na(+) current in adult rat small sensory neurons.** *Neuroscience* 2003, **119**:653–60.
196. Kocsis J effery D, Waxman SG: **Absence of potassium conductance in central myelinated axons.** *Nature* 1980, **287**:348–349.
197. Black JA, Waxman SG, Smith KJ: **Remyelination of dorsal column axons by endogenous**

- Schwann cells restores the normal pattern of Nav1.6 and Kv1.2 at nodes of Ranvier.** *Brain* 2006, **129**(Pt 5):1319–29.
198. Caldwell JH, Schaller KL, Lasher RS, Peles E, Levinson SR: **Sodium channel Na(v)1.6 is localized at nodes of ranvier, dendrites, and synapses.** *Proc Natl Acad Sci U S A* 2000, **97**:5616–20.
199. Raman IM, Bean BP: **Resurgent sodium current and action potential formation in dissociated cerebellar Purkinje neurons.** *J Neurosci* 1997, **17**:4517–4526.
200. Cummins TR, Dib-Hajj SD, Herzog RI, Waxman SG: **Nav1.6 channels generate resurgent sodium currents in spinal sensory neurons.** *FEBS Lett* 2005, **579**:2166–2170.
201. Sittl R, Lampert a., Huth T, Schuy ET, Link a. S, Fleckenstein J, Alzheimer C, Grafe P, Carr RW: **Anticancer drug oxaliplatin induces acute cooling-aggravated neuropathy via sodium channel subtype NaV1.6-resurgent and persistent current.** *Proc Natl Acad Sci* 2012, **109**:6704–6709.
202. Buffington S a, Rasband MN: **Na<sup>+</sup> channel-dependent recruitment of NavB4 to axon initial segments and nodes of Ranvier.** *J Neurosci* 2013, **33**:6191–6202.
203. Schwarz JR, Glassmeier G, Cooper EC, Kao T-C, Nodera H, Tabuena D, Kaji R, Bostock H: **KCNQ channels mediate IKs, a slow K<sup>+</sup> current regulating excitability in the rat node of Ranvier.** *J Physiol* 2006, **573**(Pt 1):17–34.
204. Rydmark M: **Nodal axon diameter correlates linearly with internodal axon diameter in spinal roots of the cat.** *Neurosci Lett* 1981, **24**:247–50.
205. Johnson C, Holmes WR, Brown A, Jung P: **Minimizing the caliber of myelinated axons by means of nodal constrictions.** *J Neurophysiol* 2015:jn.00338.2015.
206. Hess A, Young JZ: **The nodes of Ranvier.** *Proc R Soc Lond B Biol Sci* 1952, **140**:301–320.
207. Murray JA, Blakemore WF: **The relationship between internodal length and fibre diameter in the spinal cord of the cat.** *J Neurol Sci* 1980, **45**:29–41.
208. Rydmark M, Berthold C-H: **Electron microscopic serial section analysis of nodes of Ranvier in lumbosacral spinal roots of the cat: ultrastructural organization of nodal compartments in fibres of different sizes.** *J Neurocytol* 1983, **12**:537–565.
209. Haydon DA, Urban BW: **The admittance of the squid giant axon at radio frequencies and its relation to membrane structure.** *J Physiol* 1985:275–291.
210. Gentet LJ, Stuart GJ, Clements JD: **Direct measurement of specific membrane capacitance in neurons.** *Biophys J* 2000, **79**:314–320.
211. Sykova E, Hájek I, Chvátal A, Kříž N, Diatchkova GI: **Changes in extracellular potassium accumulation produced by opioids and naloxone in frog spinal cord: Relation to changes of Na/1b-K pump activity.** *Neurosci Lett* 1985, **59**:285–290.

212. Czéh G, Kříž N, Syková E: **Extracellular potassium accumulation in the frog spinal cord induced by stimulation of the skin and ventrolateral columns.** *J Physiol* 1981, **320**:57–72.
213. Feng Z, Yu Y, Guo Z, Cao J, Durand DM: **High Frequency Stimulation Extends the Refractory Period and Generates Axonal Block in the Rat Hippocampus.** *Brain Stimul* 2014, **7**:1–10.
214. Bellinger SC, Miyazawa G, Steinmetz PN: **Submyelin potassium accumulation may functionally block subsets of local axons during deep brain stimulation: a modeling study.** *J Neural Eng* 2008, **5**:263–274.
215. Heinemann U, Schaible HG, Schmidt RF: **Changes in extracellular potassium concentration in cat spinal cord in response to innocuous and noxious stimulation of legs with healthy and inflamed knee joints.** *Exp brain Res* 1990, **79**:283–92.
216. Bay V, Butt AM: **Relationship between glial potassium regulation and axon excitability: A role for glial Kir4.1 channels.** *Glia* 2012, **60**:651–660.
217. BeMent SL, Ranck JB: **A quantitative study of electrical stimulation of central myelinated fibers.** *Exp Neurol* 1969, **24**:147–170.
218. Sweeney JD, Mortimer JT, Durand DM: **Modeling of mammalian myelinated nerve for functional neuromuscular stimulation.** In *IEEE 9th Annual Conference of the Engineering in Medicine and Biology Society*; 1987:1577–1578.
219. Wesselink WA, Holsheimer J, Boom HB: **A model of the electrical behaviour of myelinated sensory nerve fibres based on human data.** *Med Biol Eng Comput* 1999, **37**:228–235.
220. Terada M, Yasuda H, Kikkawa R, Koyama N, Yokota T, Shigeta Y: **Electrophysiological study of dorsal column function in streptozocin-induced diabetic rats: Comparison with 2,5-hexanedione intoxication.** *J Neurol Sci* 1993, **115**:58–66.
221. Parker JL, Karantonis DM, Single PS, Obradovic M, Laird J, Gorman RB, Ladd L a, Cousins MJ: **Electrically Evoked Compound Action Potentials Recorded From the Sheep Spinal Cord.** *Neuromodulation Technol Neural Interface* 2013, **16**:295–303.
222. Bostock H: **The strength-duration relationship for excitation of myelinated nerve: computed dependence on membrane parameters.** *J Physiol* 1983, **341**:59–74.
223. Rattay F, Paredes LP, Leao RN: **Strength-duration relationship for intra- versus extracellular stimulation with microelectrodes.** *Neuroscience* 2012, **214**:1–13.
224. Goldberg JM, Brown PB: **Response of binaural neurons of dog superior olivary complex to dichotic tonal stimuli: some physiological mechanisms of sound localization.** *J Neurophysiol* 1969, **32**:613–636.
225. Hamming RW: **Error Detecting and Error Correcting Codes.** *Bell Syst Tech J* 1950, **29**:147–160.

226. Victor JD, Purpura KP: **Nature and precision of temporal coding in visual cortex: a metric-space analysis.** *J Neurophysiol* 1996, **76**:1310–1326.
227. Kohama I, Lankford KL, Preiningerova J, White F a, Vollmer TL, Kocsis JD: **Transplantation of cryopreserved adult human Schwann cells enhances axonal conduction in demyelinated spinal cord.** *J Neurosci* 2001, **21**:944–950.
228. Kocsis JD, Waxman SG: **Intra-axonal recordings in rat dorsal column axons: membrane hyperpolarization and decreased excitability precede the primary afferent depolarization.** *Brain* 1982, **238**:222–227.
229. Horch KW, Burgess PR, Whitehorn D: **Ascending collaterals of cutaneous neurons in the fasciculus gracilis of the cat.** *Brain Res* 1976, **117**:1–17.
230. Richardson a G, McIntyre CC, Grill WM: **Modelling the effects of electric fields on nerve fibres: influence of the myelin sheath.** *Med Biol Eng Comput* 2000, **38**:438–446.
231. Holsheimer J, Buitenweg JR, Das J, De Sutter P, Manola L, Nuttin B: **The effect of pulse width and contact configuration on paresthesia coverage in spinal cord stimulation.** *Neurosurgery* 2011, **68**:1452–1461.
232. West DC, Wolstencroft JH: **Strength-duration characteristics of myelinated and non-myelinated bulbospinal axons in the cat spinal cord.** *J Physiol* 1983, **337**:37–50.
233. Barrett EF, Barrett JN: **Intracellular recording from vertebrate myelinated axons: mechanism of the depolarizing afterpotential.** *J Physiol* 1982, **323**:117–44.
234. Brazhe AR, Maksimov G V: **Activity-Related Structural Changes in the Myelinated Nerve Fiber.** In *Biosimulation in Biomedical Research, Health Care and Drug Development.* Vienna: Springer Vienna; 2011:153–177.
235. Lempka SF, McIntyre CC, Kilgore KL, Machado AG: **Computational Analysis of Kilohertz Frequency Spinal Cord Stimulation for Chronic Pain Management.** *Anesthesiology* 2015, **122**:1–15.
236. Tan DW, Schiefer M a., Keith MW, Anderson JR, Tyler J, Tyler DJ: **A neural interface provides long-term stable natural touch perception.** *Sci Transl Med* 2014, **138**.
237. Zhang TC, Janik JJ, Grill WM: **Modeling the effects of spinal cord stimulation on wide dynamic range dorsal horn neurons: influence of stimulation frequency and GABAergic inhibition.** *J Neurophysiol* 2014(April):552–567.
238. Sánchez E, Aguilar J, Rivadulla C, Canedo A: **The role of glycinergic interneurons in the dorsal column nuclei.** *Neurocomputing* 2004, **58-60**:1049–1055.

## Biography

Leonel (Leo) Medina was born in Santiago, Chile, in 1980. He received the BSc in electrical engineering and the MSc in biomedical engineering from Universidad de Chile in 2003 and 2006, respectively. He worked as a R&D engineer in the same institution for 4 years. Leo received the PhD in biomedical engineering from Duke University in 2016, under the guidance of Dr. Warren Grill. Leo was awarded a Fulbright-CONICYT Chile scholarship for doctoral studies in the US in 2010, and received a Student Travel Grant as a finalist of the paper competition at the IEEE-EMBS Conference in Neural Engineering, Montpellier, France, in 2015. Leo is married to Marcela since 2007, and has one daughter, Sofia.

### Publications:

- Medina, L.E.**, Grill, W.M Nerve excitation using an amplitude-modulated signal with kilohertz-frequency carrier and non-zero offset. *In review*.
- Howell, B., **Medina, L.E.**, Grill, W.M., 2015. Effects of frequency dependent membrane capacitance on neural excitation. *J Neural Eng* 12, 056015.
- Medina, L.E.**, Grill, W.M., 2014. Volume conductor model of transcutaneous electrical stimulation with kilohertz signals. *J Neural Eng* 11, 066012.
- Medina, L.E.**, Lebedev, M.A., O'Doherty, J.E., Nicolelis, M.A.L., 2012. Stochastic facilitation of artificial tactile sensation in primates. *J Neurosci* 32, 14271–14275.
- Perez, C.A., Estévez, P.A., Vera, P.A., Castillo, L.E., Aravena, C.M., Schulz, D.A., **Medina, L.E.**, 2011. Ore grade estimation by feature selection and voting using boundary detection in digital image analysis. *Int J Mineral Proc* 101, 28–36.
- Perez, C.A., Donoso, J.R., **Medina, L.E.**, 2010. A critical experimental study of the classical tactile threshold theory. *BMC Neurosci* 11, 76.
- Perez, C.A., Cohn, T.E., **Medina, L.E.**, Donoso, J.R., 2007. Coincidence-enhanced stochastic resonance: experimental evidence challenges the psychophysical theory behind stochastic resonance. *Neurosci Lett* 424, 31–35.
- Perez, C.A., Gonzalez, G.D., **Medina, L.E.**, Galdames, F.J., 2005. Linear versus nonlinear neural modeling for 2-D pattern recognition. *IEEE Trans Sys Man & Cybern, Part A* 35, 955–964.
- Medina, L.E.**, Grill, W.M., 2013. Mammalian Motor Nerve Fibers, Models of. In: Jaeger, D., Jung R. (Ed.) *Encyclopedia of Computational Neuroscience*: SpringerReference, Springer-Verlag, Berlin.